Reduced-order modeling of granular intrusions driven by continuum approaches

by

Shashank Agarwal

B.Tech., Indian Institute of Technology Gandhinagar (2014)
S.M., Massachusetts Institute of Technology (2019)

Submitted to the Department of Mechanical Engineering
in partial fulfillment of the requirements for the degree of

Doctor of Philosophy in Mechanical Engineering

at the

MASSACHUSETTS INSTITUTE OF TECHNOLOGY

May 2022

Author .....
Department of Mechanical Engineering
March 21, 2022

Certified by .....
Ken Kamrin
Professor of Mechanical Engineering, MIT
Thesis Supervisor

Certified by .....
Gareth H McKinley
Professor of Mechanical Engineering, MIT
Thesis Supervisor

Certified by .....
Wim M van Rees
Assistant Professor of Mechanical Engineering, MIT
Thesis Supervisor

Certified by .....
Daniel I Goldman
Professor of Physics, Georgia Institute of Technology
Thesis Supervisor

Accepted by .....
Prof. Nicolas Hadjiconstantinou
Chair, Graduate Program Committee

Reduced-order modeling of granular intrusions driven by continuum approaches

by
Shashank Agarwal

Submitted to the Department of Mechanical Engineering
on March 21, 2022, in partial fulfillment of the
requirements for the degree of
Doctor of Philosophy in Mechanical Engineering

Abstract

Granular intrusions such as ballistic impacts, vehicular and animal locomotion in natural terrains, and stirring of materials in industrial processes are common. Granular media often exhibits coupled solid-like and fluid-like multiphase characteristics in such systems that are commonly not shown by simple solids (like metals) and fluids (like water). This makes modeling granular media challenging. While the field of granular physics extensively uses grain-scale Discrete Elements Modeling (DEM) to model such characteristics of granular systems, they are computationally expensive. On the other hand, capabilities to model such systems in real-time are critical in numerous applications such as path planning and efficient maneuvering of vehicles in sandy terrains on earth and extra-terrestrial environments. Due to their shape- and media-specific forms, existing reduced-order intrusion modeling methods have limited capabilities.

This work focuses on developing efficient approaches to model motions of arbitrarily shaped objects into the granular volumes to various numerical details and accuracy levels. Specifically, we focus on a mesoscale continuum approach and a macroscale empirical approach. We establish the sufficiency of appropriately-chosen constitutive laws and computational methods in modeling various complex granular flow scenarios with a continuum approach. We exploit the approach to develop deep insights into the origin of granular resistive forces encountered during granular intrusions. We further use these insights to extend an empirical modeling method called Resistive Force Theory (RFTs) for real-time modeling of granular intrusions. RFTs developed in this work are verified against a variety of experimental and simulation results and allow modeling the motions of arbitrary three-dimensional objects moving arbitrarily in granular media at low and high speeds in real-time.

Thesis Supervisor: Ken Kamrin
Title: Professor of Mechanical Engineering, MIT

Thesis Supervisor: Gareth H McKinley
Title: Professor of Mechanical Engineering, MIT

Thesis Supervisor: Wim M van Rees
Title: Assistant Professor of Mechanical Engineering, MIT

Thesis Supervisor: Daniel I Goldman
Title: Professor of Physics, Georgia Institute of Technology

Acknowledgments

The completion of this work would not have been possible without the guidance and support of my research and academic advisor, Prof Ken Kamrin. Ken has continually encouraged me to be a better student and researcher, providing me with his invaluable tutoring to investigate the details of challenging problems from a curious researcher's perspective. His push for solving problems till the last exception and coming up with robust and beautiful solutions has been a great research experience. I thank my parents and elder sister for their encouragement and constant support from overseas. I specifically thank my sister Dr. Swati Agarwal who has been the most significant pillar of implicit support to me. She took care of my parents in multiple medical emergencies over the past few years when I was unable to travel home. Special thanks to our collaborator Andy Karsai and Prof Daniel Goldman at Georgia Institute of Technology. Their experimental expertise was vital for this work. Timely and in-depth feedback from my thesis committee members, Prof Gareth H. McKinley and Prof Wim M van Rees have also been very useful. I am thankful to all my peers in MechE and the members of the Kamrin Group, especially Maytee, Saviz, and Aaron, for making this entire experience a positive one. I am also indebted to an innumerable number of friends who have been there for me throughout my time at MIT.

Contents

List of Figures

List of Tables

Chapter 1

Reduced-order modeling of granular media: meaning, utility, history, and status

1.1 What are granular materials and why are they so complex?

Granular media are among the most common and yet most complex classes of materials around us. Sand in deserts, mining material in the industry, food grains, and pharmaceutical pills all fall under the category of granular media. In fact, granular media constitutes the second most handled material in the industry after water [1]. In general, they are defined as — 'A conglomeration of discrete solid, macroscopic particles characterized by a loss of energy whenever the particles interact. The most common example would be friction when grains collide' [1]. Their tendency to display multi-phase characters in fairly simple and daily life scenarios differentiates them from other classes of materials such as simple solids (like metals and ceramics) and liquids (like water and paints) [2, 3]. For instance, figure 1-1 shows a few real-life scenarios in which sand, a granular media, shows a solid, as well as a fluid-like behavior. The cases correspond to the motions of vehicles in the deserts and a golfer hitting a golf ball stuck in a sand trap. In all these cases, while the unmoved sand (supporting the human and/or vehicle weight without continuously deforming) shows a solid-like behavior, the flowing sand particles show a fluid-like material behavior. In order to completely predict the flow of granular media in such cases, all the material states and corresponding physics are needed to be understood. Once understood, all the material states are needed to be appropriately characterized for accurate modeling of granular flows in such systems.

While solid-like and fluid-like (and sometimes gas-like) behaviors are the most

Figure 1-1: Examples of granular materials displaying it's multi-phase nature in diverse real-life scenarios (A) Motion of car in desert [4], (B) A golfer hitting a golf ball from a sand trap [5], and (C) A bike wheel over sands [6]

visible aspects of such materials, the media is much more complex at the elementary level. At the microscopic level, granular media consists of solid particles or grains that interact to resist the flow when acted upon by an external motion or force (or both). As expected, all grains are not identical solids with identical properties. Grains vary in shape, size, density, stiffness, surface properties, strength, porosity, particle shape, particle size, particle density and their distributions through out the granular domain, to name a few [7]. The conglomerations of grains respond differently to different external loads based on cumulative grain properties. Similarly, the nature and magnitude of external loads and individual grain properties such as grain plasticity dictate the evolution of granular volume properties such as inter-grain and intra-grain porosity, packing efficiency, etc. [7, 8]. For instance, fine non-cohesive powders are known to develop cohesion at very high loads but remain cohesionless at low loads, a concept used for manufacturing pills in the pharmaceutical industry [9, 10, 11]. In addition, the presence of surrounding fluids (such as air and water) and their interactions with the grains further complicate the modeling of granular media in certain scenarios [12, 13, 14, 15]. Thus, even the simplest types of granular materials may require considering a large number of properties, making their computational modeling a fairly complex task.

1.2 Simplifying granular response modeling

A variety of simplifications are often used for modeling granular media responses in various situations. These simplifications rely on getting a deep physical insight into granular flows and identifying dominating mechanics of material response. Once known, these insights are used to introduce simplification in material representations that facilitate the overall numerical modeling task.

Numerous simplifications can be made to simplify the modeling of granular vol-

umes. For instance, granular volumes can be represented as discrete particles, with each particle having individual grain properties, a continuum media with no particle character, or a mixture of two. In each representation, further simplifications can be made by controlling the physics included in their forms, for instance, grain properties in the particle approach and complexity of constitutive laws in the continuum approach. Simplifications in representations and properties are often acceptable because the existence of a grain character does not necessitate its utility in modeling every scenario related to granular flow [16, 17]. Some properties could play negligible roles in the dynamics of certain granular flows and thus could be ignored due to their insignificant contributions to the final material response. For instance, while a media could very well show rate-dependent effects, the property could be ignored if the material flow is quasi-static. Similarly, while grains of a granular volume could very well show plastic deformations at large stress values, the grain plasticity can be ignored if the system stresses always remain negligible in comparison to the yield stress of individual grains in a flow. To better understand the advantages and limitations of modeling granular volumes, we discuss three approaches commonly used for modeling granular volume in the order of decreasing complexities. The activity will help us develop a systematic understanding of granular media modeling:

1.3 Micro-scale modeling: Discrete Element Method

At the fundamental level, granular media consists of grains. This property is kept intact in the particle approach for modeling granular media. The grains are represented at the individual particle level, with each particle having grain-specific characteristics such as radius, stiffness, and other surface properties. The approach is commonly called Discrete element method (DEM) [18, 19, 20, 21]. The method was first introduced by Cundall and Stack [22]. The most basic DEM models for modeling granular media consider each particle as a sphere, and the contact force between any grain-pair is modeled as a spring-dashpot system with a tangential friction limit (see figure 1-2). Upon application of external forces or displacements, the particles experience contact forces from neighboring particles. The contact forces and the external forces are integrated via Newton's laws of motion to calculate particle velocities and positions over physical space in DEM. Hertzian and Hookean contact models are among the most common particle contact models used in DEM modeling of granular media [19, 20, 21]. These models use the following formulations for the calculation of contact forces between the particles [23]:

In hookean contact model:

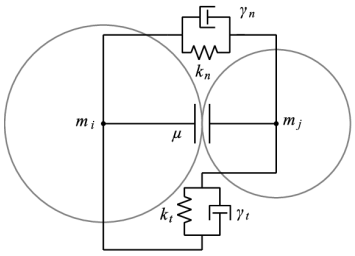

Figure 1-2: Representation of particle contact model for granular media

$$\boldsymbol{F}_{hk} = (k_n \delta \boldsymbol{n}_{ij} - m_{\text{eff}} \gamma_n \boldsymbol{v}_n) - (k_t \Delta \boldsymbol{s}_t + m_{\text{eff}} \gamma_t \boldsymbol{v}_t) \tag{1.1}$$

In hertzian contact model:

$$\boldsymbol{F}_{hz} = \sqrt{\delta}\sqrt{\frac{R_i R_j}{R_i + R_j}}\boldsymbol{F}_{hk} = \sqrt{\delta}\sqrt{\frac{R_i R_j}{R_i + R_j}}\big[k_n \delta \boldsymbol{n}_{ij} - m_{\text{eff}} \gamma_n \boldsymbol{v}_n) - (k_t \Delta \boldsymbol{s}_t + m_{\text{eff}} \gamma_t \boldsymbol{v}_t\big) \tag{1.2}$$

Both the formulations follow couloumb friction limit as:

$$\boldsymbol{F}_t \leq \mu \boldsymbol{F}_n \tag{1.3}$$

where,
$\delta = d - r$ represents overlap distance of 2 particles,
k_n represents elastic constant for normal contact,
k_t represents elastic constant for tangential contact,
γ_n represents viscoelastic damping constant for normal contact,
γ_n represents viscoelastic damping constant for tangential contact,
$m_{\text{eff}} = M_i M_j/(M_i + M_j)$ represents effective mass of 2 particles of mass M_i and M_j,
$\Delta \boldsymbol{s}_t$ tangential displacement vector between 2 particles which is truncated to satisfy a frictional yield criterion,
$\boldsymbol{n}_{ij}$ represents the unit vector along the line connecting the centers of the two particles,
$\boldsymbol{v}_n$ represents the normal component of the relative velocity of the two particles, and
$\boldsymbol{v}_t$ represents the tangential component of the relative velocity of the two particles.

Equation 1.1 and 1.2 represent the variation of contact forces between two particles from Hookean and Hertzian contact models. Forces in the normal direction are proportional to different powers of overlapping distance δ, and forces in the tangential direction are proportional to history-dependent tangential overlap $\Delta \mathbf{s_{ij}}$ in the two models. The formulation includes damping in the normal and tangential direction in the form of γ_n and γ_t coefficients [23].

1.3.1 Simplifications in micro-scale modeling

While particle level (micro-scale) modeling is one of the most elaborate modeling methods for modeling granular material, most of the widely used DEM models carry a variety of simplifications in them. Particle contact properties are often held constant across the volume for simplicity and efficient computations. In systems with known particle type, size, and interaction property distributions, multiple interaction properties and particle types are used. With increasing system complexities, the particle models are enriched with particle physics. For instance, in addition to the cohesionless simple spring-dashpot model shown above, particles can have cohesion which may increase and/or decrease as particles compress against each other. The interaction can also have rolling friction between the particles. For all such systems, more complex granular contact models are used [24, 19, 20, 21, 25]. We discuss a few typical simplifications used in defining particles in DEM, below:

Particle shape: Though naturally occurring granular materials come in diverse shapes, for ensuring simplicity and computational efficiency, they are often modeled as perfect spheres (i.e., every particle contact is modeled as sphere-sphere contact as shown in figure 1-2). The effects of variable grain shapes are compensated and incorporated in the choice of other material properties on statistical grounds and experimental observations. In recent years, models systematically incorporating grain shapes variations (such as ellipsoid particle shape and anisotropic grain properties [26, 27]) are also being proposed. In addition, for modeling arbitrarily shaped particles, variations of DEM have been developed which model arbitrary shapes with an agglomeration of grains or using polygonal definitions of individual particles [28, 29, 30].

Size distribution: In addition to particle size, grains in granular volumes may vary in their size. Estimating the size of every grain in the system is expensive and often impossible. Hence, granular volumes are often assumed to have a given grain size distribution (such as Gaussian and normal distributions) [31].

Individual particle and contact properties: Besides particle size and shape, assumptions in other grain properties are also used. They include the presence/absence of history dependence in contacts, rolling friction between the contacts, cohesion between the contacts, intra-particle porosity, and damage evolution in particles and others[32].

So far, our discussion corresponds to granular systems with negligible effects of other phases on grain interactions and flow dynamics. This is often a valid assumption for granular volumes with low-density fluids (such as air) at low pressure and flow rates, where the fluid drag on particles is negligible. In more complex systems, heavier/pressured/high-inertia fluids can exist between the particles and/or can cause significant fluid drags and inter-particle interactions [13]. A variety of two-

phase models are used for modeling such systems. In such approaches, while the solid phase (grains) is modeled as discrete particles (DEM), the fluid phase is modeled using conventional Navier-Stokes equations with various computational fluid dynamics (CFD) approaches such as finite volume method, FVM) (CFD-DEM [33, 34, 35, 18]), and Lattice Boltzmann Method, LBM (called LBM-DEM [36, 37, 38]) etc. In all these methods, additional particle–fluid interaction forces [39] are used to couple the motion of the two phases together and model the overall coupled system. Similar to the single-phase DEM, mixed methods often use simplifications for the numerical tractability of the approach. Coupling between the two phases is often limited to mass and momentum balance, and/or one-way drag forces (only the drag of fluid on the solid phase is considered and not vice versa) between the phases [14, 10]. Figure 1-3 shows a demonstration of a CFD-DEM approach for modeling flow of fluid-particle mixture during compaction of granular volumes in the presence of fluid phase around them based on an implementation by Goniva and Kloss [18].

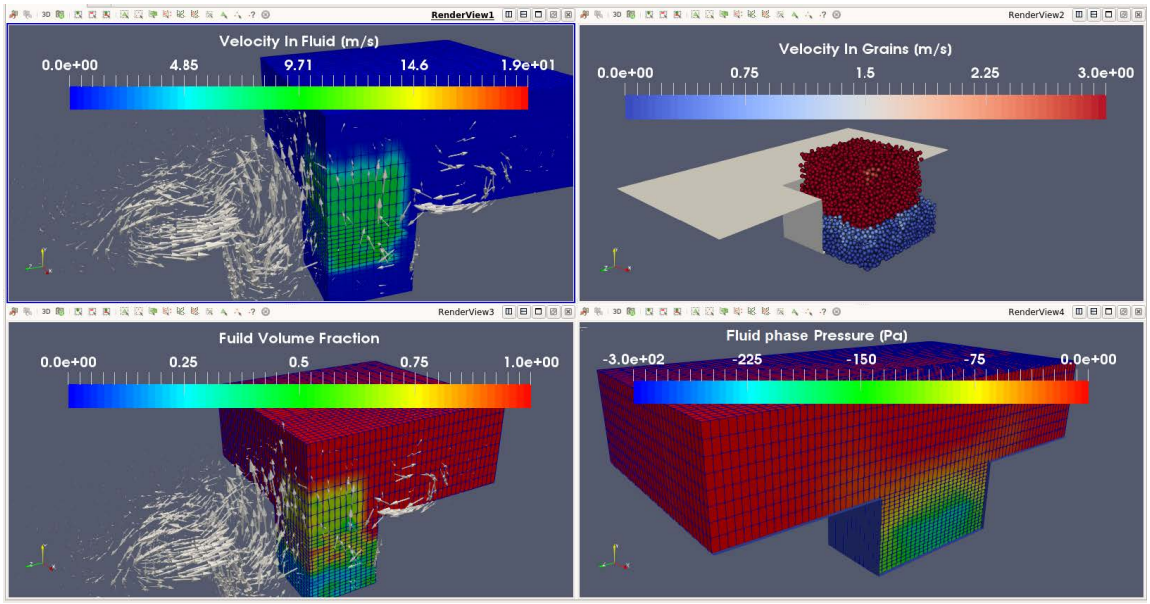

Figure 1-3: Demonstration of CFD-DEM technique in a compaction setting. Variations of various system variables in the solid and fluid phases (grains and air) are plotted upon intrusion of a piston, represented by a group of closely rigidly packed grains (shown in red) into a fluid-saturated granular bed. In these simulations, the fluid phase is modeled using the finite volume method (FVM) implemented in OpenFoam. Similarly, the granular phase in these simulations is modeled using the discrete element method implemented in LIGGGHTS. The coupling is done using CFD-DEM implementation by Christoph Goniva and Christoph Kloss [18], both at DCS Computing GmbH, 2012 (named CFDEM)

1.4 Meso-scale modeling: Continuum modeling

Consideration of the particle nature of granular materials for modeling granular flows (DEM) has well served the granular research community over the decades. DEM remains the most used method of modeling granular media in the industry over the years[24]. But accuracy of DEM comes at the expense of its large computational cost [40]. In recent years, there has been a growing interest in modeling increasingly larger granular systems [41, 42, 43, 44, 45]. This has led to a push for computationally faster alternatives to DEM, especially continuum descriptions of granular media[17].

In the continuum representation of granular media, it is assumed that though at the fundamental level (micro-scale) the granular media consists of grains, at a mesoscale, their flow and response can be modeled using a continuum displacement field that follows momentum balance equations (which dictate the evolution of media displacements based on system stresses and external forces) at the fundamental level. The stresses and displacements for material are related using materials constitutive laws and other material states [46]. The approach implements the continuum description of the granular media by assuming that the constitutive material laws (elastic-plastic for constitutive modeling used in this work) are sufficient to represent the majority of the material behaviors. In some cases, various particle effects could be added to the systems through material constitutive relations. The physics associated with particle re-arrangements, particle packing fraction, grain shape and size, stiffness, distribution, force transfer between the particles, and other aspects, are included using constitutive representations of these properties to ensure the physical accuracy of representations [47, 48, 49] in intended applications. For instance, a local density variable is typically used for representing the changing packing fraction of grains across the granular domains as a result of particle re-arrangement over time and space [50, 51, 52]. Similarly, numerous local state variables are used for capturing packing density-dependent strength of the media, phenomenon such as as Reynold's dilation[9], rate-dependent material response ($\mu(I)$ rheology [53, 54]) etc. As the continuum modeling ignores the particle representation of granular media, its performance deteriorates in systems where the length scale of the simulations starts approaching grain diameters (typically < 10 grain diameters). In this regard, mixed-methods, coupling the continuum approach with the DEM approach, have been introduced in recent years with various levels of success [55, 56].

Like DEM, the continuum modeling approach consists of two components — material constitutive relations and methods for implementing those constitutive relations over simulation domains. The choice of constitutive models depends on the materials and phenomenon under consideration. Similarly, implementing the continuum representation of the granular media requires methods that are capable of maintaining high numerical accuracy even under large deformations that are expected in granular flows. We use the material point method (MPM)[57] for implementing

various continumm material models in our research. More details on the constitutive laws and the MPM approach are provided in Chapter 2.

In the presence of other phases of matter such as fluids, Two-phase models (TFM) are used [58, 59]. TFM's can be considered as continuum equivalents of the CFD-DEM approach. In this approach, two phases (solid grains and liquid) are simultaneously modeled in the same physical space using two sets of constitutive laws. The two phases cross-talk with each other at each time step, to maintain mass and momentum balance on the domain. The drag forces on each phase due to the other, are also calculated using coupling equations such as Darcy's law[60, 13] at each time step. We do not use this approach in our work. For more details the reader can refer to Baumgarten and Kamrin [13]. Though TFM is computationally more efficient than a more detailed method such as LBM-DEM CFD-DEM, they remain less accurate in many scenarios.

1.4.1 Simplifications in mesoscale modeling

Similar to other methods, continuum modeling often assumes a variety of simplifications in defining a granular volume. Such simplifications include (but are not limited to) presence/absence of density variations in the media [17], the evolution of media density as a result of shear and/or volumetric loading of the media (Reynolds dilation/compaction, capping models) [61, 62, 11], rate-sensitivity of material properties ($\mu(I)$ rheology [53, 54]), presence of other phases (such as air and liquid) in the computational domain (Mixture theories) [13, 63] etc. The details incorporated in a constitutive law decide its applicability in a specific condition. Similarly, the capability of the implementation method to represent models of deformation and information transfer across the granular domain restricts its applicability to system under consideration. For example, conventional Finite Elements Methods(FEM) can not model large strains in granular intrusions. This is due to large errors associated with severely deformed elements in FEM. Modifications such as adaptive mesh refinement [64] are required to be made to make these methods conducive for the purpose.

1.5 Macro-scale modeling: Reduced-order/Empirical modeling

Real-life granular flow scenarios often require limited information from the system based on the applications at hand. For instance, estimating the power requirements for a conveyor transferring granular media (e.g. in the mining industry) requires only the effective load of the media on the conveyer as a result of its weight and the friction force it experiences due to sidewall friction on it. Similarly, deciding a

silo (used for storing grains) opening for a fixed flow rate of the grains only requires their dependence on silo angle, silo opening, and level of grains in it [65, 66, 67]. Similarly, characterizing the locomotion of vehicles in sandy deserts requires only the estimation of forces on wheels from the sands and does not require complete characterization of the granular flow itself. In all such cases, a limited amount of information from the system is sufficient for the end goal [68, 69].

Rigorous numerical methods such as finite element methods (FEM) [70], discrete element methods (DEM) [22], two-phase models (mixture theories)[58], and mixed methods (LBM-DEM, SPH-DEM, etc) [36, 37, 38, 56], model granular systems to a variety of details and accuracy. The detailing and accuracy of these methods come at high computational costs associated with them. While some methods are faster than others, none of them can estimate material response in real-time for applications discussed in this section. The associated high computational costs of such methods make them non-optimal approaches for quick estimation of granular response. Reduced-order or Empirical models provide great alternatives for these situations.

The origin of empirical methods dates to the early days of human civilization when they started making *rules of thumb*[71] for approximating the response of systems to external stimulus in lack of their detailed understanding (though the phrase 'Rule of thumb' dates just a few centuries back [71]). With the arrival of classical physics, the empirical methods improved. In modern days, empirical methods are defined as 'procedures for conducting an investigation that rely upon experimentation and systematic observation rather than theoretical speculation' [72]. The empirical approach becomes even more effective with the use of scaling/dimensional analysis, and the combination is extensively used in the fields of fluid mechanics and others. The field of granular media also uses empirical approaches, especially in relation to vehicular locomotion (discussed next). We discuss major forms of existing and upcoming empirical methods in granular mechanics next.

1.5.1 Dimensional analysis

The dimensional (or scaling) analysis combined with empirical observations to estimate the dependence of outputs on certain combinations of system inputs is the most common type of empirical modeling. The basic philosophy of the method is that if a system output depends on an exhaustive list of system state variables, independent of how complex the dependence is, the final dependence must satisfy dimensional constraints. Thus, just by knowing the dimensions of the system state variables, many variable interdependencies can be obtained. Scaling analysis has long been reliably used in the field of fluid mechanics, heat transfer, acoustics, terramechanics [73] and many others for analysis, design, and development of complex systems [72].

The concept of Reynolds number, Stokes number, Parcelet number, Mach number all have their origin in this approach [74]. In this thesis work, we use scaling analysis in multiple places to improve existing knowledge of granular materials and make new discoveries. For the latest developments in scaling laws in granular media, the reader could refer [75, 17, 76, 77].

1.5.2 Terramechanical methods

With the arrival of automobiles, the invention of the rubber tire to its current form, and the beginning of the use of automobiles (automobiles and tanks) in warfare in the early 20th century, researchers became more interested in optimizing the motion of vehicles in deserts and other natural terrains. The famous book 'The eyes of the desert rats' [78] talks about the adventures of Brigadier Ralph A. Bagnold in Libyan deserts in the late 1930s and specifically, do's and don't for optimizing motions of vehicles on sand from an empirical perspective. In the book, the Brigadier says —

"It should be taken at full speed on the high gear as far as possible, only putting low gear when the speed slackens considerable and returning to high gear as soon as the sufficing acceleration has been obtained. Stopping anywhere on hard and slightly elevated ground should be avoided and getting into ruts of a preceding car is dangerous if the ground is sat all soft. A car will frequently go without difficulty in virgin ground but will stick if the same ground has been ploughed up by other cars"

A breakthrough in the field of motion of objects in granular volumes, especially near free-surface vehicular locomotion, came with the works of Bekker [79] in the 1960s. Bekker gave a semi-empirical formulation for modeling rigid cylindrical wheel motion over non-cohesive sands. Since then, many [80, 81, 82, 83] have expanded their work to expand on the capability of their theories in diverse scenarios and materials like dry snow [84], clay [85] etc. The most notable contribution in this regard came from Wong and Reece, which has become the de facto model of rigid cylindrical wheels on soft terrain [80, 81]. Wong and Reece's model is the most commonly used method in terramechanics for deriving wheel torque, thrust, and sinkage by estimating the stress distributions along the wheel-terrain contact region. The model is based on the Bekker pressure-sinkage relation, and the Janosi-Hanamoto shear-displacement equation [82]. Both the equations and their schematic representation in regards to a cylindrical wheel are provided in eq 1.4 and eq 1.5 and figure 1-5. In brief, the method characterizes a rigid circular wheel moving (rolling and slipping) on sand using a combination of fitting parameters derived using physical insights and experimental observations into the motion of wheels in sands.

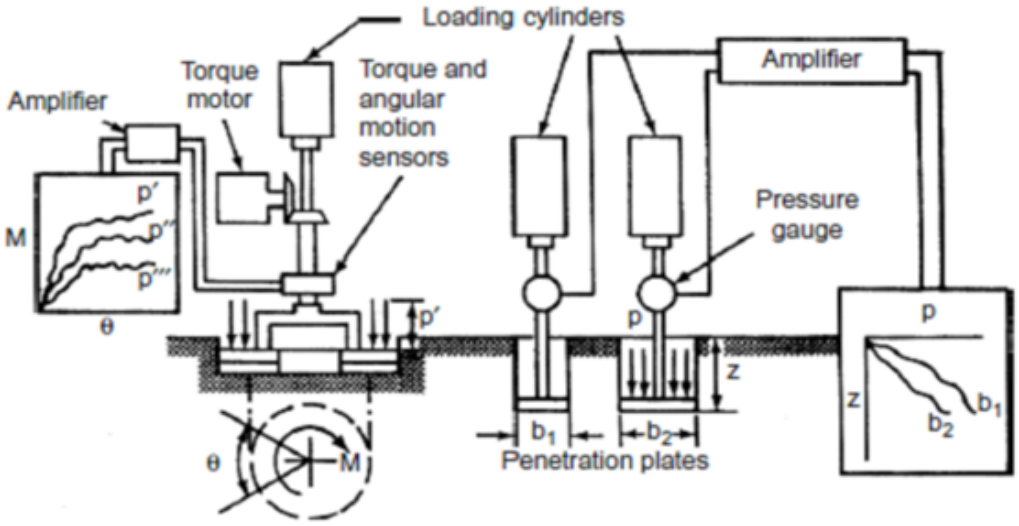

Figure 1-4: Bevameter setup proposed by Bekker [79] and used for terramechanical charaterization of granular media

Bekker pressure-sinkage relation:

$$p = \left(\frac{k_c}{b} + k_\phi\right) z^n \tag{1.4}$$

Parameters k_c, k_ϕ, n are empirical constants that dependent on soil properties, while b corresponds to the intruding plate/tire width. These parameters can be obtained from field tests conducted with a device called a Bevameter (Figure 1-4 [86, 87]).

Janosi-Hanamoto shear-displacement equation [82]:

$$\tau = (c + \sigma \tan\phi)\left(1 - e^{-\frac{J}{K}}\right) \tag{1.5}$$

where c and ϕ are the cohesion and the angle of internal shearing resistance of the terrain, respectively. K is the shear displacement modulus which may be considered as a measure of the magnitude of the shear displacement required to develop the maximum shear stress (see [84]). J represents the shear displacement of the wheel edge with respect to the adjacent soil.
The above equations represent the stress state along a cylindrical wheel surface as shown in Figure 1-5. The model introduced by Wong and Reece derives the wheel torque, thrust, and sinkage by estimating the stress distributions along the wheel-terrain contact region using the above formulations. More details of the model can be found in Chapter 3 of Agarwal [88].

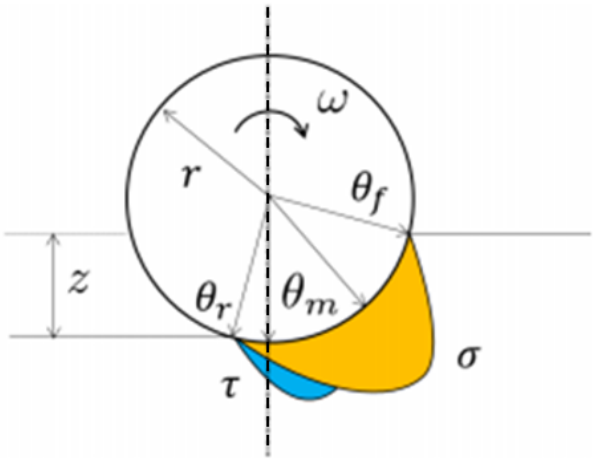

Figure 1-5: Normal (σ) and Tangential (τ) stress profiles along a wheel surface. θ_f and θ_r represent the angles subtented by wheel at fore and aft points of contact of the wheel with the terrain (known as 'soil entry' and 'soil exit'). θ_m is the angle at which the maximum normal stress occurs.

1.5.3 Semi-empirical method: Resistive Force Theory (RFT)

While the terramechanics methods are among the most commonly and extensively used methods in the field of granular locomotion, in recent years, a new approach has gained a lot of attention. The approach is called Resistive Force Theory (RFT).

The Resistive Force Theory methodology was originally introduced by Gray and Hancock [89] for modeling self-propelling undulatory biological systems in viscous fluids. In this theory, a simple approximate formula for the resistive force on a segment of a thin body was derived from the Stokes equations as a function of the segment's velocity components, orientation, and a few variables characterizing the fluid-segment interaction. Importantly, the theory assumed decoupling of the forces over the various segments of the body [90]. The success of fluid RFT motivated many [91, 92, 93] to explore the existence of a similar theory in granular media. Li et al. [93] proposed a plane strain version of RFT for granular media (2D-RFT). The theory assumes superposition and de-coupling of forces over the surface elements of a large body. The granular RFT has been found to be successful in modeling granular intrusions at low speeds. At low-speed limits, the rate-independent nature of granular media (characterized using a non-dimensional *inertial number* [53, 54, 94]) makes the force relations velocity-magnitude independent. Similarly, the local-pressure-dependent bulk strength, gravitational loading dependent pressure, and dimensional

analysis in such limits lead to the following form of a generic RFT.

$$\boldsymbol{F}_{total} = \int_{surf} \boldsymbol{\alpha}_{x,y,z}(\hat{\boldsymbol{n}}, \hat{\boldsymbol{v}}, \boldsymbol{g})|z|ds \tag{1.6}$$

Where $\boldsymbol{F}_{total}$ represents the total integrated forces on the surface of the body which is sub-divided into smaller sub-surfaces of area ds and $|z|$ mean depth from the free surface. The vector-valued $\boldsymbol{\alpha}_{x,y,z}$ represents the force per unit area per unit depth ($|z|$) and is an function of the surface normal ($\hat{\boldsymbol{n}}$), velocity direction ($\hat{\boldsymbol{v}}$), gravity vector ($\hat{\boldsymbol{g}}$), and the granular material and material-intruder surface-interaction properties. Thus, the local force (integrant) on sub-surfaces are extracted independently from each other at varying depths($|\boldsymbol{z}|$), orientations ($\hat{\boldsymbol{n}}$), and velocity directions ($\hat{\boldsymbol{v}}$) in a granular system with given material properties and gravity. The vector-valued function $\boldsymbol{\alpha}_{x,y,z}$ is a priori obtained through experiments or simulations of plate drag and depends on the granular media properties, the media-intruder surface interaction, and the value of gravity. The net granular resistive forces on the body are calculated by summing up all the sub-surface force using localization [91], de-coupling, and superposition of force fields on intruder sub-surfaces. A comprehensive comparison of various existing reduced-order methods for modeling granular intrusions, including 2D-RFT and a *terramechanical* model, can be referred from Agarwal et al. [95]. Chapter 3 of this thesis discusses RFT in more detail.

This thesis extensively focuses on expanding the capabilities of 2D-RFT and develops various advanced versions of RFT, namely Dynamic RFT (DRFT) and 3D-RFT that are discussed in more detail in Chapter 4 and Chapter 5. Chapter 3 goes into finer details of 2D-RFT before introducing DRFT and 3D-RFT to the readers.

1.5.4 Machine learning and new approaches

The recent decade has witnessed exponential growth in the field of machine learning (ML). In the context of terramechanics, the ML approach is not too different from empirical modeling. While the empirical modeling tries to create the rules of thumbs with systematic experimentation for characterizing the response of systems to external stimulus, machine learning attempts to do so on un-organized data. Both approaches typically do not directly include system physics in their implementation, but substantial improvements are seen with their incorporation. Though, in recent years physics-inspired machine learning has also gained some attention for modeling granular media (as well granular intrusions) [96, 97, 98, 99], it is yet to become a mainstream modeling/prediction tool in the field.

1.6 Conclusion

In this chapter, we briefly discussed the complexities of modeling granular media. We discussed three types of modeling approaches that are commonly used for modeling granular systems — namely, the DEM approach (micro-scale modeling) that models granular systems at grain level, the continuum approach (meso-scale modeling) that models granular systems as continua, and reduced-order approaches (macro-scale modeling) that focus on getting limited system outputs without performing full-field characterization of the systems. Each method has associated advantages and limitations. We conclude that even though granular media are fairly complex at the fundamental level, they can be modeled to various levels of complexity depending on the application at hand. The extent of complexities and details in any method plays to its advantage and limitations in accuracy and computation time. For instance, particle-based approaches are among the most accurate, versatile, but computationally expensive approaches for modeling granular volumes. In contrast, the empirical approaches are the least expensive and limited in scope. But each one has its utility in specific applications.

In this thesis, we primarily focus on developing faster methods for modeling low and high-speed granular intrusions. The task is divided into two parts. First, we attempt to understand the physics of granular intrusions with full-field numerical approaches. And second, we use that understanding to reduce the computation times further. To understand the physics of granular intrusions, we focus on the continuum modeling approach. The approach is expected to give us a physical insight into the origins of granular resistive forces in computationally more efficient ways than DEM. In addition to its advantage on computational efficiency over DEM, the continuum approach is also expected to systematically single out the individual constitutive aspects of the media responsible for different types of force generations in the media by providing a fine control on material properties included in the constitutive models, which could not be done in DEM (more details in chapter 2 section 2.6). We use the insights obtained from continuum modeling to develop further reduced-order models for granular intrusions. The latter half of the thesis focuses on the empirical modeling technique RFT, which is a rapidly growing method with the potential to paradigmatically shift the field of *terramechanics* and *granular intrusion modeling* over time. We have developed numerous forms of granular RFT to extend the real-life applications of RFTs. A brief overview of the contents of the thesis is provided below:

1. Chapter 1: Introduced the concepts of reduced-order modeling in granular media and the approaches that can be used for modeling granular volumes to varying levels of accuracy

2. Chapter 2: Discusses the efficacy of the continuum approach in modeling and understanding a variety of granular flow and intrusion scenarios

3. Chapter 3: Provides an in-depth understanding of two-dimensional granular resistive force theory (2D-RFT). The discussion serves as the base for understanding RFT extensions in chapters 4 and 5

4. Chapter 4: Introduces a high-speed version of resistive force theory called Dynamic resistive force theory or 2D-DRFT driven by insights obtained through continuum modeling of granular intrusions

5. Chapter 5: Introduces a three-dimensional version of 2D-RFT called 3D-RFT

6. Chapter 6: Concludes the thesis with possible avenues of future research topics based on this thesis work

Chapter 2

Continuum approach for modeling granular intrusions

Chapter 1 discussed the complexity of granular materials and their tendency to show multi-phase behaviors where the media shifts among solid-like and fluid-like states [2, 7]. Granular intrusions such as meteorite impacts and high speed locomotion in deserts [41, 42, 43] (see figure 1-1) often create complex flow and force responses, where the media exhibits such multiphase characteristics. The media deforms elastically under stress like a solid, but begins to flow like a fluid once a friction-based yield criterion is met. Large variations in the media stress, momentum, and volume fraction in different regions often result in complicated system dynamics exhibiting multiphase characteristics [2, 3]. The flow complexity also makes interpreting resistive forces non-trivial if the intruder re-interacts with the deformed region [100], as the media now has a new inhomogeneous state near the surface. The media's inhomogeneous flow and multiphase nature often restricts modeling to discrete particle methods that track the individual grains, unlike fluids that can be solved with the Navier-Stokes equations. These behaviors of the media are dictated by many material properties and local state variables such as pressure and granular packing fraction[101]. The coupled space and time dependence of these state variables, as well as the multi-phase behavior of the media, makes modeling overall granular flow response computationally expensive.

As discussed in section 1.3.1, though Discrete Element Methods (DEM) are reliable and established methods for modeling granular media [102, 103] and have played a major role in the advancement of the field of granular media[104, 105], their precision comes at a computational cost. Once the simulation's spatial scale becomes large relative to the size of the particles in the system, the computational cost of simulating many particles makes DEM prohibitively expensive. As an example, a 0.1 mm particle diameter granular system with a 0.5m per side cubic domain would

require evaluating $\sim 9 \times 10^{11}$ DOF per time step (at a packing fraction of 0.64 with 6 degrees of freedom, degree of freedom (DOF) per particle). While current large-scale granular DEM studies remain in the range of $\sim 10^7$ particles ($\sim 10^8$ DOF) [33, 34], efforts are being made to extend this range. Most recently, some have reached the $\sim 10^9$ DOF range with the use of supercomputers and GPUs [106]. On the other hand, there has been a growing interest in modeling increasingly large granular systems in recent years, such as those relevant in ballistic impacts, wheeled locomotion, and agricultural plowing [41, 42, 43, 44, 45]. This has led to a push for computationally faster alternatives to DEM, such as using continuum descriptions of granular media. We discuss this approach in more detail in this chapter and evaluate its efficacy in modeling our systems of interest— granular intrusions.

2.1 Introduction

In this chapter, we focus on modeling diverse real-life scenarios of granular flows with the continuum approach to test and establish its efficacy in modeling common granular flow systems. The chapter highlights the capability of the approach in modeling and explaining common granular intrusion cases using a very minimal set of constitutive ingredients, a revelation which is of great value for the community, as well as for reduced-order modeling as we will discuss later in this thesis. The study also aims at understanding the flow dynamics in these cases which is also useful in developing empirical insights into the cases considered in this study.

The phenomena we focus on herein have been independently studied in the literature, and the work demonstrates that they can be quantitatively modeled and unified under a family of basic constitutive assumptions. With the aim of testing the limits of simple constitutive models, we use two basic constitutive representations of non-cohesive granular media in this work:

- A non-dilatant plasticity model (NDPM), and
- A dilatant plasticity model (DPM).

The DPM model permits dilatancy during dense flow, while the NDPM model assumes dense flow is a constant-volume process (details later). Thus, the NDPM is suitable for modeling steady-state granular behaviors, while the DPM is a more suitable model for transient flow processes. The latter is also a more elaborate model that converges to the former model under certain limits. Both of these models have their respective advantages depending on the scenarios they simulate. We do not include micro-inertial $\mu(I)$ effects [107] (effects of grain-level inertia on material properties) in these models; thus, both of these constitutive models are rate-insensitive. More

details of each model are provided in a later section.

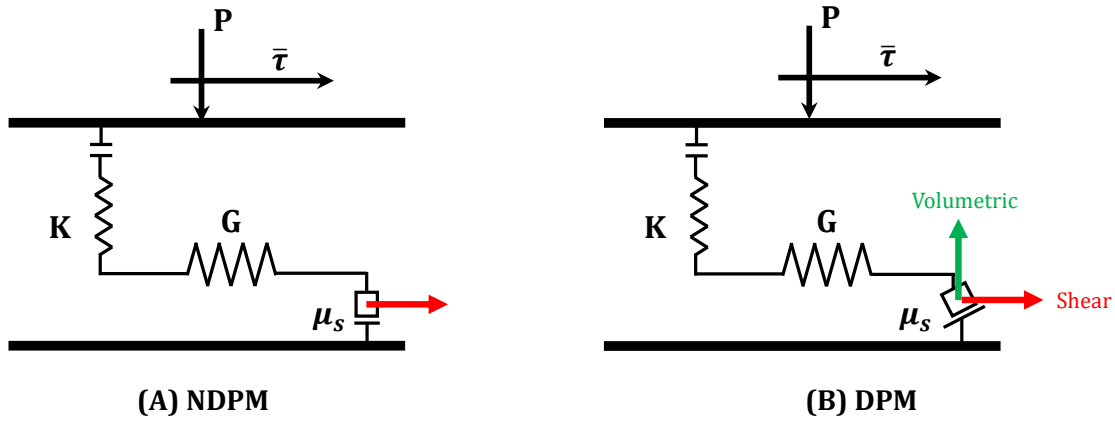

Figure 2-1: *Analog model representation of NDPM and DPM: (A)* Non-dilatant plasticity model (NDPM) and (B) DPM models representations in two dimentions. The vertical direction represents the direction of shape preserving volumetric deformations. And the horizontal direction represents the volume preserving shear deformations. In both the models, the material offers no resistance to the tension i.e. $P = 0$ below a critical density ρ_d. In compression ($P > 0$), both the models have an elastic volumetric response with bulk modulus K and an elastic-plastic shear response with shear modulus G and yield strength proportional to pressure (P) times an internal friction variable μ_s. NDPM model shows a pure shear response upon plastic loading. On the other hand, DPM model shows shear as well as volumetric (compaction or dilation based on local density value) response upon plastic loading. More details are provided in section 2.2.1 and 2.2.2.

We highlight here that we ignore numerous particle-based media properties such as grain-plasticity and the presence of other phases in these models. This is a justifiable choice because all the granular intrusions considered in this study (discussed next) occur near the free surfaces of the granular beds. The resultant stresses in these systems are expected to be low and unlikely to cause any plastic deformations in the constituent grains. Similarly, the fluid phase (air) drags are expected to be negligible. Had the pressures been higher, more advanced models such as the Ducker-Prager Cap Model and Cam-Clay models, and two-phase models would have been more appropriate choices [61, 62, 11].

To demonstrate the utility of each model, we consider granular flow and force responses in four fundamental intrusion cases which have been studied in the literature (see Figure 2-2) :

1. Depth-dependent force response in horizontal submerged-intruder motion,
2. Separation-dependent drag variation in parallel-plate vertical-intrusion,
3. Initial-density-dependent drag fluctuations in free surface plowing, and
4. Flow zone development during vertical plate intrusions in under-compacted granular media.

We use NDPM in the first two cases (which focus on a steady response) and DPM in the latter two cases (where transient effects are the focus). Our continuum modeling approach captures the dynamics of such granular flows and gives a deeper macroscopic insight into each of these cases. Thus, our study not only highlights the efficacy of continuum modeling for predictive purposes but also highlights its utility in developing macroscopic conceptual understanding of diverse granular intrusion phenomena. Additionally, while DPM is a more elaborate representation of granular media compared to NDPM, NDPM is easier to implement and is computationally more efficient to solve. Thus, by using NDPM in the first two cases, we also aim to highlight the advantages and sufficiency of simpler models in certain cases.

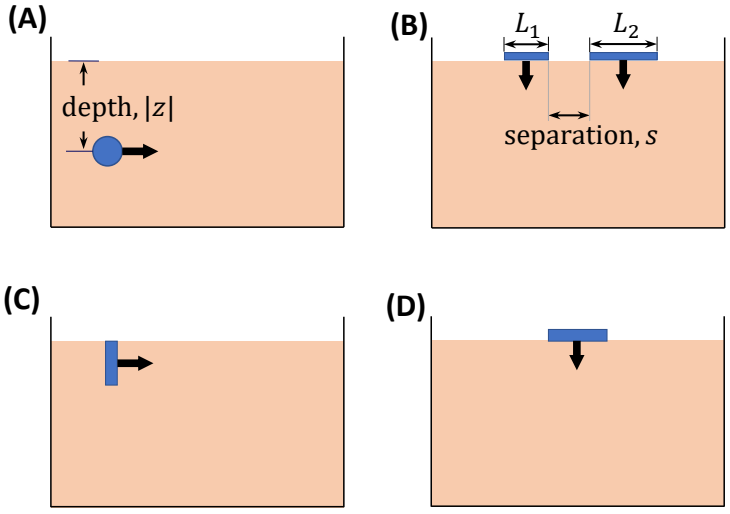

Figure 2-2: *Schamatics of four test cases considered in this study: (A)* Horizontal dragging of a submerged cylinder at different depths, *(B)* multiple-plate vertical granular intrusion, *(C)* free-surface plowing in under- and over-compacted granular media, and *(D)* vertical intrusion in under- and over-compacted granular media. Cases *(A)* and *(B)* are modeled with the non-dilatant plasticity model (NDPM), and cases *(C)* and *(D)* are modeled with the dilatant plasticity model (DPM) to model transient effects.

2.2 Material model and implementation

2.2.1 Non-dilatant plasticity model (NDPM)

This model is taken from Dunatunga and Kamrin [108, 109]. The model assumes a rate-insensitive, Drucker-Prager yield criterion, incompressible plastic shear flow (with no dilatancy), and cohesionless response in extension whereby the material becomes stress-free below a *'critical density'*. The constitutive flow equations representing the above behavior are shown below. These simultaneous constraints describe the material's separation behavior, shear yield condition, and tensorial co-directionality, respectively:

$$(\rho - \rho_d)P = 0 \quad \text{and} \quad P \geq 0 \quad \text{and} \quad \rho \leq \rho_d, \tag{2.1}$$

$$\dot{\gamma}(\tau - \mu_s P) = 0 \quad \text{and} \quad \dot{\gamma} \geq 0 \quad \text{and} \quad \tau \leq \mu_s P, \tag{2.2}$$

$$D_{ij}/\dot{\gamma} = \sigma'_{ij}/2\tau \quad \text{if} \quad \dot{\gamma} > 0 \quad \text{and} \quad P > 0, \tag{2.3}$$

for $i, j = 1, 2, 3$.

where,

ρ is the local granular density,

ρ_d is the critical density of close-packed grains,

μ_s is the internal friction coefficient,

$P = -\sigma_{ii}/3$ is the local hydrostatic pressure,

$\dot{\gamma} = \sqrt{2D_{ij}D_{ij}}$ is the equivalent shear rate.

$\tau = \sqrt{\sigma'_{ij}\sigma'_{ij}/2}$ is the equivalent shear stress,

$\sigma'_{ij} = \sigma_{ij} + P\delta_{ij}$ is the deviatoric part of Cauchy stress tensor,

$D_{ij} = (\partial_i v_j + \partial_j v_i)/2$ is the flow rate tensor.

For simplicity, the equations above are expressed in rigid-plastic form, where the flow rate is approximately all due to plastic flow. However, we also include a small elastic component which ensures that below the yield criterion the grains have a well-defined solid constituive behavior. The model evolves the flow by solving the momentum balance equations, $\partial_j \sigma_{ij} + \rho g_i = \rho \dot{v}_i$. We also assume a constant friction coefficient μ_f between the granular continuum and solid-body surfaces. The internal friction value μ_s is often measured from the tangent of the angle of repose for the granular media or from a direct shear test[110]. We refer to this model as the 'Non-Dilatant Plasticity Model' (NDPM). We provide the input material properties used in various cases in the relevant sections. We also provide a 2D schematic representation of the model in figure 2-1A.

2.2.2 Dilatant plasticity model (DPM)

While NDPM assumes a single critical granular density cutoff for the entire granular volumes, this is often not the case in real granular systems. Granular media can support stress in a range of densities, including close and loose packings[7]. The second model we present addresses this limitation of the NDPM model and allows for density evolution in the media [101]. This model takes inspiration from the family of Critical State models [101, 49]. We use a simple rigid-particle version of the Critical State model in which grains are not modeled to crush under hydrostatic loads; rather, they only have a hydrostatic elastic response in this case. When pressure is non-zero, the material is deemed to be in a 'dense state,' and the density evolution occurs through shearing-based Reynolds dilation/contraction, representing particle rearrangements at the granular level. In a dense state, the packing fraction ϕ is equal to an evolving state variable ϕ_d. Every shearing action in dense media drives the local value of ϕ_d towards a limiting steady-state critical packing fraction, ϕ_c. Furthermore, when the packing fraction varies, the material's friction coefficient also changes; material with a low packing fraction has low consolidation and thus has less strength than more consolidated media.

Thus, in terms of constitutive relations, the simultaneous constraints describing the material's separation behavior and shear yield condition (eq.2.1 and eq.2.2, respectively) remain the same with the two exceptions that the close-packed density, ρ_d, and internal friction value, μ_s, are non-constant local state variables (which vary with time and space), as follows:

$$\rho_d = \rho_g \phi_d, \qquad \mu_s = \mu_c + (\phi_d - \phi_c)\chi \tag{2.4}$$

Here, ρ_g represents the solid grain density, χ represents a dimensionless scaling constant, and μ_c represents the critical-state internal friction value reached by material at steady state (when $\phi_d = \phi_c$). When pressure is positive (the packing is dense), the evolution of ϕ_d is modeled as:

$$\frac{d\phi_d}{dt} = -3\beta\phi_c\dot{\gamma} \tag{2.5}$$

where, $\beta = (1/3)(\phi_d - \phi_c)\chi$ is a local dilatancy variable. In the absence of confining pressue, the material can leave the dense state ($\phi < \phi_d$), but reconsolidates at the current value of ϕ_d unless the material opens up beyond a global lower limit, $\phi_d^{\min}$, which defines a minimum density possible for loaded media, below which no connected material states exist. We set this value to 0.45 in all simulations. Thus, the material can exist in a dense state only for $\phi \geq 0.45$ and the local state variable ϕ_d gets reset to $\phi_d^{\min}(= 0.45)$ whenever ϕ drops below this value.

In addition to the material's separation behavior and shear yield condition (eq.2.1

and eq. 2.2), the material flow rule has a deviatoric dependence as before (eq.2.3) but due to dilation now also has a corresponding volumetric component. The volumetric strain rate is given by the dilatancy variable, β. The plastic flow rate tensor, thus, has the form:

$$D_{ij}/\dot{\gamma} = \sigma'_{ij}/2\tau + \beta\delta_{ij} \quad \text{if} \quad \dot{\gamma} > 0 \quad \text{and} \quad P > 0 \tag{2.6}$$

Thus, the combination of eqs.2.1, 2.2, 2.4, 2.5, and 2.6 collectively represent the Dilatant Plasticity Model (DPM). Note that DPM reduces to NDPM in the limit of $\chi \to 0$. Regarding its uasge in cases 3 and 4, χ is calibrated for each material qualiatively based on experimental observations.

2.3 Numerical implementation

2.3.1 Pseudocodes for implementing NDPM and DPM

Non-Dilatant Plasticity Model (NDPM)

This model implementation was adopted from Dunatunga and Kamrin [108]. Readers can refer to [108] for implementation and derivation details.

Dilatant Plasticity Model (DPM)

$$\text{Material Evolution:} \quad \mu_s = \mu_c + (\phi_d - \phi_c)\chi \tag{2.7}$$

$$\frac{\partial \phi_d}{\partial t} = -(\phi_d - \phi_c)\phi_d \chi \dot{\gamma}^p \tag{2.8}$$

$$\text{Plastic flow rule:} \quad \boldsymbol{D}^p = \frac{\dot{\gamma}^p}{\sqrt{2}} \frac{\boldsymbol{\sigma_o}}{||\boldsymbol{\sigma_o}||} + \beta \dot{\gamma}^p \underline{\mathbf{1}} \tag{2.9}$$

$$\beta = \frac{1}{3}(\phi_d - \phi_c)\chi \tag{2.10}$$

Known state properties: $\mu_c, \rho_g, m, \Delta t, \chi, \phi_d, \phi_c$

Input: $L^{n+1}, v^{n+1}, \boldsymbol{\sigma}^n$ (v represents volume here)

Output: $\boldsymbol{\sigma}_{n+1}$

Step n:

$\rho^{n+1} = m/v^{n+1}$

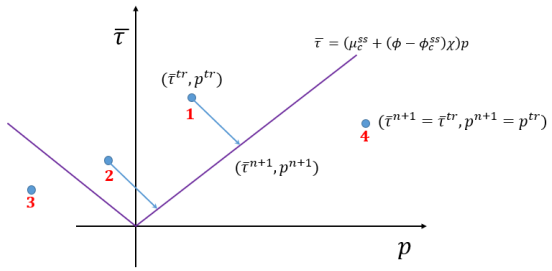

Figure 2-3: A representation of DPM on shear stress, hydrostatic pressure graph

$$\boldsymbol{D}^{n+1} = \tfrac{1}{2}(\boldsymbol{L}^{n+1} + (\boldsymbol{L}^{n+1})^T)$$
$$\boldsymbol{W}^{n+1} = \tfrac{1}{2}(\boldsymbol{L}^{n+1} - (\boldsymbol{L}^{n+1})^T)$$
$$\boldsymbol{G}^{n} = -\boldsymbol{\sigma}^{n}\boldsymbol{W}^{n+1} + \boldsymbol{W}^{n+1}\boldsymbol{\sigma}^{n}$$
$$\boldsymbol{\sigma}^{tr} = \boldsymbol{\sigma}^{n} + \Delta t\,[C : D^{n+1} + G^{n}]$$
$$p^{tr} = -\tfrac{1}{3}tr(\boldsymbol{\sigma}^{tr})$$
$$\boldsymbol{\sigma}_o^{tr} = \boldsymbol{\sigma}^{tr} + p^{tr}\underline{\mathbf{1}} \qquad \bar{\tau}^{tr} = \tfrac{1}{\sqrt{2}}||\boldsymbol{\sigma}_o^{tr}||$$
$$\mu_s = \mu_c + \Delta\phi_d\chi \qquad \Delta\phi_d = \phi_d - \phi_c$$
$$\alpha = K\chi\Delta\phi_d/G \qquad \rho_c = \phi_d\rho_g$$

Figure 2-3 shows a representation of DPM on a shear stress vs. hydrostatic pressure graph. A trial material stress state, assuming all the strain increment in a step is elastic, $\boldsymbol{D}^p = 0$ and $\boldsymbol{D}^e = \boldsymbol{D}^{n+1}$, can exist in any of the following four states at any time. Note that we use the superscript 'tr' to show *trial* values of state variables from here on. Similarly, we use the subscript 'o' to show deviatoric part of state variables. But the constitutive model allows the material stress state to exist only in zone 3, zone 4, or along the yield curve shown as the violet line in figure 2-3. Thus trial stresss in,

zone 1	$\Longrightarrow$	$p^{tr} > 0,\ \delta\gamma > 0$	Elastic-plastic step
zone 2	$\Longrightarrow$	$p^{tr} < 0,\ \delta\gamma > 0$	Elastic-plastic step
zone 3	$\Longrightarrow$	$p^{tr} < 0,\ \delta\gamma = \bar{\tau}^{tr}/G$	Separated material
zone 4	$\Longrightarrow$	$p^{tr} > 0,\ \delta\gamma = 0$	Completely elastic step

where $\delta\gamma$ represents the magnitude of plastic flow at the given step.

The numerical implementation ensures that material stress does not exist in zone 1 and 2. This is because these zones defy the material constitutive behavior (eq. 2.2). For evaluating the elastic and plastic components of the material states, we assume an additive decomposition of strain rate tensor: $\boldsymbol{D}^{n+1} = \boldsymbol{D}^p + \boldsymbol{D}^e$. Next, we

use the following relationships to express $(\bar{\tau}^{n+1}, p^{n+1})$, in terms of $\dot{\gamma^p}$:

$\bar{\tau} = (1/\sqrt{2})||\boldsymbol{\sigma_o}||$ $\qquad$ $\dot{\gamma^p} = \sqrt{2}||\boldsymbol{D_o^p}||$ $\qquad$ $\boldsymbol{D^p} = \frac{\dot{\gamma^p}}{\sqrt{2}}\frac{\boldsymbol{\sigma_o}}{||\boldsymbol{\sigma_o}||} + \beta\dot{\gamma^p}\underline{\mathbf{1}}$

$$
\begin{aligned}
\bar{\tau}^{n+1} &= \sqrt{1/2}||\boldsymbol{\sigma}_o^{n+1}|| = \sqrt{1/2}||\boldsymbol{\sigma}_o^{tr} - 2G\Delta t\boldsymbol{D}_o^p|| \\
&= \sqrt{\frac{1}{2}\left(\boldsymbol{\sigma}_o^{tr} : \boldsymbol{\sigma}_o^{tr} + (2G\Delta t)^2\boldsymbol{D}_o^p : \boldsymbol{D}_o^p - 2 * 2G\Delta t\frac{\dot{\gamma^p}}{\sqrt{2}||\boldsymbol{\sigma}_o^{tr}||}\boldsymbol{\sigma}_o^{tr} : \boldsymbol{\sigma}_o^{tr}\right)} \\
&= \sqrt{(\bar{\tau}^{tr})^2 + (G\Delta t\dot{\gamma^p})^2 - 2G\Delta t\dot{\gamma^p}\bar{\tau}^{tr})} \\
&= \bar{\tau}^{tr} - G\Delta t\dot{\gamma^p} \\
&= \bar{\tau}^{tr} - G\delta\gamma
\end{aligned}
$$

$$
\begin{aligned}
p^{n+1} &= -\frac{1}{3}tr(\boldsymbol{\sigma^{n+1}}) \\
&= -\frac{1}{3}tr(\boldsymbol{\sigma^{tr}} - \Delta t(2G\boldsymbol{D_o^p} + Ktr(\boldsymbol{D^p})\underline{\mathbf{1}})) \\
&= -\frac{1}{3}tr(\boldsymbol{\sigma^{tr}}) + \Delta tKtr(\boldsymbol{D^p}) \\
&= p^{tr} + 3\Delta tK(\beta\dot{\gamma^p}) \\
&= p^{tr} + \Delta tK((\phi_d - \phi_c)\chi\dot{\gamma^p}) \\
&= p^{tr} + (K\Delta\phi_d\chi)\delta\gamma
\end{aligned}
$$

Any elastic-plastic increment must lie along the yield curve, $(\bar{\tau}^{n+1} = \mu p^{n+1})$. Substituting $\bar{\tau}^{n+1}$ and p^{n+1}, we get:

$$
\begin{aligned}
\bar{\tau}^{tr} - G\delta\gamma &= \mu p^{tr} + \mu(K\Delta\phi_d\chi)\delta\gamma \\
\delta\gamma &= \frac{\bar{\tau}^{tr} - \mu p^{tr}}{G\big(1 + \mu\frac{K\Delta\phi_d\chi}{G}\big)} \\
&= \frac{\bar{\tau}^{tr} - \mu p^{tr}}{G\big(1 + \mu\alpha\big)} \\
\bar{\tau}^{n+1} &= \bar{\tau}^{tr} - G\frac{\bar{\tau}^{tr} - \mu p^{tr}}{G\big(1 + \mu\alpha\big)} \\
&= \mu\Big(\frac{\alpha\bar{\tau}^{tr} + p^{tr}}{1 + \mu\alpha}\Big) \\
p^{n+1} &= \frac{\alpha\bar{\tau}^{tr} + p^{tr}}{1 + \mu\alpha} \\
\dot{\gamma}^p &= \frac{\bar{\tau}^{tr} - \bar{\tau}^{n+1}}{G\Delta t}
\end{aligned}
$$

For a stress free state (p^{n+1}) the following conditions are also needed to be met: $\alpha\mu + 1 > 0$ and $\bar{\tau}^{tr}\alpha + p^{tr} < 0$

NUMERICAL IMPLEMENTATION

if $\rho^{n+1} < \rho_c$
$\boldsymbol{\sigma}^{n+1} = 0$

$\dot{\gamma}^p = \bar{\tau}^{tr}/G\Delta t$

else if $(\bar{\tau}^{tr} \leq \mu p^{tr})$ *elastic-step (Zone 4)*

$\boldsymbol{\sigma}^{n+1} = \boldsymbol{\sigma}^{tr}$

$\dot{\gamma}^p = 0$

else *elastic-plastic step (includes $p^{tr} < 0$)*

if $\big(\ p^{tr} \leq 0 \quad \text{and} \quad \bar{\tau}^{tr}\alpha + p^{tr} \leq 0 \quad \text{and} \quad \alpha\mu + 1 \geq 0\big)$ *(Zone 3)*

$\boldsymbol{\sigma}^{n+1} = 0$

$\dot{\gamma}^p = \bar{\tau}^{tr}/(G\Delta t)$

else *material has $\dot{\gamma}^p > 0$*

$p^{n+1} = \left(\bar{\tau}^{tr}\alpha + p^{tr}\right)/\left(\alpha\mu + 1\right)$

$\bar{\tau}^{n+1} = \mu p^{n+1}$

$\boldsymbol{\sigma}^{n+1} = \boldsymbol{\sigma}_o^{tr}\left(\bar{\tau}^{n+1}/\bar{\tau}^{tr}\right) - p^{n+1}\underline{\mathbf{1}}$

$\dot{\gamma}^p = \left(\bar{\tau}^{tr} - \bar{\tau}^{n+1}\right)/(G\Delta t)$

$\phi_d^{n+1} = \phi_d^n - (\phi_d^n - \phi_c)\phi_d^n\chi\dot{\gamma}^p\Delta t$

2.3.2 Material point method (MPM)

A variety of computational methods have been developed and utilized in recent years for to aid in simulating continuum models for large deformation processes, such as the Material Point Method (MPM)[108, 95, 111, 112], the Particle Finite Element Method (PFEM)[113], and Smoothed Particle Hydrodynamics (SPH)[114]. In this regard, a recent study on high-speed locomotion of wheels [16] in grains, a process which involves complex trans-phase characteristics of the soil and non-trivial grain motions, revealed that a continuum treatment implemented with MPM captures the essential behaviors and agrees well with experimental data. Thus, we use a continuum simulation approach based on the Material Point Method (MPM)[57], a derivative of

the fluid-implicit-particle (FLIP) method for implementing a continuum description of granular media.

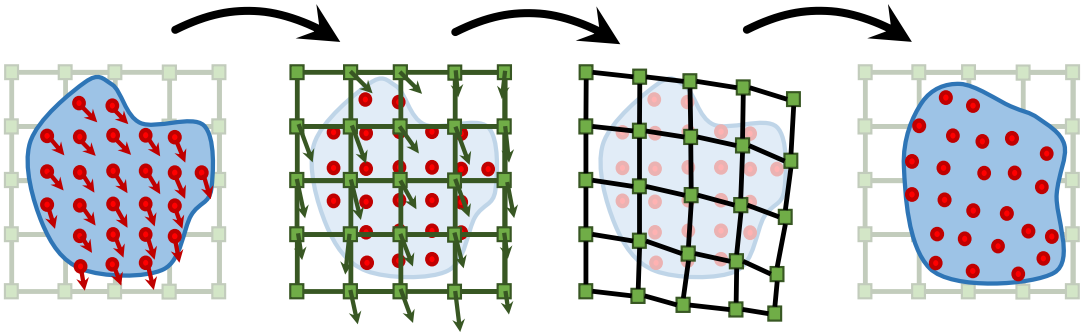

Figure 2-4: *Sample explicit time integration step in MPM:* The Lagrangian tracers representing material points (solid red circles) carry the state of material over time and space. The background grid (green squares) assists in integrating the motion on the simulation domain and is reset each step. More details can be found in Dunatunga and Kamrin [108].

The MPM implementation uses a combination of Lagrangian material points/tracers, which contain the state of the continuum, and a background computational mesh that is used to solve the equations of motion. These tracers, representing a chunk of material around their position, are 'cast' onto a background simulation grid where equations of motion are solved. Thus, material point tracers act as quadrature points for solving the weak form of the momentum balance equations on a static background simulation grid. Since the state is saved on the material points, the mesh is reset at the beginning of each computational step without any information loss, and thus the method allows for large deformations in the media without the error associated with large mesh deformations. A schematic representation of an explicit time-integration MPM-step is shown in Figure 2-4. We use the MPM implementation described in Dunatunga and Kamrin [108] to implement the different constitutive equations representing granular volumes assuming 2D plane-strain motion.

We choose the spatial grid resolution (Δx) in each system on a case-by-case basis, such that all the geometric features are well represented, and all system outputs converge. Also, to ensure numerical stability, we choose a time step (Δt) that satisfies the CFL condition based on minimum element size, maximum Young's modulus, and minimum medium density.

2.4 Verification studies

2.4.1 Case 1: Drag and lift on submerged cylinder dragging

Drag and lift forces on submerged objects in granular media are relevant in processes such as mixing, mining, soil-buried pipelines, and animal locomotion [115, 116, 117]. Over the past two decades, several studies[118, 119, 120, 121] have explored the mechanisms and the variation of these forces by considering the horizontal dragging of submerged, rigid cylinders (at different depths) as a test case. We specifically consider the work of Guillard et al.[119], who found that the horizontal drag force on horizontally moving cylinders increases with increasing depth while the vertical lift force plateaus for depths greater than an O(1) factor of the cylindrical diameter. The observations consider a depth range deep enough so that the cylinders are completely immersed in the granular bed even at the minimum depth. At very low depths near the free surface, the dragging motion of the cylinders results in an accumulation of the media in front of the intruders. This accumulation can augment the depth-dependence of drag forces and thus can change the force trends mentioned above. Thus, we do not consider such a near-free-surface depth range in this study (as in Ding et al.[121]) and focus on depths$\geq 2.5D$.

The experimental drag and lift results in Guillard et al.[119] were obtained by evaluating torques and vertical lifts on horizontal cylinders inside large granular beds rotated about the vertical axis. After a half rotation or so about the vertical axis, the authors observed a reduction in the force response as the cylinder begins re-interacting with the disturbed material as it is rotated multiple times. Here, we use the quasi-steady data obtained from the first half rotation of the cylinder, before it interacts with the disturbed media. Presumably, density variations play a smaller role in this portion, and hence we choose to compare the behavior observed with that of the NDPM model.

A schematic representation of the cylinder drag case is provided in Figure 2-2A. For the NDPM implementation, we use a grain density ρ_g of 2520 kg/m^3, and a critical packing fraction ϕ of 0.60. We calibrate the internal friction value (μ_s) for glass beads to 0.48 to accurately model the initial slope of depth vs. drag graph from the experiments. This is in line with the expected range of μ_s for the glass beads, which lies in the $0.39 - 0.55$ range (corresponding to an angle of repose range $\sim 22^\circ - 29^\circ$, depending on the surface roughness) [122]. The calibration absorbs possible inconsistencies between 2D simulations with 3D experiments and also incorporates the variations due to indirect measurements of experimental drag and lift from rotating cylinder experiments[119].

The cylinder is modeled as an elastic body with a high elastic modulus, thereby acting as an approximate rigid body. The media-cylinder interface friction coefficient (μ_f) is set to 0.35. The cylinder diameter, D is 4 mm, and the presumed out-of-plane

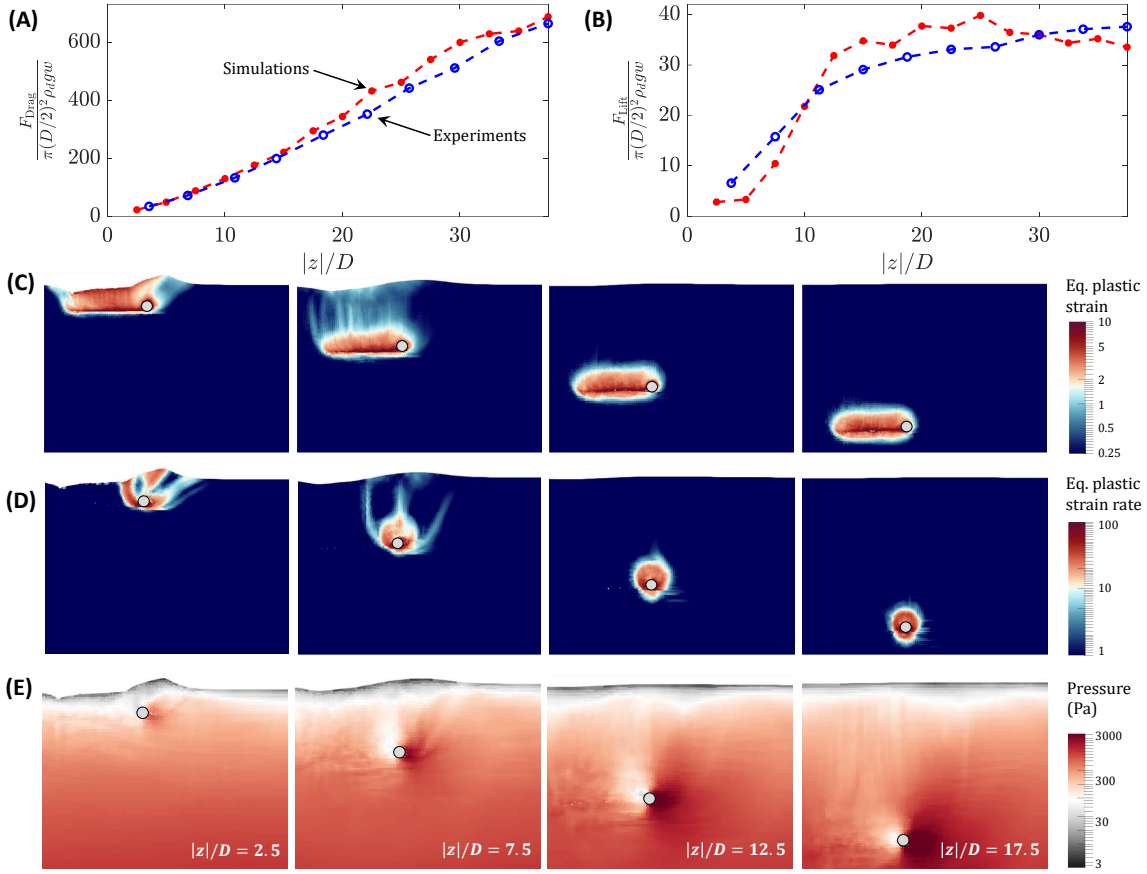

Figure 2-5: *Case 1: Experimental vs Simulations results for drag and lift on submerged cylinders (using NDPM model)*: Comparision of experimental data [119] (in blue) and the continuum simulations results (in red) for variation of *(A)* drag, and *(B)* lift on submerged cylinder motion in granular media with depth, $|z|$. The drag and lift forces are non-dimensionalized with characteristic force $\pi(D/2)^2\rho_d g w$ where D is the cylinder diameter, ρ is the effective medium density, g is the gravity, and L is out-of-plane cylinder width. Both experiments and continuum results use $D = 4$ mm, $\rho_d = 1512$ kg/m^3, and $g = 9.8$ m/s^2. Similarly depth is non-dimensionalized with cylinder diameter, D. Variation of macroscopic state variables *(C) equivalent plastic strain*, *(D) equivalent plastic strain rate*, and *(E) local hydrostatic pressure* at four different depths, $|z| = [10, 30, 50, 70]$ mm. The gray circle indicates the cylinder position and the drag direction is from left to right. See Movie S1 (refer to Appendix A.1) for visualizing material flow over time for cylinder drag cases considered in *(C)* and *(D)*.

length, w is 1 m (as the simulations are 2D plane-strain). We use a 0.20 m $\times$ 0.16 m granular bed, and a 5×10^{-4} m spatial resolution (Δx) for simulating these cases.

Figure 2-5A and B show the comparison of Guillard's experimental data to our continuum results. The linearly increasing nature of drag vs. depth graphs, along with the plateauing of lift vs. depth graphs, are well captured. The visualizations of plastic strains and strain rates (Figure 2-5C and D) qualitatively agree with those reported in previous numerical and experimental studies [118, 119]. Notably, the variation of the equivalent plastic strain shows a strong semblance with the work of Wu et al.[120]. Additionally, we also plot the variation of the local hydrostatic pressure at four different depths in figure 2-5E. The pressure distribution shows an asymmetry about the intruder, consistent with the existence of both drag and lift net forces, and as the intruder's depth increases, the vertical asymmetry diminishes, which is consistent with the plateauing of the lift force and continued growth of drag force.

Similar to past DEM studies by Guillard et al.[119] and experimental studies by Wu et al.[120], Figure 2-5C and D show high localization of the flow field for the depths greater than the lift turnover depth. A further increase in depth after this point results in a minimal-to-no change in the material flow profile. The drag and lift force behaviors are also related to this flow localization behavior. While the drag forces continue to increase linearly with depth, the lift forces become saturated near the depth the flow localizes, indicating a possible correlation between the flow and force. Figure 2-5E indicates a reducing asymmetry of the pressure variation around the cylinder as depth increases, consistent with the notion that drag forces continue to increase but lift forces plateau. A deeper analysis of this variation (i.e. the distribution and the relative magnitude of pressure) to understand the mechanics of the force distributions on different faces of the intruders is reserved for future study. Thus, the case of dragging submerged cylinders provides an example where NDPM captures the observed intrusion behavior.

2.4.2 Case 2: Vertical drag in two-plate granular intrusions

Multi-body intrusions offer another commonly encountered scenario in various real-life situations. Several researchers [123, 124, 125] have examined the dynamics of granular intrusions involving multiple intruding bodies. The case we study specifically takes inspiration from the work of Swapnil et al.[125] who examined the variation of vertical drag forces on a pair of parallel rigid plates during vertical downward intrusions as a function of the separation between them. They observed a peak in the average vertical drag as the separation between the plates was increased. A similar 'cooperative effect' was observed by Merceron et al.[124] during the upward motion of parallel intruders in the granular media. In their study, separations below a critical distance between the intruders were found to jam the media between the plates

(intruders) and result in a peak in the average particle disturbance (measured as average avalanche length) near this critical separation between the intruders. We use NDPM to investigate the findings of Swapnil et al.[125] and to capture and obtain macroscopic insight into the phenomenon. We also conduct experiments to verify claims that follow from theoretical analysis of the NDPM model.

A schematic representation of the case is given in Figure 2-2B. The case is studied in two parts. In the first part, we use generic material properties (provided next) to determine the behavior of the continuum model in the single-plate intrusion case. And in the second part, a direct quantitative comparison of simulation results with the experiments is made in the two-plate intrusion case (details later). We use a set of generic NDPM fitting properties from the earlier case, i.e. a grain density, ρ_g of 2520 kg/m^3, a critical packing fraction ϕ of 0.6, but choose the internal internal friction coefficient to be $\mu_s = 0.4$, which is common for glass beads [122]. The plates were modeled as stiff elastic bodies with vertical displacement of control points assigned; thus, the plates act as quasi-rigid objects with a common fixed downward velocity. The intrusion velocity was set to 0.1 m/s in all simulations, and the media-plate surface friction was set to 0.35. We use a 1.2 m $\times$ 0.6 m granular bed, and a 1.25×10^{-3} m spatial resolution (Δx) for simulating these cases.

Understanding single plate intrusions

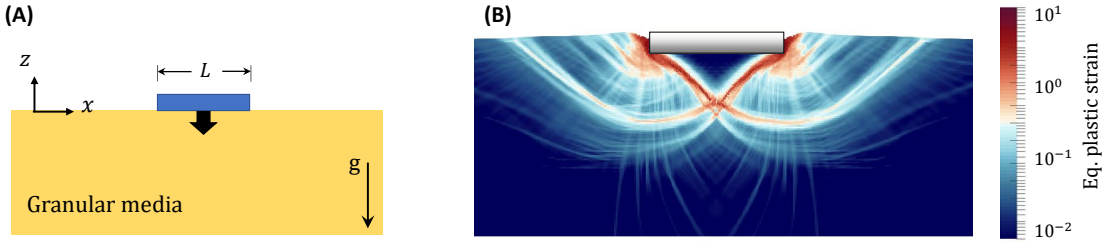

Figure 2-6: *Case 2: Vertical intrusion of single plates* (using NDPM model): *(A)* Schematic of single-plate vertical granular intrusion and (B) Variation of equivalent plastic strain in the granular volume. The simulations are plane-strain and glass bead properties are used for simulating granular media (ρ_g=2520 kg/m^3, $\phi = 0.6$, $\mu_s = 0.4$). The plate length was 0.1 m in *(B)*

We begin by first analyzing the variations of vertical drag forces in single plate intrusions. Figure 2-7A shows the drag forces on vertical plate intrusions under NDPM for various plate widths at a constant intrusion velocity of 0.1 m/s. Note that the same model and implementation was used previously [109] in the related case

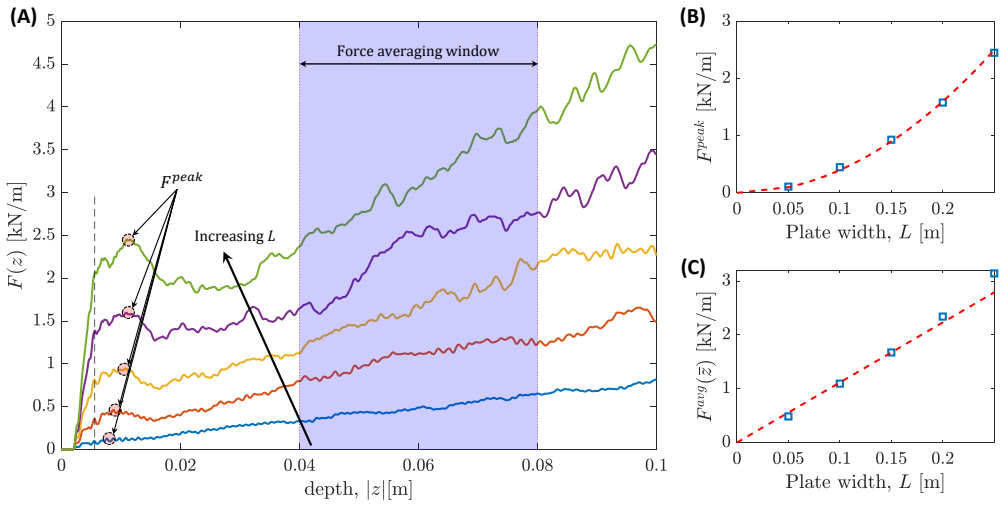

Figure 2-7: *Case 2: Vertical intrusion of single plates* (using NDPM model): *(A)* Variation of drag forces with intrusion depth for plates of various widths, L $(0.05, 0.10, 0.15, 0.20, 0.25\,\text{m})$ during single-plate vertical granular intrusion. The arrow shows the direction of increasing L. The simulations are plane-strain and glass bead properties are used for simulating granular media (ρ_g=2520 kg/m^3, $\phi = 0.6$, $\mu_s = 0.4$). Each data series on the left graph was time-averaged over a 0.5 ms window to remove high-frequency force fluctuations. The vertical black dotted line in *(A)* shows the depths after which this averaging window includes sufficient data. Dependence of *(B)* initial force peaks, and *(C)* average drag forces on plate widths in single plate intrusions (blue squares). The corresponding quadratic and linear fits for *(B)* and *(C)* are shown as red dotted lines in corresponding graphs. The force peaks are shown with arrows in the left graph. Time window used for calculating the average forces is the highlighted blue region (*force averaging window*) on the left graph.

of high-speed impacts of a circular intruder in granular media; the model quantitatively matched the flow and force data of Clark and Behringer [126]. Before analyzing the simulation results, we perform a scaling analysis of the problem, assuming the NDPM equations hold in order to predict the dependence of drag on various system parameters. In this case, we expect the drag force, on a vertical intruder of width L and out-of-plane width w at a depth of z, to depend on various system parameters, i.e. intruder dimensions (w and L), depth z(distance between the intruder bottom and the free-surface), close-packed media density ρ_d, gravity g, the media's internal friction μ_s, the media-intruder interface friction μ_f, and the velocity of intrusion v. Using scaling analysis, with base units of length as L, time as $\sqrt{L/g}$, and mass as $\rho_d L^3$, we obtain:

$$
\begin{aligned}
F^D &= \rho_d L^3 L(\sqrt{L/g})^{-2} \hat{f}(\mu_s, \mu_f, z/L, w/L, v/\sqrt{gL}) \\
&= \rho_d g L^3 \hat{f}(\mu_s, \mu_f, z/L, w/L, v/\sqrt{gL})
\end{aligned} \tag{2.11}
$$

Where, $\hat{f}$ represents some unknown function. Recall that we are scaling based on NDPM, so certain properties such as the particle diameter do not appear in the above relation.

The dependence of F^D on z can be divided into two regimes. (1) At low depths $z \ll L$, the variable z/L is negligible and can be ignored. And (2), at larger depths, the drag forces F^D are known to show a linear dependence on depth (after an initial jump in the vertical drag near free surfaces[127, 128, 129, 77]). In both of these regimes, we set the dependence of F^D on w to be linear, assuming the plane-strain nature of the intrusions. We also focus on intrusions that are sufficiently slow such that F^D is independent of velocity v (low-velocity regimes) as seen in the work of Swapnil et al.[125].

With the above assumptions, in the $z \ll L$ regime, we obtain:

$$
\begin{aligned}
&F^D = \rho_d g L^3 (w/L) \hat{f}(\mu, \mu_f) \\
&\rightarrow F^D/w = \rho_d g L^2 \hat{f}(\mu, \mu_f) \\
&\rightarrow F \propto L^2.
\end{aligned} \tag{2.12}
$$

And in the latter, moderate-depth regimes with $F^D \propto z$, we obtain:

$$
\begin{aligned}
&F^D = \rho_d g L^3 (w/L)(z/L) \hat{f}(\mu, \mu_f) \\
&\rightarrow F^D/w = \rho_d g z L \hat{f}(\mu, \mu_f) \\
&\rightarrow F \propto zL.
\end{aligned} \tag{2.13}
$$

Thus, from the scaling analysis, we expect the drag forces per unit out-of-plane width F ($= F^D/w$) (unit N/m) to have a quadratic dependence on plate width, L, near the free surface, and a linear dependence on plate width at larger depths. The scaling analysis does not provide information on the exact form of variation of F^D in z in the region connecting the two regimes. However, we do expect the variation to be non-monotonic in z since in the vanishing depth limit, the force scales as L^2, and in the deeper limit, it scales with zL.

Using the simulation's force output, in Figure 2-7B and C we plot the observed relationships between F and L at, respectively, a smaller depth (where initial peaks occur) and in a deeper regime, where linear force variations are predicted. The forces in Figure 2-7C are averaged over a depth window ($z_i - z_f$), i.e.

$F^{avg} = (\int_{z_i}^{z_f} F(z)\mathrm{d}z)/(z_f - z_i)$. The expected trends from the dimensional analysis are apparent. Besides our own simulation results, the linear dependence of drag force on intruder area, once deep enough, is a well studied relation [127, 128, 129]. We reiterate that our simulations are all in the quasistatic regime. Thus, the velocity contributions are negligible in comparison to static force contributions in our study. Thus, the initial peak in the force response is not related to inertial drag as seen in faster intrusions[130, 128].

Physically, the initial force maxima (F^{peak}) in the force vs. displacement graphs of Fig. 2-7A correspond to the force requirements for initiating media flow in the system. The F^{peak} force contributions enable the beginning of flow by initiating the shearing of the media, which exists at some finite strength due to finite pressure under the plate. From slip-line theory for granular intrusions[131], the flow develops a wedge-shaped no-shear-zone below the intruder, which has an acute angle of $\pi/2 - \tan^{-1}(\mu)$ (where μ represents the material internal friction). Thus, the requirement of shearing media of a finite strength along the wedge-shaped shear zone is responsible for these force contributions. We can obtain an intuition for the initial L^2 dependence of force by considering the conventional limit analysis for indentation of materials with yield stress Y, common in manufacturing processes such as drawing and blanking[132]. In such cases, indenter force per unit out-of-plane width, F, varies as $F \propto Y \times L$ for L the indenter plate length. In frictional media, the strength is pressure-sensitive. With $Y = \mu \times P$ and supposing P grows linearly along the edge of the no-shear-zone wedge, the mean strength along the edge grows $\propto L$. Substitution of $Y \propto L$ in the limit analysis formula then gives the observed quadratic dependence of the drag force on L. We do not further investigate these forces but identify that the existence of small regions of under-compacted granular media near free surfaces is expected to suppress the growth of such forces in many cases (see figure 2-13D). Our simulations indicate that the drag forces' dependence of F on L enter linear regimes at depths $z \sim O(10^{-1})L$. These forces are unique from the 'added mass' effects[133] and other macro-inertial effects[127, 128] in granular impacts that are common in high-speed intrusion (and vary $\propto v^2$) since our intrusion velocities are small.

Two plate intrusions

The above scaling analysis gives an important insight into the case of multi-body intrusions. In the purview of eq. 2.13, we expect that two plates intruding far from each other and at moderate depth will experience the same net vertical drag as that experienced by a single plate with an equivalent surface area — the linearity in L (eq.2.13) indicates that this equality should hold for any ratio of areas between the two plates. Thus, any combination of plate widths should experience the same forces

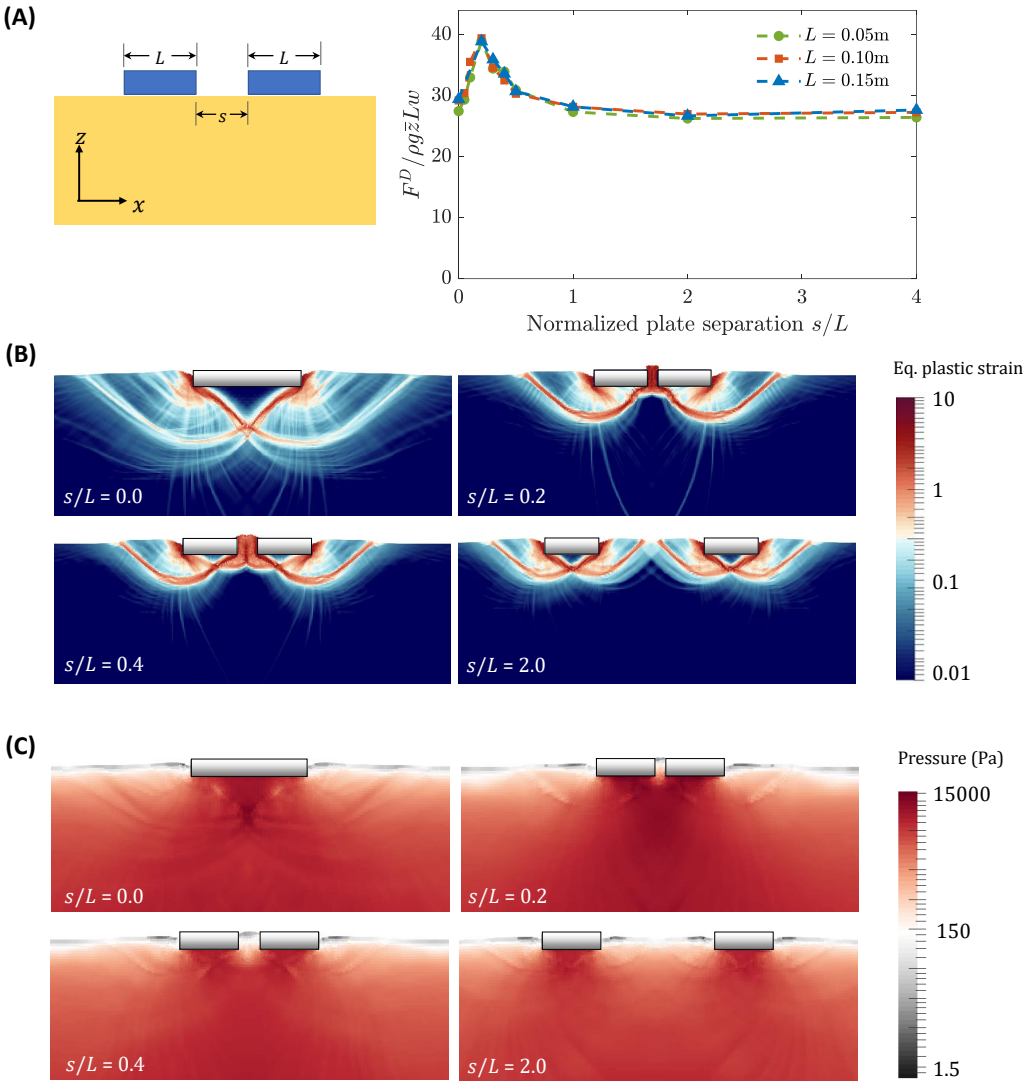

Figure 2-8: *Case 2: Vertical intrusion of two parallel plates (using NDPM model)*: *(A)* Variation of vertical drag (normalized) with plate separation, s (normalised to plate width L) and *(B)* the correspondng flow fields of *equivalent plastic strain* for equally sized plates (L = 0.10 m each) and *(C) local hydrostatic pressure*, for equally sized ($L = 0.10$ m each) plates. The forces F^D in *(A)* are averaged over a depth range ($z_i - z_f$) of $0.04 - 0.08$ m for all the cases and an average depth, $\bar{z} = 0.06$ m, $w = 1$ m, $g = 9.8m/s^2$, $\rho_d = 1512kg/m^3 (= \rho_g * \phi)$ is used. The simulations are plane-strain and glass bead properties are used for simulating granular media (ρ_g=2520 kg/m^3, $\phi = 0.6$, $\mu_s = 0.4$). See Movie S2 (refer to Appendix A.1) for visualizing material flow over time for *(B)*.

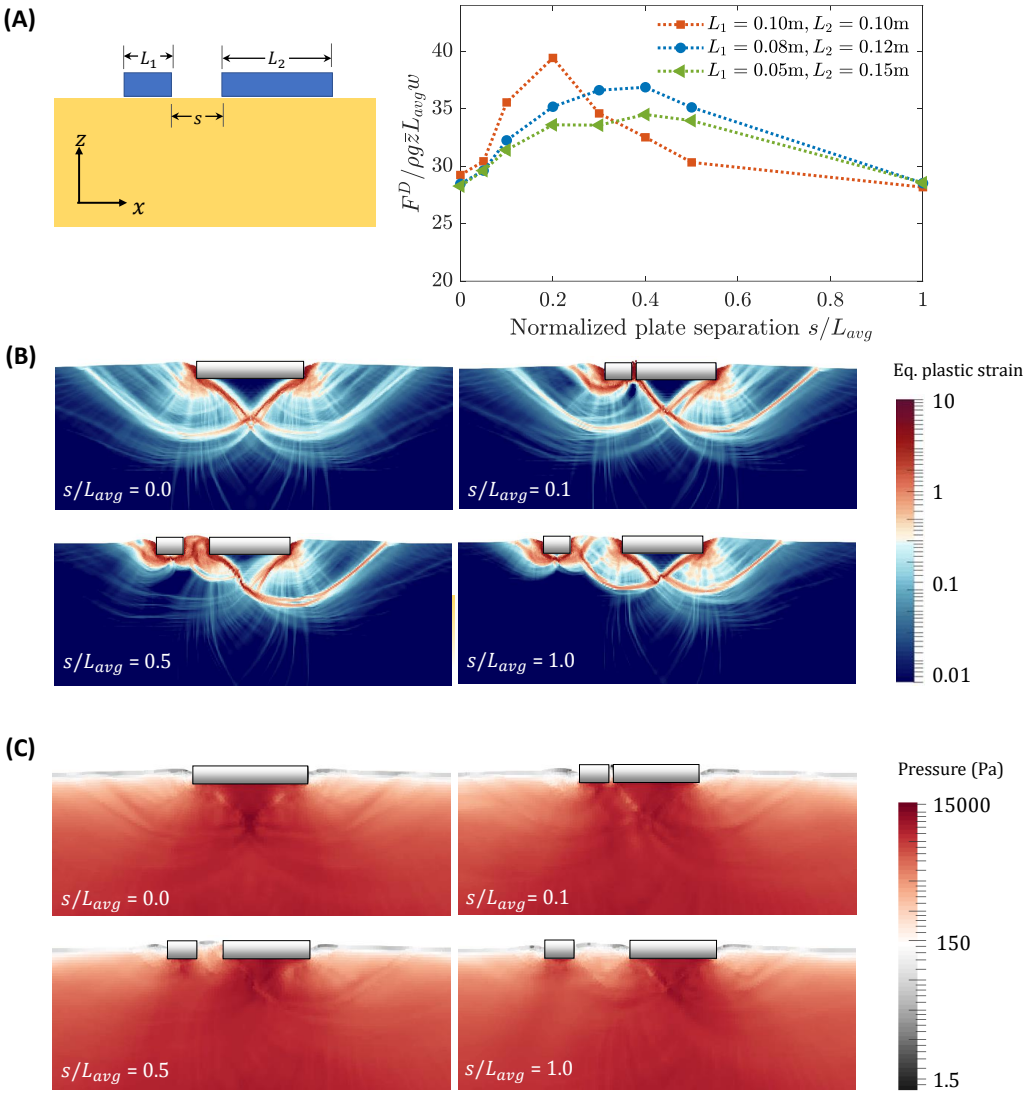

Figure 2-9: *Case 2: Vertical intrusion of two parallel plates (using NDPM model)*: *(A)* Variation of vertical drag with plate separation, s (normalised with average plate width $L_{avg} = (L_1+L_2)/2$) and the flow fields visualization using *(B) equivalent plastic strain* and *(C) local hydrostatic pressure* for unequally sized plates ($L_1 = 0.05$ m and $L_2 = 0.15$ m, bottom) plates. The forces F^D in *(A)* are averaged over a depth range $(z_i - z_f)$of $0.04 - 0.08$ m for all the cases and an average depth, $\bar{z} = 0.06$ m, $w = 1$ m, $g = 9.8m/s^2$, $\rho_d = 1512kg/m^3 (= \rho_g * \phi)$ is used. The simulations are plane-strain and glass bead properties are used for simulating granular media (ρ_g=2520 kg/m^3, $\phi = 0.6$, $\mu_s = 0.4$). See Movie S2 (refer to Appendix A.1) for visualizing material flow over time for *(B)*

both when they are infinitely far apart and when they have no separation. This analysis does not provide any information on the force variations when the plates are close but are at a finite distance from each other. However, physical intuition suggests that the presence of plates in the vicinity of each other will restrict the material flow, which should increase the drag on each plate. Given that the plates experience equal net forces at infinite and zero separation between them, we expect there to be a value of separation at which the force response is maximal or minimal (unless the force response is constant). The work of Swapnil et al.[125] explored this variation and found there is a peak in the force response at a low value of separation between the plates. Note that near the free surface ($z \ll L$), we do expect drag force at zero separation to be higher than at infinite separation due to the quadratic dependence of the force on plate size in this regime — the ratio of forces for plate lengths of L_1 and L_2 would be $F_0/F_\infty = (L_1+L_2)^2/(L_1^2+L_2^2)$ which is always greater than 1.

Figure 2-8A and 2-9A show the variation of force for different combinations of plate widths and plate separations. Continuum modeling shows the existence of force peaks for both equal plate cases (Figure 2-8A) and unequal plate cases (Figure 2-9A). Our observations are in accord with similar experiments and DEM simulations by Swapnil et al's[125] for equal plates. As the continuum modeling successfully captures the behavior, the detailed material states in these simulations can now be used to identify the macro-mechanical origins of the phenomena. We visualize the material flow by plotting snapshots of the plastic strain in a few of these cases. The plastic strain fields before, at, and after the force peak in Figure 2-8B and 2-9B suggest a macro-mechanical picture. We observe higher granular flow interaction between the two plates as the separation between the plates is decreased. For a single plate intruder, any neighboring flow restriction is expected to make it more difficult to push material during the intrusion. Thus, decreasing plate separation results in increasing drag on each plate. Once the plates are sufficiently close, a large wedge-shaped rigid zone forms, spanning the plates, causing the two plates to act as a single large plate. Thus, any further reduction in the separation does not result in additional flow restriction. Instead, it leads to a reduction in the effective area of the merged plate systems, and thereby the drag forces decrease upon a further decrease in separation. It is interesting to note that the material flow profiles when the two plates are together or far-separated are similar to the classical plasticity solution of Prandtl [134] for yielding of metals upon indentation under a plate, characterized by a single rigid wedge of media under the indenter and flow emanating from both edges of the wedge. However, when the plates are separated but very close, the flow profile looks similar to the indentation plasticity solution of Hill [135], characterized by two smaller wedges under the plate and flow emanating only from the two outermost edges. We also plot the variation of local hydrostatic pressure in the media for the two cases in figures 2-8C and 2-9C. The ratio of local pressure magnitudes with

equivalent hydrostatic pressure, $\rho_d g|z|$, is large (~ 40) in accord with the observations of Brezinski et al. [129].

To understand the behavior of the flow solutions, we re-derive the scaling relations for combinations of plates of different lengths L_1 and L_2 ($L_1 \leq L_2$) assuming NDPM, similar to the single plate case. Using base units of length as $L_{avg} = 1/2(L_1 + L_2)$, time as $\sqrt{L_{avg}/g}$, and mass as $\rho_d L_{avg}^3$, we obtain:

$$F^D = \rho_d g L_{avg}^3 \hat{f}(\mu_s, \mu_f, z/L_{avg}, s/L_{avg}, w/L_{avg}, L_1/L_2, v/\sqrt{gL_{avg}}).$$

With similar assumptions as before in the moderate-depth regime ($F \propto z$),

$$F^D = \rho_d g z L_{avg} w \hat{f}(\mu_s, \mu_f, s/L_{avg}, L_1/L_2).$$

Defining a non-dimensional force, $\tilde{F} = F^D/\rho_d g z L_{avg} w$, we get

$$\tilde{F} = \hat{f}(\mu_s, \mu_f, s/L_{avg}, L_1/L_2) \tag{2.14}$$

and for equal plates, $L_1 = L_2$, $L_{avg} = L$ and we obtain:

$$\tilde{F} = \hat{f}(\mu_s, \mu_f, s/L). \tag{2.15}$$

Therefore, if the NDPM model suffices to describe the physics of two-plate intrusion, we expect the above relation to describe a master curve that collapses data for plates of various L intruding into the same media.

Based on eq.2.14, for $F \propto z$, we obtain following relations for peak separation (s_p) and corresponding peak force (F_p) values:

$$s_p = L_{avg}\, \hat{f}_1(L_1/L_2, \mu_s, \mu_f), \text{ and} \tag{2.16}$$

$$F_p = \rho_d g z w L_{avg}\, \hat{f}_2(L_1/L_2, \mu_s, \mu_f). \tag{2.17}$$

For equal plates ($L_1 = L_2 = L = L_{avg}$) we obtain

$$s_p = L\, \hat{f}_1(\mu_s, \mu_f), \text{ and} \tag{2.18}$$

$$F_p = \rho_d g z w L\, \hat{f}_2(\mu_s, \mu_f). \tag{2.19}$$

Note that F_p has units of force per out-of-plane length. Also, note that under these relations, the only material properties that influence the peak force and separation are the friction coefficient(s) and density; the sole length scale comes from the plate itself. This makes physical sense when the smallest in-plane feature ($\min(w, L, s)$) is sufficiently larger than grain diameter. However, the exact value of O(1) needs to be calculated experimentally. Swapnil et al.[125] explored the dependence of force-peak

separation s_p/d with intruder size, L/d, when the intruder size is close to the grain diameter, d (L/d range 1–6). Interestingly, their data agree with our proposed linear dependence $s_p \propto L$ at intruder sizes as low as 3-4 grain diameters.

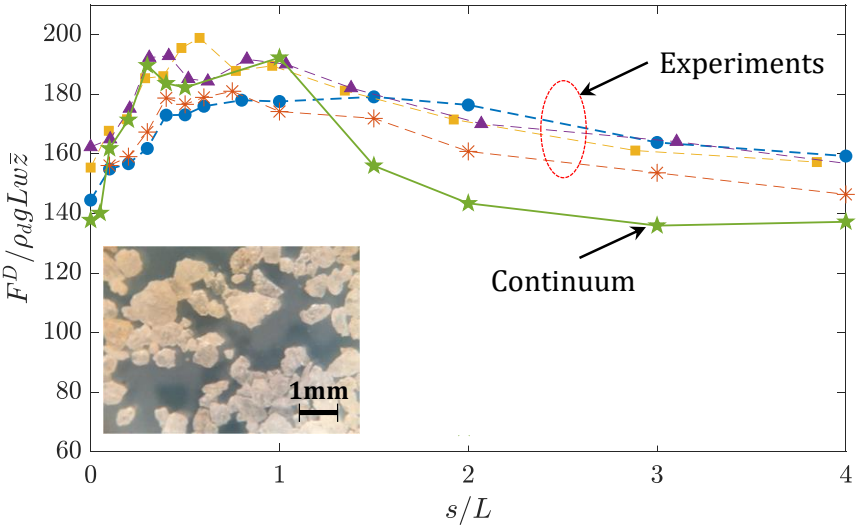

Figure 2-10: *Case 2: Experimental verification of peak force phenomenon in two-plate intrusions:*. The comparision of experimental data (dotted lines) and calibrated continuum simulations (solid line) for two (equal) plate intrusion experiments. The experiments use plates of width (L) 15 mm (blue data with • marker), 20 mm (orange data with $*$ marker), 26 mm (yellow data with ■ marker), 29 mm (violet data with ▲ marker), and the continumm model uses a plate of width 10 mm (green data with $\star$ marker). Quikrete Pool Filter Sand with grain density $\rho_g = 2520kg/m^3$ was used (inset shows microscopic view). The effective critical density ρ_c and angle of repose of the sand was found to be $1512kg/m^3$ and $36^o \pm 1$ resp. All of the paired plates have a $1:5$ horizontal aspect ratio. The continuum results correspond to plane-strain two plate intrusions with drag forces F^D averaged over a depth range of $0.06 - 0.08$ m for all the cases and an average depth, $\bar{z} = 0.07$ m, $w = 1$ m, $g = 9.8m/s^2$, $\rho_d = 1512kg/m^3 (= \rho_g * \phi)$ is used for scaling the vertical axis. The material properties are calibrated based on experimental data with ρ_g=2520 kg/m^3, $\phi = 0.6$, $\mu_s = 0.72$ ($=\tan^{-1}\theta_{repose}$). All these experiments were conducted by Andras Karsai under the guidance of Prof Daniel Goldman at Crab Lab, Georgia Institute of Technology.

We also verify these drag force variations and the peak separation scaling relation with new vertical intrusion experiments and compare them to calibrated continuum simulations (see figure 2-10 for the details). A DENSO VS087 robot arm intruded an apparatus that held pairs of steel plates at various separations into a bed of loosely

consolidated Quikrete Pool Filter Sand with grain density $\rho_g = 2520$ kg/m^3, and effective close-packed density $\rho_d = 1512$ kg/m^3. The internal friction value of this medium was $\mu_s = 0.72$ based on the angle of repose measurements from experimental tilting tests, with the media globally fluidized for 15 seconds to a loose initial packing fraction of $\phi \approx 0.58$ for all trials. All intrusions were performed at 11 mm/s, where speed dependence of the force response is negligible. Over 128 trials, the net resistive forces on the pair of intruding plates were measured using an ATI Mini40 force transducer. Andras Karsai from Prof Daniel Goldman's group at the Department of Physics at Georgia Institute of Technology conducted these experiments.

We observed a satisfactory match between the experiments and the simulations. The fact that the experimental data for different values of L collapse onto a single dimensionless master curve supports the robustness of the scaling relation implied by NDPM in eq 2.15. Additionally, we observe that although both 2-8(A) and Figure 2-10 show peaks in normalized force responses of the media at low separations, the shapes of the graphs are not 'identical'. This variation is expected because eq 2.15 indicates that the graph between normalized drag ($\tilde{F}$) and normalized separation (s/L) depends on material friction properties (μ_s and μ_f) and the two cases use different internal friction (μ_s) values.

We also briefly explore, in our simulations, the effect of changing plate width ratios on the peak separation distance (s_p), and the peak separation force (F_p) in our study (see figure 2-9A). We find that F_p monotonically decreases from a maximum value to F_∞ as the plate ratio decreases from 1 to 0 (note that plate-ratio L_1/L_2 is always ≤ 1 as $L_1 \leq L_2$ by definition). The normalized peak separation distance (s_p/L_{avg}) increases with decreasing plate-ratios (L_1/L_2). The peak separation relations are also expected to be a function of μ_s from scaling analysis (eq. 2.17). Thus, an in-depth shape and material property dependence characterization of this phenomenon are relegated to future study.

2.4.3 Case 3: Drag variations in the plowing of granular media

This case takes inspiration from the work of Gravish et al.[136] who studied drag force fluctuations in the plowing of granular beds at different initial packing fractions. A Discrete Element Method (DEM) based study of the case was also performed by Kobayakawa et al.[137]. Both of these studies observed increasing drag force fluctuations with an increasing initial packing fraction of the granular beds. Similar force fluctuations were observed by Kashizadeh and Hambleton [138] on reduced-order modeling of the plowing processes in sands and by Jin et al.[139] in the development

of a new single-gravity (1-g) small scale testing methodology. As this phenomenon directly relates to the changing density of the media, we use the more detailed DPM model for this case.

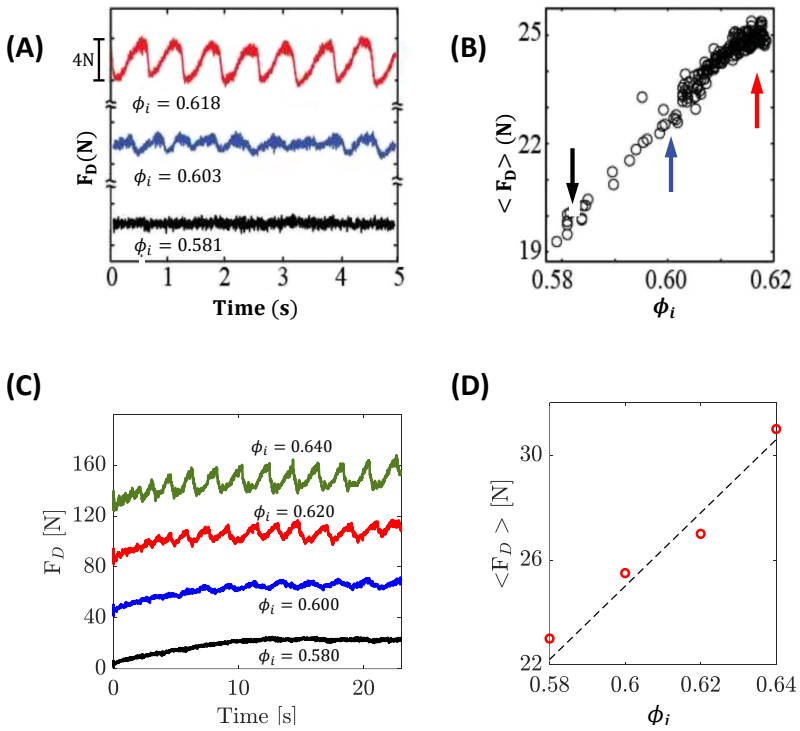

Figure 2-11: *Case 3: Force fluctuations during plowing (using DPM model)*: Variation of drag forces at various initial packing fractions in Gravish et al's [136] experiments: *(A)* time variation of drag forces, and *(B)* average drag forces. The average values of forces for three initial packing fractions in *(A)* are shown with corresponding colored arrows in *(B)*. *Corresponding continuum simulations: (D)* Time variation of drag forces (force plots for consecutive ϕ_i are shifted vertically by 0, 40, 80, and 120 N respectively for improved visualization), and *(E)* averaged drag forces. The simulations are plane-strain and glass bead properties are used for simulating granular media (ρ_g=2520 kg/m^3, $\phi_=$0.6, $\mu_c = 0.4$, $\chi = 5.0$, $\phi_{min} = 0.45$). See Movie S3 (refer to Appendix A.1) for visualizing time evolution of material front during plowing of under- and over-compacted media from experiments and simulations. Figure *(A)* and *(B)* are modified from Gravish et al [136].

A schematic representation of this case is given in Figure 2-2C. Both of the reported studies were performed in 3D, while our simulations are 2D plane-strain. Characterizing the effects of this difference in our studies is difficult, so we do not attempt an exact match. Nevertheless, we do expect the 2D simulations to capture

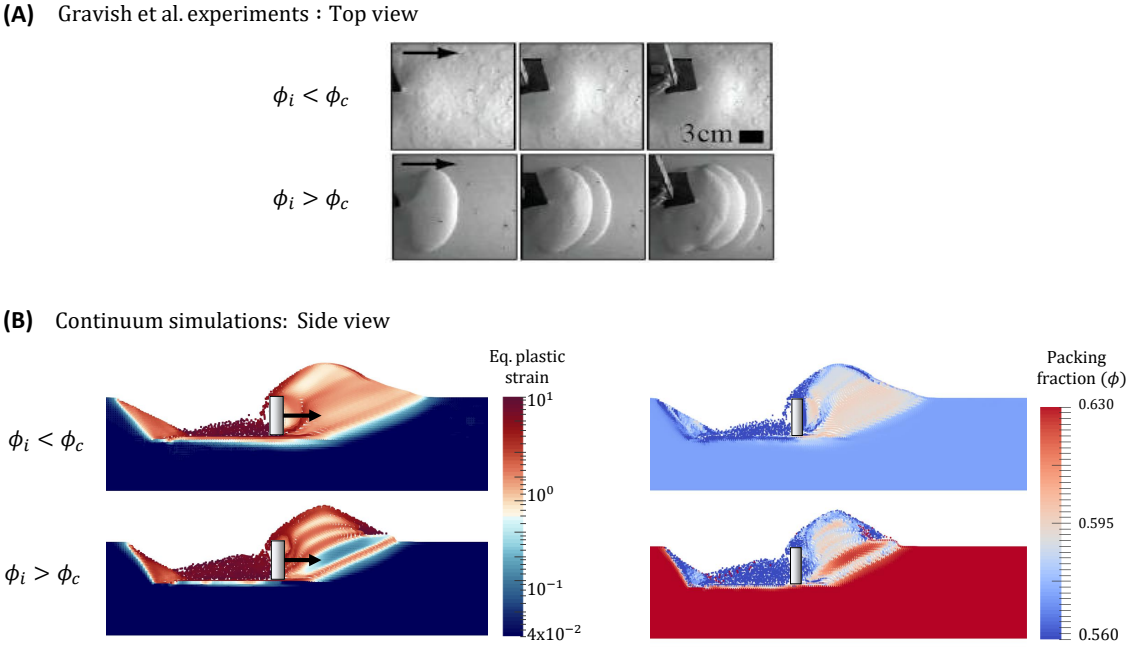

Figure 2-12: *Case 3: Force fluctuations during plowing (using DPM model)*: Visualisation of the free surface in under/over compacted granular media: top view from Gravish et al's [136] experiments *(A)*, and side view in continuum simulations *(B,left)*. *(B,right)* Variation of material packing fraction from continuum modeling simulations in initially under-compacted ($\phi_i = 0.57$) and over-compacted ($\phi_i = 0.63$) media cases considered in *(B, left)*. The simulations are plane-strain and glass bead properties are used for simulating granular media (ρ_g=2520 kg/m^3, $\phi_=$0.6, $\mu_c = 0.4$, $\chi = 5.0$, $\phi_{min} = 0.45$). See Movie S3 (refer to Appendix A.1) for visualizing time evolution of material front during plowing of under- and over-compacted media from experiments and simulations. Figure *(A)* are modified from Gravish et al [136]. [Photo credits: (A) N. Gravish, P. B. Umbanhowar and D. I. Goldman, Georgia Institute of Technology]

the phenomenon qualitatively and the drag forces to be similar in their magnitudes. We once again use the glass bead material properties used in the previous case. We use a grain density ρ_g of 2520 kg/m^3, a critical packing fraction ϕ_c of 0.60, a steady-state critical internal friction μ_c of 0.4, and a scaling coefficient χ of 2.5. Similar to previous cases, the plates are modeled as elastic bodies with high elastic modulus to act as rigid bodies. The media/plate interface friction (μ_f) was set to 0.35. We use a 2.4 m $\times$ 0.4 m granular bed, and a 4×10^{-3} m spatial resolution (Δx) for simulating these cases. The plowing plate dimensions are 0.03×0.08 m^2.

Figure 2-11 and 2-12 shows the variation of horizontal drag forces from the Gravish et al.[136] experiments alongside our continuum simulations. The continuum results are scaled proportionally to the out-of-plane width in Gravish et al.[136]. The mean drag force and force fluctuations from continuum modeling are plotted in Figure 2-11C and D, showing smooth forces transition to larger, fluctuating forces as the initial packing fraction rises above ϕ_c. The same trends can be seen in experiments, c.f. Figure 2-11A and B. A visual free surface comparison between experiments and the simulations also shows the similarity of flows as ϕ_i varies, c.f. Figure 2-12A and B. In the over-compacted case, the continuum results show a stepped pattern forming on the surface, but it is not as persistent as the wavy patterns observed in the experiments. This is due to the 2D nature of our simulations. The 2D nature restricts the material from flowing in an out-of-plane direction, which causes the material to flow over the existing waves and overrun the wavy patterns. Such patterns are otherwise not overrun in 3D experiments and are more visible in over-compacted cases.

The observed shear patterns, free-surface profiles, and force fluctuations shown in Figure 2-11A,B are in accord with the shear-softening (shear-strengthening) of over-compacted (under-compacted) granular media that is built-in to the DPM model. In a sample initially under-compacted ($\phi_i < \phi_c$), shear deformations cause compaction, resulting in higher densities along the sheared regions than in bulk (see eq.2.5). This density increase results in higher shear strength along the shear zone (see eq.2.4). Thus, further loading in such systems induces shear to occur in the weaker material adjacent to the shear band, which effectively spreads the shearing in such systems. On the other hand, in the over-compacted case, shear deformations dilate the material, resulting in lower density in the sheared region than in bulk, which results in lower shear strength there. Hence, continued loading causes shear to accumulate along the thin zone of initial failure causing the appearance of a strong shear band. This process continues until the total force requirement for shearing along the existing band exceeds that for creating a new shear band in bulk (after which the same process repeats itself). Thus, in over-compacted media, a visually separable shear band formation pattern occurs (Figure 2-12B (left)). In initially over-compacted cases ($\phi_i > \phi_c$), increasing the initial packing fraction of the media results in an increased plate motion requirement between successive shear band formations (due to increased strength of the media in bulk) and thus the force fluctuation magnitudes increase (and their spatial frequency decreases) with increasing packing fraction (also observed by Gravish et al.[136]). We also plot the variation of the packing fraction in the media from continuum modeling in figure 2-12B (right). The figure provides a visualization of changing packing fraction ahead of the plate in accordance with the smooth versus banded mechanism explained above.

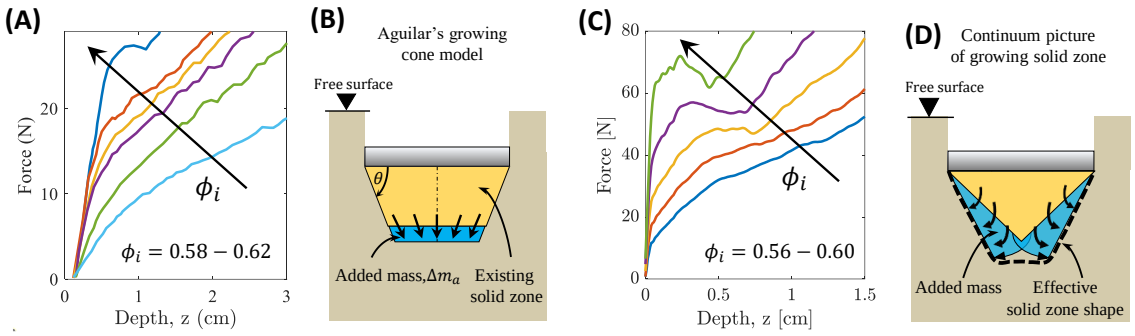

Figure 2-13: *Case 4: Material front development during vertical intrusion (using DPM model): (A)* Experimental data from Aguilar and Goldman [133]. The experiments intruded a circular plate of 0.051 m diameter into poppy seeds (ρ_g = 1100 kg/m^3) at various initial packing fractions (ϕ_i). *(B)* Schematic of Aguilar and Goldman's cone growth model[133]. *(C) Continuum modeling results:* Force data from 2D plane-strain simulations. We intrude 0.04 m wide flat plates into a granular material with ρ_g = 1100 kg/m^3, μ_c = 0.53, ϕ_c = 0.60, χ = 5.0, and ρ_{min} = 0.45. *(D)* Mechanism of solid zone development from continuum modeling.

2.4.4 Case 4: Shear deformation zone in plate intrusions

This last case takes inspiration from the work of Aguilar and Goldman [133] and highlights the capability of the basic DPM model in capturing the *development* of the flow profile during vertical intrusion of single plates. A schematic representation of the case is given in Figure 2-2D. Aguilar and Goldman [133] postulated that the formation of a rigid No Shear Zone (NSZ) ahead of a flat plate during vertical intrusion is an incremental growth process. In three dimensions, this growth takes the form of a rigid frustum shape which grows from a low height frustum with a fixed base (matching the shape of the intruder) to a fully developed cone/pyramid at the completion of the mechanism. For a circular base, the final shape is a cone. In two dimensions, like our case, this would translate to successive isosceles trapezoids (with larger parallel edges matching the intruder's intruding edge), leading to a wedge shape with the base as the intruder's leading edge.

Figure 2-13 and 2-14 shows the variation of intrusion forces and successive velocity profiles in under-compacted granular intrusion experiments compared to our continuum simulations. We model the granular media, poppy seeds, with the DPM to incorporate the effect of density transitions. We use material properties for poppy seeds with a grain density ρ_g=1100 kg/m^3, a critical packing fraction ϕ_c=0.60, a steady-state critical internal friction μ_c=0.53, and a scaling coefficient χ=5.0. The media/plate interface friction (μ_f) was set to 0.35. We use a 0.5 m $\times$ 0.2 m granular bed, and a 5×10^{-4} m spatial resolution (Δx) for simulating these cases. The

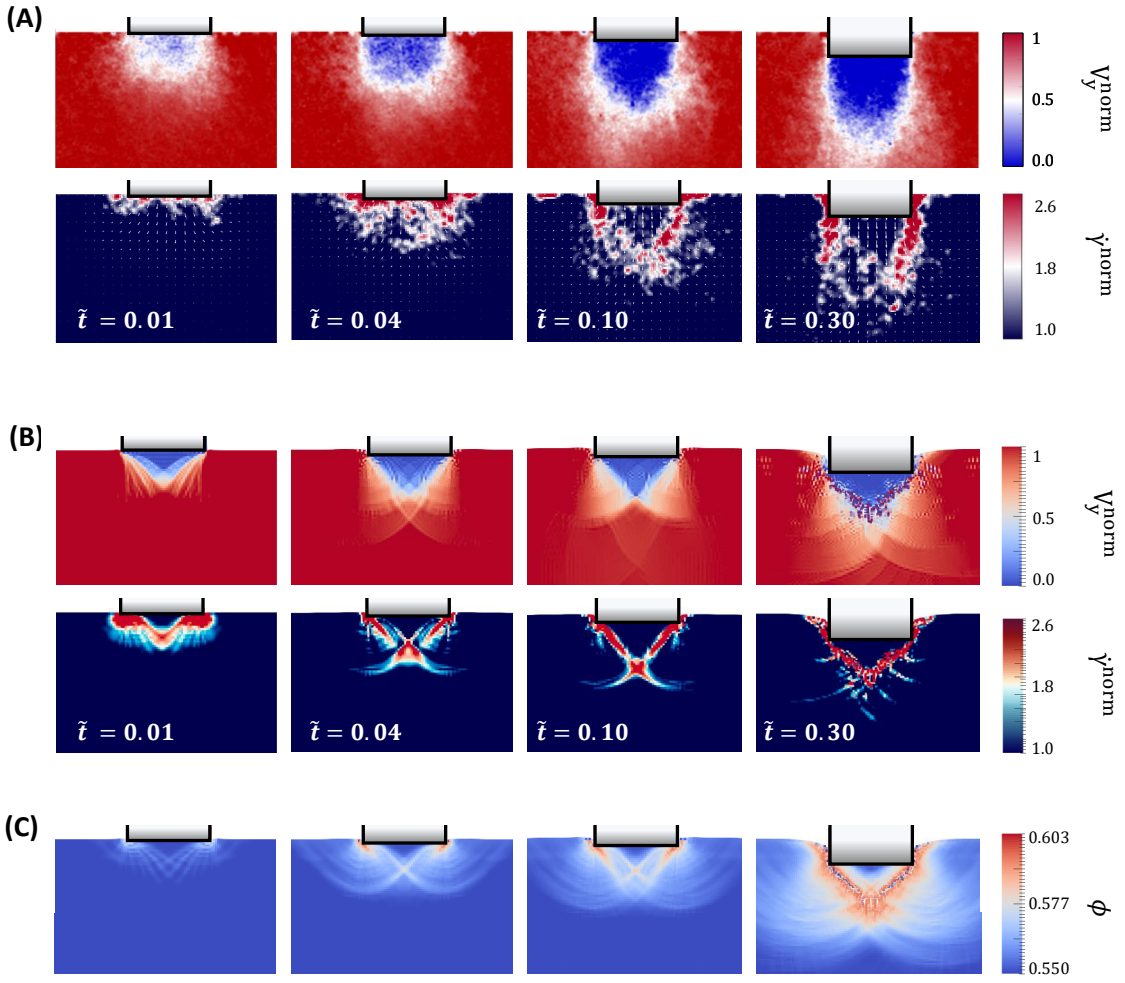

Figure 2-14: *Case 4: Material front development during vertical intrusion (using DPM model): (A)* PIV analysis of constant speed plate intrusions. New set of experiments were conducted by intruding $L = 40$ mm wide rectangular flat plates at a constant low speed, $v = 150$mm/s, in loosely packed poppy seeds. Time is non-dimensionalized ($\tilde{t} = t/t_o$) by $t_o \equiv L/v$. The velocity is normalized by intrusion speed, v, and strain rates by $\dot{\gamma}_o \equiv 1/t_0$. We plot these results in the intruder's frame of reference. *(B) MPM simulation results:* Vertical velocity and equivalent plastic strain rate fields during vertical intrusion in initially under-compacted media ($\phi_i = 0.55$) for material properties discussed in *Figure 2-13C*. We also show the evolution of packing fraction (ϕ) from continuum modeling in *Figure 2-13C*. See Movie S4 (refer to Appendix A.1) for visualizing material flow at various ϕ_i

intruding plate dimensions are 0.04 m $\times$ 0.02 m.

The force trends from simulation qualitatively match the trends from Aguilar's experiments (compare Figure 2-13A to 2-13C), keeping in mind that Aguilar uses a 3D circular plate while our simulations are in 2D plane-strain. In a set of separate experiments using a rectangular plate intruder and PIV (Figure 2-14A) we observed the flow zone development appears similar to continuum results (Figure 2-14B). These trends also agree with general observations from a 3D DEM study done by Feng et al.[140]. The Aguilar and Goldman [133] study presents a model whereby the rigid cone emerges from a growing rigid frustum of constant base angle that gets progressively longer until converging to the final cone shape (Figure 2-13B). However, in our simulations, the zone actually starts as a 'short' wedge coincident with the plate bottom, having a large apex angle (expected by a slip-line theory to be approximately $\pi/2 - \tan^{-1}\mu_i$ for μ_i the friction at the initial density) due to the low initial packing fraction of the media. The rigid front then grows by 'fanning out' from the diagonal edges (see Figure 2-13D), as the edges represent the zone experiencing maximum shear-compaction and hence the most strengthening. This growth can be observed as well from density variations, shown in Figure 2-14C. The growing density of the region results in an increasing but variable internal friction value in the zone below the intruder and results in the development of a progressively sharpening, quasi-rigid trapezoid-like shape under the plate. As the intruder moves deeper, the process converges to a final wedge shape (with a sharper angle equal to '$(\pi/2 - \tan^{-1}\mu_c)/2$'). Thus the DPM model provides an apt description of the observed behavior in under compacted granular intrusion.

2.5 Approach limitations and their implications

While the continuum modeling and the numerical implementation we use in this study are able to represent the considered cases to a sufficient degree, both the model and the method have their limitations. Clearly, as emphasized in the introduction, the phenomena incorporated in a constitutive model limit the behavior the model can capture, and the constitutive relations we use here intentionally exclude certain effects for the benefit of simplicity. Similarly, MPM has known accuracy limitations given by choice of the grid resolution, material point density, shape functions, and the means of representing contact between domains. For instance, MPM inherently captures a volume average material response everywhere. If during the flow, an element has a low number of interior material points, the accuracy of the integration is also diminished. But these issues can be overcome with an appropriate choice of shape functions and refined discretization. Specifically for these issues, use of more advanced methods such as the hybrid DEM-MPM approach (such as Yue et al. [55] and Chen et al. [141]) or dynamic particle enrichment (such as Zhu et al.[142])

could be used at the expanse of computation time. The use of smoother and wider shape functions could also help decrease numerical fluctuations often observed in MPM[143].

2.6 Conclusion

In this work, we demonstrated the efficacy of continuum modeling in four cases using two continuum descriptions of granular media, of forced granular intrusion — (1) depth-dependent force response in horizontal submerged intruder motion; (2) separation-dependent drag variation in parallel plate vertical in-trusion; (3) initial density-dependent drag fluctuations in free-surface plowing; and (4) flow zone development in vertical plate intrusions in under compacted granular media (see Figure 2-2). The study shows that relatively simple, friction-based plasticity models capture a large variety of granular intrusion phenomena.

Moreover, the models provide a useful macroscopic understanding of granular intrusion processes, which are often primary interests in engineering applications, and remove the additional complexity of trying to determine large-scale physics from grain-scale observations. The simplicity of these continuum models also streamlines this understanding, both by exclusion – i.e. if such a model works, it implies that mechanisms or effects lying outside the model's formulation are not crucial to the outcome – and by admitting simple scaling analyses as we have utilized throughout. Such simplifications will certainly limit the accuracy of these models in a variety of cases, but an incremental approach of adding physical augmentations (such as micro-inertial effects, particle size effects, or evolving fabric variables) provides a systematic approach for exploring the underlying physics in diverse cases. For instance, we do not use $\mu(I)$ rheology in either of the models in this study; the fact that our modeling still captures the observed behaviors indicates micro-inertial effects are not a key mechanism in the observed behaviors.

In the future, the work could be extended to three dimensions to compare the computational advantage of using such methods extensively. Furthermore, the continuum treatment could help reconcile granular behavior with similar behaviors observed in other, more standard continua. For example, Minetti et al.[144] reported that during swimming in the water, slight separation between fingers increases propulsive thrust, similar to our observation for slightly separated granular intruders [144, 145]. Comparing and analyzing continuum forms could provide insights into the rationale behind such similarities, as was done in other flow resistance studies[146].

We use the results of this work in multiple ways. In this study, we notice that despite it's simplicity, the continuum approach models a large variety of granular intrusions. Additionally, the approach provides fine control on phenomenologies included in its form. This feature is extremely useful in systematically developing further-reduced models. We use the NDPM model from this study for developing a generalized, rate-dependent, Dynamic Resistive Force Theory for the rapid intrusion of intruders (more details in Chapter 4). We also use a three-dimensional implementation of the NDPM model to develop a 3D version of RFT (more details in Chapter 5).

Chapter 3

Reduced-order modeling of granular intrusions with RFT

3.1 Introduction

The remaining half of this thesis discusses two versions of Resistive Force Theory (RFT) developed in this thesis work. This chapter provides an in-depth discussion of 2D-RFT for providing readers with a comprehensive understanding of this approach which is crucial for understanding enhanced versions of RFT.

The RFT methodology, which was originally introduced by Gray and Hancock [89] for modeling self-propelling undulatory biological systems in viscous fluids, has gained a lot of attention in the field of granular physics in recent decades. On the lines of fluid RFT, granular RFT assumes that the net forces on any arbitrarily shaped body moving through granular media at low speeds can be obtained by summing up forces on individual sub-surfaces and that these sub-surface forces can be independently obtained using an empirical formula that depends on sub-surface size, velocity, the sub-surface state in the media, and a few variables characterizing the media-surface interactions, without full-scale numerical modeling of the granular system. Thus, the theory assumes superposition and decoupling of forces over the sub-surfaces of a large body [91, 92, 93]. Figure 3-1 and eq 3.1 shows a plane strain version of RFT for granular media (2D-RFT) proposed by Li et al. [93].

$$\begin{aligned}[f_x, f_z] &= \int_{Surf} ((\alpha_x(\beta,\gamma), \alpha_z(\beta,\gamma))H(-z)|z|\mathrm{d}s \\ &= \sum_{i=1}^{N} [\alpha_x(\beta_i,\gamma_i), \alpha_z(\beta_i,\gamma_i)]H(-z_i)|z_i|\mathrm{d}s_i \end{aligned} \tag{3.1}$$

where sub-script i represents i^{th} sub-surface of the body. $H(z)$ is the Heaviside function representing force go to zero when a sub-surface lies above free surface ($z_i > 0$). α_x and α_z represent force per unit area per unit depth in the above equation. ds represents the area of a sub-surface and $|z|$ represents the depth below the free-surface.

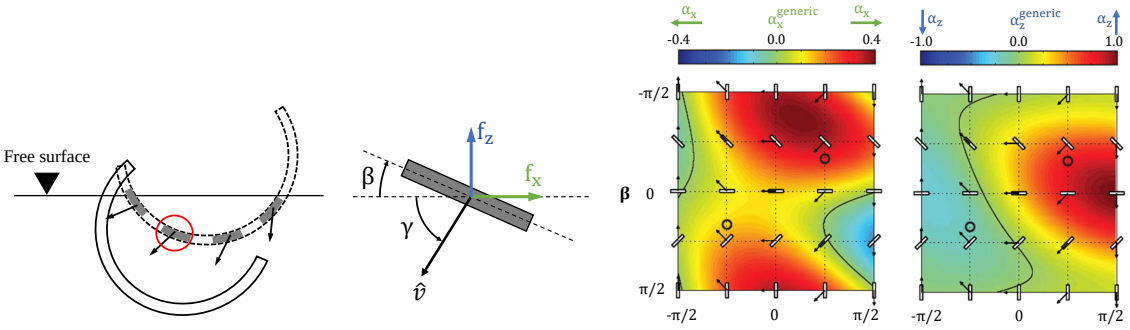

Figure 3-1: *(A)* Characterization of a sub-surface with two characteristic angles in 2D RFT. β represents the plate tilt angle and γ represents the plate velocity direction. *(B)* Generic form of force per unit area per unit depth ($\alpha_{x,z}^{\text{generic}}$) in 2D RFT (proposed by Li et al.[93])

In the above form, RFT takes an empirical approach by determining α_x and α_z functions through repeated slow experimental intrusions of a small flat plate submerged a unit depth in the tested media at various orientations and velocity directions. These orientations are characterised with angle β and the velocity directions are charaterised with angle γ (figure 3-1(A)). The repeated experiments create a force diagram from force measurements for these angled surface elements (figure 3-1(B)). These small elements are assumed to obey linear superposition and can be applied to any desired intrusion surface. Thus, this simple closed-form equation makes granular RFT a useful tool for estimating the forces on both submerged and intruding bodies in granular media. Functions α_x and α_z represent force/area/depth on any sub-surface in x and z-directions respectively. While the original dependence of $\alpha_{x,z}$ was obtained in the form of experimental data, Li et al [93] also observed that variations of $\alpha_{x,z}$ over $\{\beta, \gamma\}$ space are approxiately identical for most of the non-cohesive materials, differing only by a scalar multiplicative grain-structure interaction parameter, ξ. Thus, for any material-surface combination, functions $\alpha_{x,z}$ could be split into $\alpha_{x,z}^{gen}$ and ξ as:

$$\alpha_{x,z} = \xi * \alpha_{x,z}^{gen} \tag{3.2}$$

$$\alpha_z^{gen} = \sum_{m=-1}^{1}\sum_{n=0}^{1}[A_{m,n}cos2\pi(\frac{m\beta}{\pi} + \frac{n\gamma}{2\pi}) + B_{m,n}sin2\pi(\frac{m\beta}{\pi} + \frac{n\gamma}{2\pi})] \tag{3.3}$$

$$\alpha_x^{gen} = \sum_{m=-1}^{1}\sum_{n=0}^{1}[C_{m,n}cos2\pi(\frac{m\beta}{\pi} + \frac{n\gamma}{2\pi}) + D_{m,n}sin2\pi(\frac{m\beta}{\pi} + \frac{n\gamma}{2\pi})] \tag{3.4}$$

where all the coefficients ($A_{i,j}, B_{i,j}, \text{and} C_{i,j}$) except the following are zero:

Table 3.1: Generic values of fitting parameters in analytic form of RFT

Parameter	$A_{0,0}$	$A_{1,0}$	$B_{1,1}$	$B_{0,1}$	$B_{-1,1}$	$C_{1,1}$	$C_{0,1}$	$C_{-1,1}$	$D_{1,0}$
Values	0.206	0.169	0.212	0.358	0.055	-0.124	0.253	0.007	0.088

The 2D granular RFT has found many successess in modeling granular intrusions at low speeds. As we will discuss in chapter 5, the theory can be more generally expressed as:

$$\boldsymbol{F}_{\text{total}} = \int_{\text{surf}} \boldsymbol{\alpha}_{x,y,z}^{\text{mat}}(\hat{\boldsymbol{n}}, \hat{\boldsymbol{v}}, \boldsymbol{g})|\boldsymbol{z}|ds \tag{3.5}$$

Where, $\mathbf{F}_{\text{total}}$ represents the total integrated forces on a large surface which is divided into smaller plane sub-surfaces of area ds and mean depth $|\boldsymbol{z}|$ from the free surface. The $\boldsymbol{\alpha}_{x,y,z}^{\text{mat}}$ functions represent the force per unit area per unit depth and are functions of the surface normal $\hat{\boldsymbol{n}}$, velocity direction $\hat{\boldsymbol{v}}$, gravity $\boldsymbol{g}$, and the properties of the material and material-surface interaction. The heavyside function H from eq 3.1 is dropped in eq 5.2 in the interest of simplicity and obviousness. The local force (integrant) on sub-surfaces are extracted independently from each other at varying depths($|z|$) and orientations ($\hat{\boldsymbol{n}}$). The calculation of the net intruding force on the body using a linear sum of forces on surface elements is a result of the localization [91] and decoupling of force fields on intruder sub-surfaces. A comprehensive comparison of various existing reduced-order methods for modeling granular intrusions, including 2D-RFT and a *terramechanical* model, can be referred from Agarwal et al. [95].

3.2 RFT implementation

The following sections briefly discusses the step-by-step procedure for implementing RFT for modeling motion of an arbitrary body. Figure 3-2 shows a few examples of

granular intrusions modeled with 2D-RFT:

1. Body surfaces are discretized into smaller sub-elements that as a whole, approximate the total geometry.

2. For each sub-surface, if $\hat{\boldsymbol{v}} \cdot \hat{\boldsymbol{n}} \geq 0$ and $z < 0$ (surface is a leading edge and lies below free surface), steps 3-6 are repeated to find sub-surface forces. Else the sub-surface forces are set to zero.

3. For each sub-surface, the orientation angle (β), velocity angle (γ), effective depth from the free surface ($|z|$), and area (ds) are calculated.

4. The values of $\boldsymbol{\alpha}_{x,z}^{\text{gen}}$ are calculated using β and γ from eq 3.3-3.4 for each sub-surface.

5. Media specific $\boldsymbol{\alpha}_{x,z}$ are calculated using eq 3.2.

6. $\boldsymbol{\alpha}_{x,z}$ are multiplied with $|z|$, and ds to calculate forces on each sub-surface.

7. The net resistive force on the body is calculated by adding forces on all the sub-surfaces using RFT assumptions of additivity of granular resistive forces eq 3.1.

8. A momentum balance in the x and z coordinates then models the body's motion in the horizontal and vertical direction.

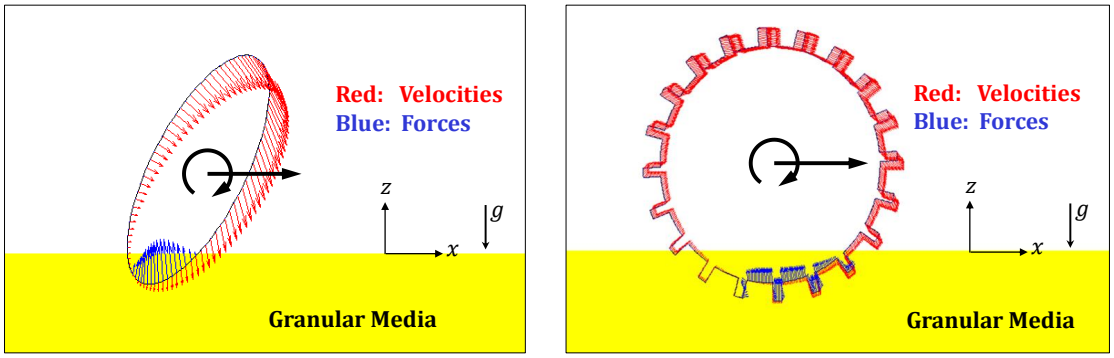

Figure 3-2: Examples of an elliptical (left) and a grousered wheel (right) under forced-rotation (fixed rotation and horizontal-translation speed) modeled using RFT implementation discussed in secttion 3.2. Blue arrows show the scaled forces and red arrows show scaled local velocities.

3.3 Open source app for granular intrusion modeling with RFT

An open-source, Matlab-based implementation of granular 2D-RFT developed as a part of this thesis can be downloaded from the following link [1]. The app allows for modeling motion of arbitrary shapes imported as images in the app using RFT calculations discussed in section 3.2. Figure 3-3 shows a snapshot of the app interface. The app allows for constrained as well as free locomotion scenarios. In addition to conventional RFT, the app also allows adding a macro inertia term ρv^2, with the desired scaling value, at each sub-surface (see section 4.6.1 for more details). Readers can find more details at the provided link.

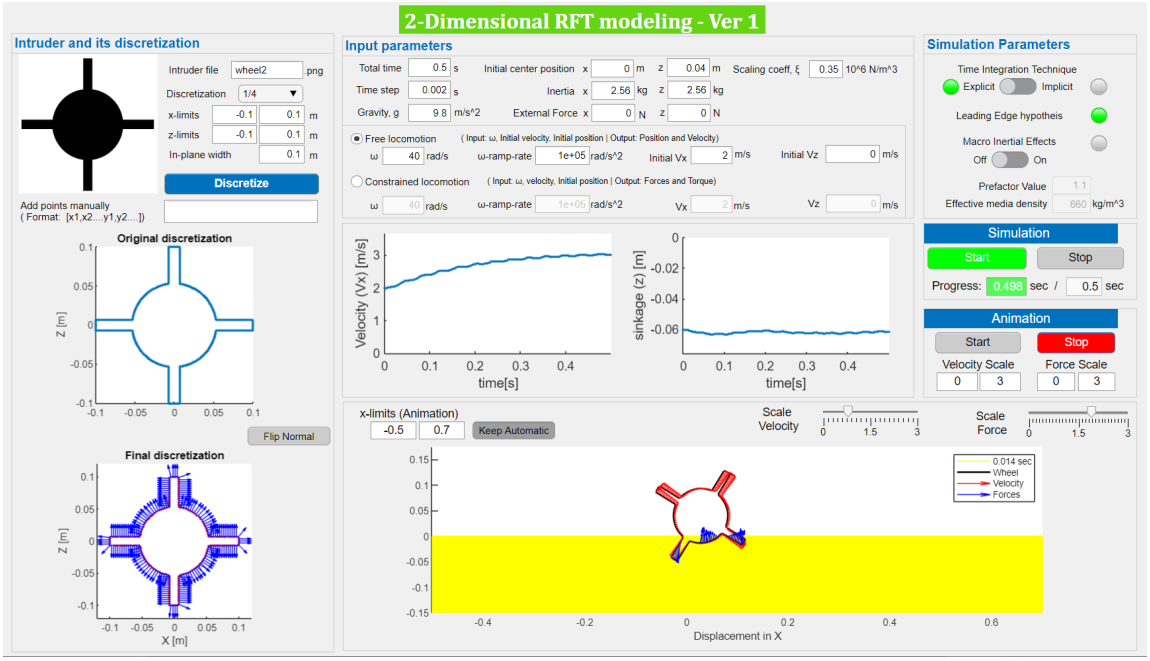

Figure 3-3: Interface of Matlab based RFT app for modeling arbitrary intrusions of arbitrary shaped bodies using RFT. The app allows for inputing arbitrary shapes as image files and uses implementation discussed in secttion 3.2

[1] https://www.mathworks.com/matlabcentral/fileexchange/75389-reduced-order-granular-intrusion-modeling-using-rft?s_tid=prof_contriblnk

Chapter 4

Extending resistive force theory to high-speed regimes: Dynamic Resistive Force Theory

Granular intrusions, such as dynamic impact or wheel locomotion, are complex multiphase phenomena where the grains exhibit solid-like and fluid-like characteristics together with an ejected gas-like phase. Such phenomena are even more pronounced at high speeds. Despite decades of modeling efforts, a unified description of the physics in such intrusions is as yet unknown. Work in this chapter makes use of a continuum model (NDPM), which uses simple notions of frictional flow and tension-free separation to describe complex granular intrusions near free surfaces to capture media flow dynamics in a variety of high-speed granular intrusion experiments, including wheel locomotion, plate intrusions, and running legged robots. The model reveals that three effects (a static contribution and two dynamic ones) primarily give rise to intrusion forces in such scenarios. Identification of these effects enables the development of the further reduced-order technique, Dynamic Resistive Force Theory (DRFT), for rapid modeling of granular locomotion of arbitrarily shaped intruders. The continuum-motivated strategy we propose in this chapter for identifying physical mechanisms and corresponding reduced-order relations has potential use for a variety of other materials.

4.1 Introduction

A common granular intrusion involves a rigid or flexible solid penetrating into the media and using the resistive force to propel itself into a state of locomotion (see Figure 4-1). If a body slowly intrudes into granular beds, granular stress arises independent of the intrusion rate, and the resistive force on the intruding body remains

in the quasistatic limit [53, 54, 94]. However, various intrusion scenarios can arise which deform the media rapidly enough that the net force response, and hence the locomotive behavior, is affected. Examples of such intrusions include ballistics, meteor impacts, rapid locomotion, and many industrial processes [147, 148, 149, 2, 150].

Rigid wheel locomotion is a great example of a system that combines these effects, exhibiting multiphase granular behavior, complex grain-surface interactions, and re-interaction with deformed media. Rigid wheels like those found in planetary rovers continuously shear and sometimes violently deform the local media [80] to locomote in loosely consolidated terrain. These intrusions, particularly in high-velocity cases, cause the substrate material to behavior to deviate significantly from its quasistatic response, driven by potentially non-trivial surface interactions with the wheel. Thus, we first focus on rigid wheel locomotion as a diagnostic scenario of complex intrusion, which includes a wide array of non-trivial effects.

Figure 4-1: **Examples of high speed locomotion on granular surfaces:** *(A)* Wheel of the Curiosity Mars rover (Diameter $\sim$ 50 cm) [151] *(B)* running human [152], *(C)* RHex C-legged robot (C-leg limb length $\sim$ 18 cm) [153], and *(D)* a racing dirt bike (Diameter $\sim$ 50 cm)[154]. [Photo credits: *(A)* MAHLI imager Curiosity, NASA; *(B)* A. Singh, www.pexels.com; *(C)* G. C. Haynes, A. M. Johnson, and D. E. Koditschek, University of Pennsylvania; *(D)* Daniel, www.pexels.com] .

We use the continuum framework for NDPM model introduced in Chapter 2 section 2.2.2 based on a frictional-plastic yield condition and free separation for modeling granular media in these systems with the Material Point Method (MPM) (more details in section 2.3). Our intrusion analysis begins with a focus on circular

wheels with grousers — grousers are finite-sized radial protrusions along the wheel circumference, which facilitate traction (See figure 4-2A, 4-6A, Table 4.1 for more details). Grousered wheels are commonly used in granular locomotion applications in soft terrain [155, 95, 156, 157, 80]. We model and experiment with the motion of these wheels on poppy seeds, the granular media in this work (more details in Table 4.2). Alongside scenarios of slow and rapid wheeled locomotion, two additional families of test cases, submerged lateral plate intrusion, and "four-flap runners" are simulated and compared to known results in the literature to verify the model's ability to capture dynamics of complex granular intrusions. Interestingly, the NDPM model captures the non-trivial rate-dependent phenomena exhibited in complex intrusions even though its constitutive equations are *rate-independent*. In addition to developing a high-speed RFT, this work shows how a single continuum interpretation of the media (NDPM) can represent multiple intrusion scenarios by implicitly reconciling various inertial effects.

Table 4.1: Grousered wheel dimensions †

1. Inner Diameter, D	188 mm	2. Wheel width, W	140 mm
3. Grouser height, h_g	12 mm	4. Grouser width, w_g	6 mm
5. Gravity, g	9.8 kg/m^2	6. Number of grousers, N	20
7. Effective horiz. inertia	23.0 kg	8. Effective vert. inertia	6.3 kg

† A constant forward force of 4 N was also applied on the grousered wheel MPM simulations to calibrate them with the friction-compensating mechanism used in the experiments.

Table 4.2: Granular media (Poppy seeds, PS) properties

1. Density, ρ_{grain}	1100 kg/m^3
2. Critical packing fraction, ϕ_c	0.58
3. Internal friction, μ (2D,MPM)*	0.56
4. Wheel-PS surface friction (2D,MPM)	0.35
5. RFT scaling coefficient, ξ	0.35

* The internal friction (μ) for the PS was obtained by calibrating the sinkage of the grousered wheel between MPM simulations and experiments, at low angular velocity (10 RPM) where the system is known to display in quasi-static character.

In addition to capturing full-field characteristics of wheel locomotion, we obtain a global-level physical understanding of intrusion dynamics by analyzing plasticity

solutions, which guides the development of a reduced-order model for intrusion that we call the Dynamic Resistive Force Theory (DRFT). We show that DRFT accurately models all the considered granular intrusion cases. By combining existing literature, continuum modeling, and experimental verification, we identify the relevant physics that go into DRFT and its interpretation as corrections to an existing quasistatic RFT model [93, 92, 95] for slow intrusion. Key effects that generate rate-dependent behaviors are identified, and, once incorporated, DRFT allows rapid calculation of the expected resistive forces in the media.

4.2 Wheel locomotion experiments

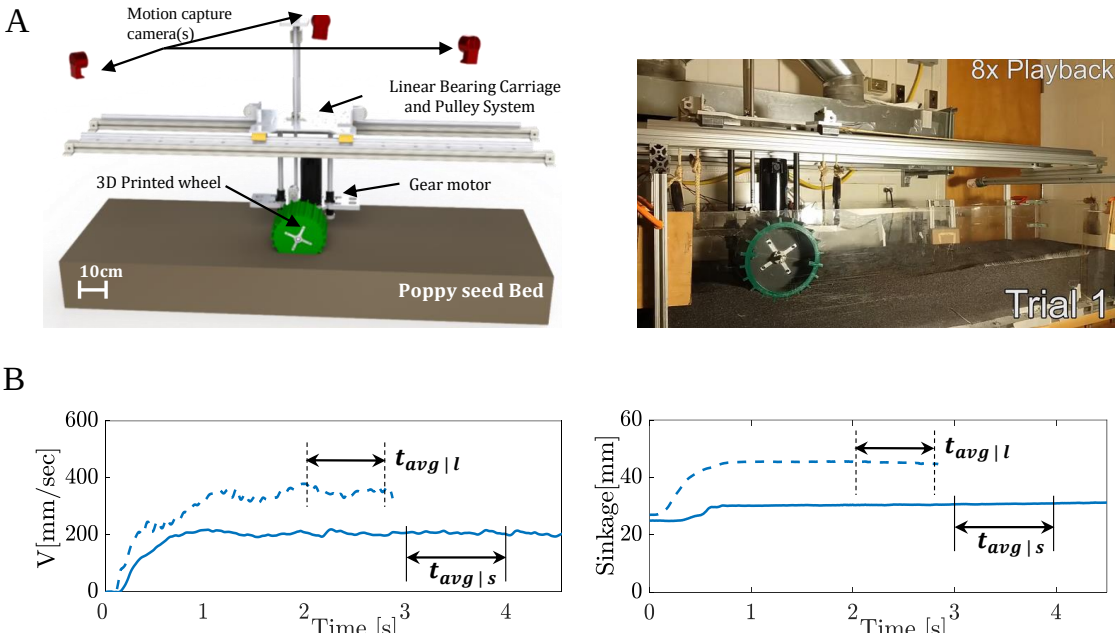

Figure 4-2: **Setup for rigid-wheel experiments (Andras Karsai, GeorgiaTech):** *(A)* CAD model (left), and a snapshot (right) of the experimental setup at Crab Lab GeorgiaTech used in this study. *(B)* Sample experimental time series data for translation velocity (left) and sinkage (right) at low ω (20 RPM, solid lines) and high ω (50 RPM, dotted lines) respectively. $t_{avg|s}$ and $t_{avg|l}$ show the time windows used for avergaing low and high ω data, respectively.

Figure 4-2A shows a CAD model and a snapshot of the laboratory setup used for performing wheeled locomotion experiments in this study, and Figure 4-2B indicates our data collection methodology. To perform systematic experiments of free-wheel locomotion, a simple, automated 'terramechanics testbed' was built. A powerful

gear motor (capable of providing up to 70 RPM at 14.1 Nm) was mounted in a carriage (Figure 4-2A and B), which moves freely along vertical and horizontal linear bearings. The effective vertical loading of the wheels was controlled through a combination of weights and pulleys. The system ran trials in a fluidizing bed of poppy seeds (a dry non-cohesive granular media) across a bed length of 1 m, allowing for controlled resets of terrain by blowing air up from the bottom. The poppy seeds acted as the representative material for the class of non-cohesive granular materials in our study. We specifically chose them due to the ease of running wheel locomotion experiments within them and previous experience using RFT. This fluidization redistributed the grains evenly into a homogeneous medium after each experiment, giving nearly identical terrain for each test [158]. Along with the terrain fluidization, the testbed also had the capability to reset itself: after each run, a linear actuator and a winch work together to drag the wheel carriage back to its starting position. Various system dimensions/specifications are listed in Table 4.1 and 4.2.

For experimental visualization of the granular flow around the wheels (Figure 4-5A), we also perform PIV analysis of the wheel locomotion at different ω values. The wheel was placed adjacent to the transparent side wall of the poppy seed container and performed the locomotion trials. Images of the flow field were captured with an AOS high-speed camera mounted on a tripod at a resolution of 1280x1024 and a framerate of 500 FPS. We expect minor variations in the flow fields due to the friction experienced by the material flowing next to the sidewall. The open-source PIVLab package was used in MATLAB for the analysis. Readers can refer to Movie S3 in the Supplemental Information at the end of this chapter for more details. The experimental part of both the above activities was also done by Andras Karsai from the department of Physics at Georgia Institute of Technology.

Figure 4-4A and B shows the trends of steady-state translation velocity and sinkage (resp.) with increasing angular velocity for a grousered wheel's free locomotion. Experiments indicate the emergence of a rate-dependent effect in wheel locomotion; an increase in slipping, accompanied by an increase in the sinkage of the wheels, breaks the linear trend in velocity vs. ω seen in the quasistatic domain of $\omega < 30$ RPM (corresponding to $\omega/\omega_o < 0.46$ in Fig 4-4A).

4.3 Continuum modeling of high-speed granular intrusions

We use the NDPM continuum model (introduced in Chapter 2 section 2.2.2) for modeling poppy seeds (PS), the granular media used in this study. We use the Material Point Method (MPM) (more details in section 2.3) for implementation. The

Figure 4-3: A sample high-speed rigid-wheel continuum simulations using MPM. The field being plotted is the equivalent plastic strain-rate.

material properties are provided in Table 4.2. Figure 4-3 shows a sample of wheel locomotion simulation performed with continuum modeling.

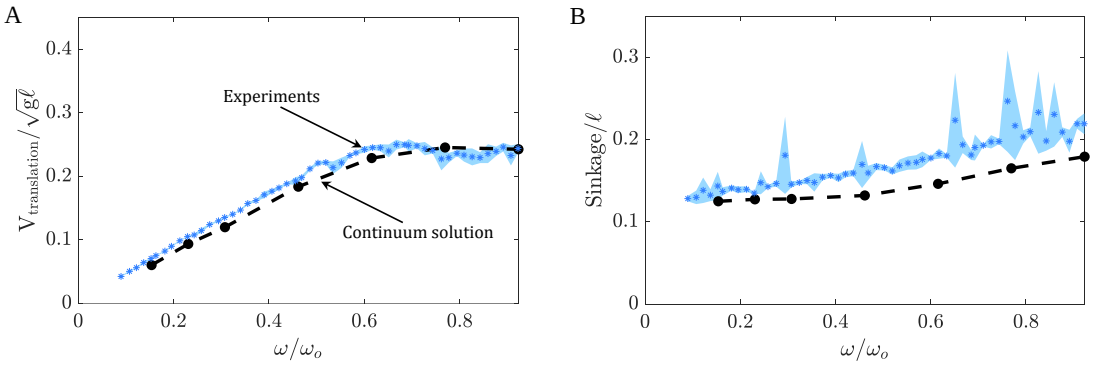

Figure 4-4: **Comparison of wheel locomotion experiments and continuum simulations:** Variation of *(A)* translation velocity, and *(B)* sinkage from experiments (blue), and continuum modeling solutions (black). The results are non-dimensionalized using a characteristic system velocity $(g\ell)^{0.5}$ (= 1440 mm/s) for translation velocity; a characteristic system length ℓ (= 212 mm) for sinkage; and a characteristic angular velocity, ω_o (= $(g/\ell)^{0.5}$ = 65 RPM) for angular velocity, where g represents the gravity and ℓ represents the wheel's outer diameter.

The trends of steady-state translation velocity and sinkage with varying ω obtained using continuum modeling are plotted in Figure 4-4A and B. Continuum modeling successfully captures the experimental trends for wheel locomotion; in particular, the model captures the plateau in the normalized $v - \omega$ curve at the correct rotation speed and correctly predicts increased sinkage with rotation rate.
To check the robustness of the results, we also applied small changes to the initial state of the experimental and simulated systems — including minor variations in ini-

tial wheel depth, initial wheel velocity, and ramp-rate of the wheel — and observed that the steady-state results in both systems were insensitive to these variations. [88].

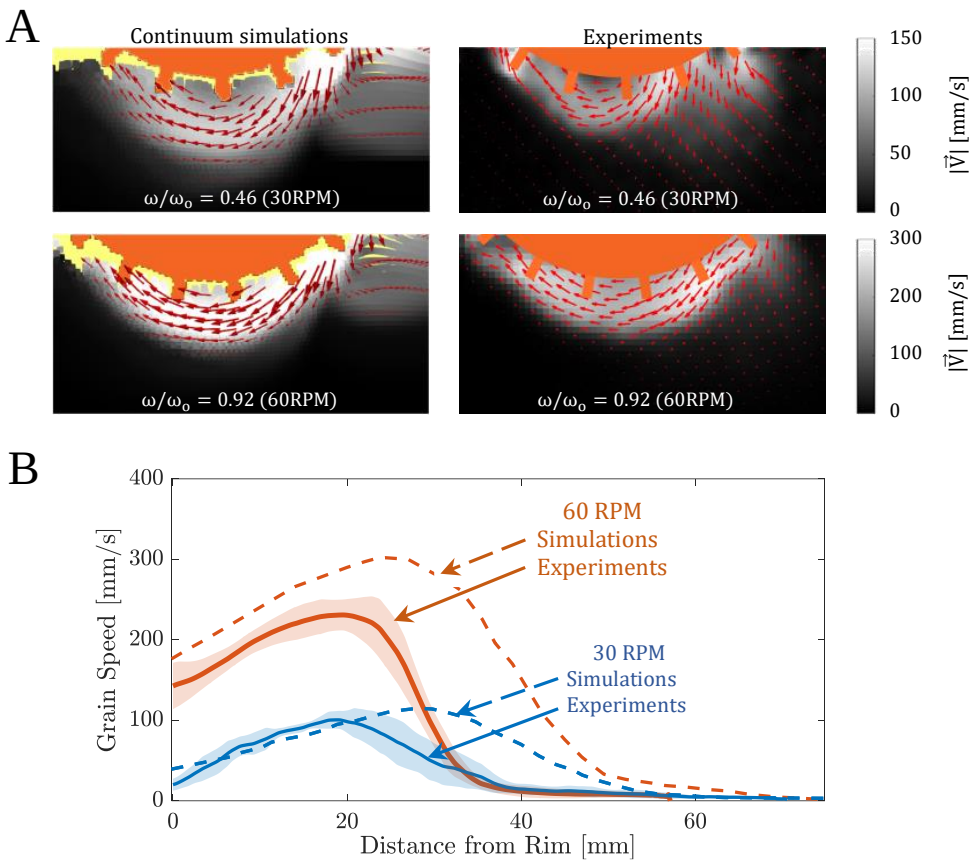

Figure 4-5: **Comparison of wheel locomotion experiments and continuum simulations:** *(A)* Granular flow field velocities obtained from continuum modeling and experiments (PIV) for slow (30 RPM, top) and fast (60 RPM, bottom) wheel locomotion. Data are averaged over an effective rotation of 0.1 rad (for PIV), with the orange regions representing the mean position of the wheel. See Movie S4, S5, and S6 for more details. *(B)* Plots showing variation of grain velocity from continuum simulations and PIV experiments along the radial direction directly below the center of the wheel; note some wall friction from the plexiglass plate exists in the experiment but not in the continuum solution. Key structural features of the flow under the wheel agree between the experiments and model in *(A)* and *(B)*

To further validate the model predictions, we have conducted experiments to visualize subsurface flow fields as discussed in section 4.2 and compared them to the

model. Velocity fields in grains for 30 and 60 RPM cases from continuum modeling and experimental PIV analysis are plotted in Figure 4-5A and B. There is some wall drag from the plexiglass plate that likely causes the granular flows in the experiment to be overall slower than the model, however, the key structural features of the flow under the wheel agree between the experiments and model. Importantly, both show a zone of material ahead of the wheel being pushed forward and a wide zone under and behind the wheel being pushed to the rear. The rear flow zone also grows with increasing ω due to higher flow entrainment and material movement at higher ω.

4.4 Towards reduced-order models: High-speed RFTs

A major benefit in identifying an accurate continuum model for a system is the possibility of using it to extract global-scale simplifications of the system's dynamics that can be used to develop further-reduced models. For example, in previous work on slow quasistatic intrusion, Askari et al. [146] found a connection between frictional yielding and a reduced-order intrusion force model called granular Resistive Force Theory (RFT) [93]. The success of the present continuum model for slow and rapid locomotion in wheels (and the other intrusion scenarios in this study) motivates us to ask whether an RFT-like reduced-order model for complex and rapid intrusions exists and if it might be derivable based on phenomena observed within the continuum model. We begin by first defining the quasistatic form of RFT and evaluating its predictions for wheeled locomotion dynamics. From Chapter 3, 2D-RFT intrusion force formula can be re-written as:

$$\mathbf{F} = \int_S \boldsymbol{\alpha}(\beta, \gamma)\, H(-z)|z|\, \mathrm{dA}. \tag{4.1}$$

where, RFT presumes the force-per-area vector (or traction) $\mathbf{t}$, on each surface element can be written as $\mathbf{t} = \boldsymbol{\alpha}(\beta, \gamma)\, H(-z)|z|$, dependent on the element's orientation angle (β), velocity angle (γ), and vertical depth from the free surface ($|z|$), with H being the Heaviside function. We often use the phrase 'quasistatic RFT' to refer to the original version of 2D-RFT proposed by Li et al.[93] from here on, in this chapter. We do this to avoid any potential confusion between 'Dynamic RFT' proposed by us and quasistatic 2D-RFT of theirs.

Figure 4-6A and B show the results of applying quasistatic RFT (solid blue line in Figure 4-6A and B) in modeling grousered wheel locomotion using the established RFT functions α_x and α_z [93]. Figure 4-6B shows that while RFT captures the speed vs ω trends at low ω, at higher ω it does not predict the wheel locomotion kinematics. RFT predicts a linear relation between the angular and translation velocities, which matches the experiments' dynamics at low-speeds, but diverges as ω increases. The fact that quasistatic RFT predicts the steady speed of a round wheel to always be

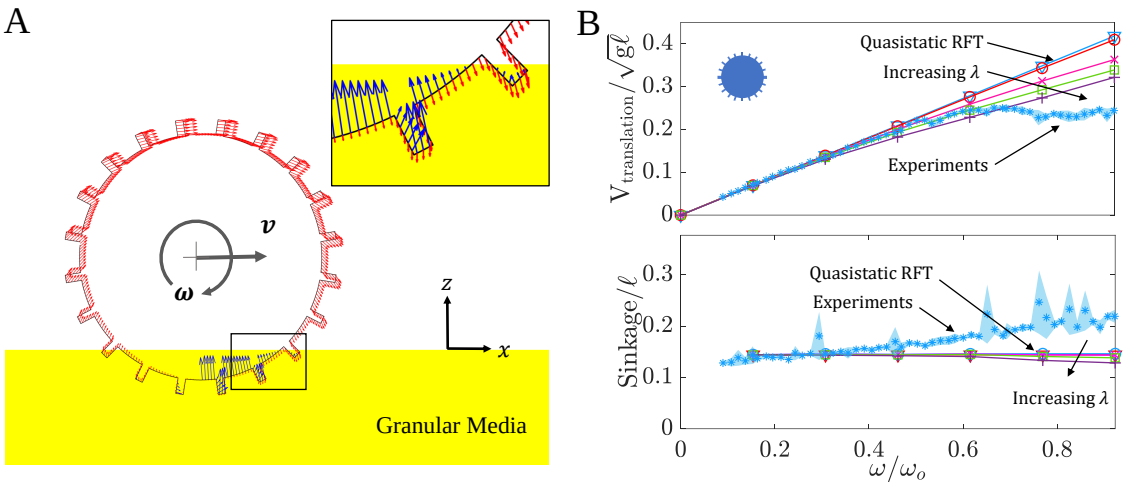

Figure 4-6: **Experiments vs RFT:** *(A)* Snapshot of a quasistatic RFT simulation, used for studying grousered wheel locomotion. Direction and magnitude (normalized) of the velocity and resistive stress are indicated by red and blue arrows, respectively, along surface elements of the wheel boundary. *(B)* Translational velocity (Top) and sinkage behaviors (Bottom) of the wheel; experimental mean and 1σ standard deviation (light blue data) and RFT results with local $\lambda\rho v^2$ modification (solid lines). The results in *(B)* are non-dimensionalized as explained in figure 4-4. The direction of increasing λ is indicated (λ=0, 1, 25, 50, 100). Red solid lines with $\lambda = 0$ (in B) correspond to quasistatic RFT results.

a constant multiple of the wheel spin can be shown as a consequence of the rate-independence of the RFT traction relation in equation 4.1 (see Appendix B.2 at the end of this chapter for more details).

4.5 Exploiting the continuum treatment for physical insight

An important step in developing a general reduced-order model for high-speed granular intrusion scenarios is to identify the key underlying physics. In granular intrusions, rate effects could arise due to a variety of physical causes. Increased vibrations in the media could fluidize the material at high speeds and reduce its strength [159]. Increasing velocities could decrease the friction on the wheel/media interface (per a dynamic friction drop), which in turn could decrease the traction on the wheels. Rapid flows may also have significant *micro-inertia*, which makes the rheology rate-dependent by causing the stress ratio $\mu \equiv \tau/P$ to depend on shear-rate through the "inertial number" I, where $I = \dot{\gamma}\sqrt{d^2\rho_s/P}$, where $\dot{\gamma}$ is the shear-rate, d the mean

grain diameter, ρ_s the solid particle density, and P the local pressure [53, 54]. Moreover, conventional *macro-inertia* (i.e. the $\rho\dot{v}_i$ term in the momentum balance) adds inertial body forces that could alter the flow of the media and its resistance against the intruder.

Predicting the dominating rate effect(s) is difficult using experiments alone. In this regard, our continuum modeling approach greatly aids in eliminating non-significant candidates from the possible rate effects above. The key is to recall that our model implements a *rate-insensitive frictional surface interaction* with no dynamic friction drop on the wheel-sand interface, and a *rate-insensitive constitutive model* with no dependence on the inertial number nor any accounting of material thermalization or fluidization. The model does, however, include macro-inertia in the momentum balance equations. The fact that the continuum model is successful in capturing the wheel dynamics along with many other granular intrusion scenarios (discussed later), indicates that the observed rate effects can be reconciled solely from macro-inertia ($\rho\dot{v}_i$). At the same time, the *global* consequences of *local* macro-inertial forces may be subtle and depend upon the particular system and its dynamics.

Based on this insight, along with analysis of the continuum solutions to wheel locomotion and other granular intrusion scenarios from the literature, we now propose and test a more general RFT that encompasses the domain of slow to rapid intrusions in granular media, which we refer to as 'Dynamic RFT' (DRFT).

4.6 Dynamic RFT (DRFT)

DRFT modifies the quasistatic RFT in two ways to account for macro-inertial effects. First, we add a momentum flux contribution, which we term the *dynamic inertial correction*. This term is required for the transfer of momentum to the granular material surrounding the intruder. This term is also in accord with many previous studies on high-speed granular intrusions [128, 160, 161, 162, 163, 133, 130, 164], and takes the form of an additional rate-dependent force going as velocity-squared. The second modification, which we will show is critical for more complex intrusions, describes the way in which increased bulk inertia can change the free-surface geometry. A change to the free-surface geometry then feeds back on the resistive forces through the depth-dependence of RFT. We denote this modification as the *dynamic structural correction*. Taken together, DRFT imposes the following formula for the traction on a surface element:

$$\mathbf{t} = \boldsymbol{\alpha}(\beta, \gamma) H(-\tilde{z}) |\tilde{z}| - \hat{\boldsymbol{n}} \lambda \rho v_n^2 \tag{4.2}$$

where $|\tilde{z}|$ indicates the *effective depth* of the surface element. That is, $\tilde{z} = z + \delta h$ where δh represents the height decrease of the free surface in the zone affecting the

traction at (x, z). Recall $\hat{\boldsymbol{n}}$ represents the outward normal to the surface element (and $-\hat{\boldsymbol{n}}$ the inward), and we define v_n as the normal component of the surface velocity. To use DRFT, one must determine the appropriate δh for each surface element of the intruder as a function of the intruder motion as well as an appropriate λ, an $O(1)$ scalar fitting constant. Similar to RFT, DRFT asserts a *localized* formula for the calculation of stresses on intruder sub-surfaces, and thus allows for near real-time modeling of intruder motion.

Implementing DRFT

The procedure for modeling intrusions with DRFT begins by discretizing the intruding geometry into subsurfaces of size $\Delta\ell$, and defining the system properties such as intruder weight, gravity, the effective media density ρ, and RFT scaling coefficient ξ from calibration. One can then identify the leading edges of the intruder, and use an external measurement to determine λ and the effective free surface variation δh. Scaled continuum simulations, DEM, or experiments (PIV) can be used to measure λ and the behavior of δh; we provide an example of a methodology to infer δh using *scaling* analysis at the end of this chapter (Appendix B.1). Equation 4.2 can then be used to calculate the granular resistive force on the leading edges. With intrusion force fully defined by DRFT, one can iteratively apply a momentum balance in different directions on the intruder geometry to model the intruder motion. Thus, except a macro-inertial additive part and change in free surface heights, the remaining aspects of RFT implementation remain the same as described in section 3.2 of the chapter 3

4.6.1 Understanding the dynamic inertial correction

We take a moment to discuss the two dynamic corrections included in DRFT, beginning with the dynamic inertial correction. Analysis of the momentum balance equations under certain simplifying circumstances (see Appendix B.1 of the Supplementary Information at the end of this chapter) allows one to deduce that the transition from a quasistatic flow to a faster flow comes with a resistive force increase that goes as $\rho A v_n^2$, similar to dynamic pressure in a fluid, where A is the intruder area. Physically, this term represents the reaction force that comes from transferring momentum to the granular media. A number of previous studies [128, 160, 161, 162, 163, 133, 130] have modeled the rate-dependence of intrusion force similarly, by adding a term proportional to normal speed squared to a depth-dependent 'static' term. Examination of experimental data in [161, 165], agrees with a rate-dependent force addition of the form $\lambda\rho A v_n^2$ in simple vertical and horizontal intrusions (see Figure S2 and S3, and Movie S1 and S2 of the Supplementary Information at the end of this chapter), where λ is a $O(1)$ scalar fitting constant that accounts for certain approximations in the analysis (see Supplementary Information Appendix B.1 at the end of this chapter).

It is natural to ask whether the addition of a velocity-squared term to the quasistatic RFT relation is enough alone to explain the rate-dependence observed in general intrusion scenarios, including wheeled locomotion. We suppose the surface traction is modeled to obey the relation in equation 4.3 below, and use this relation to re-evaluate the grousered wheeled locomotion problem:

$$\mathbf{t} = \boldsymbol{\alpha}(\beta, \gamma) H(-z)|z| - \hat{\boldsymbol{n}} \lambda \rho v_n^2 \tag{4.3}$$

Figure 4-6B shows the results for various values of λ. The case of $\lambda = 0$ represents the previously discussed quasistatic RFT in these graphs. The introduction of the inertial force term ($\lambda > 0$) adds a new force contribution having net force components upward and opposite to the horizontal direction of wheel translation. This upward force results in a decrease of wheel sinkage, opposite to the experimental observation. The magnitude of these extra forces is very small; the pre-factor λ was varied from 1 to 100 in an attempt to match the experiments, but this has little effect on the outcome, and the trends for both velocity and sinkage cannot be matched (Figure 4-6B). It is clear the dynamic inertial correction alone is not sufficient to describe this set of tests.

4.6.2 Understanding the dynamic structural correction

To understand the rationale behind the dynamic structural correction in DRFT, we start by considering the spatial variation of plastic strain-rate magnitudes from continuum modeling simulations for low and high ω cases shown in Figure 4-7D. The plots make it possible to visualize how different portions of the wheel derive their resistive forces from different zones of the granular media. While the strain-rate profiles change as angular velocities increase, the basic patterns of shearing remain similar. The sheared material reaches the free surface of the granular volume in two zones. Approximately half of the flow originating from the leading edge of the wheel reaches the free surface on the trailing rear face of the wheel. The remaining flowlines extend to the free surface on the leading front face of the wheel. Importantly, the height of the free-surface on the rear side of the wheel decreases with increasing ω; qualitatively, as ω grows, the wheel expels material on the rear side. The reduction in rear free surface height suggests a reduction in the pressure head and consequent weakening of the material in the rear shear zone. This is a key observation that motivates the form of the dynamic structural correction.

Figure 4-7C shows the free surface height reduction, δh, as measured from the continuum model simulations by identifying the lowest point making rear contact with the wheel for which hydrostatic-pressure $\rightarrow 0$. Indeed, the faster the wheel spins, the deeper this point descends. Given the paucity of parameters in the continuum model, dimensional analysis is useful; for a given substrate material, it suggests

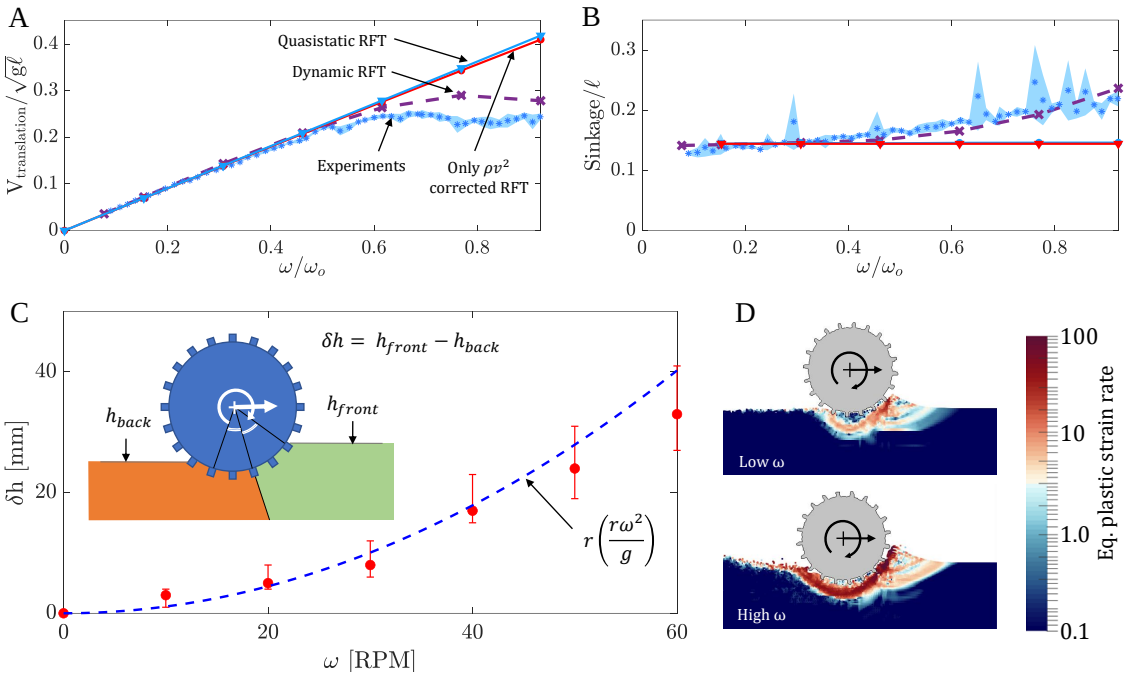

Figure 4-7: **Dynamic RFT:** Variation of *(A)* wheel translation velocity and *(B)* sinkage from experiments compared to quasistatic RFT, DRFT, and DRFT without any dynamic structural correction (i.e. having only the $\sim \rho v^2$ correction). *(C)* Presumed zones of influence and effective free-surface variation for constructing the dynamic structural correction; δh represents the gap between effective front and back free surface positions. MPM data (red circles) and empirical fit (blue dotted line) for δh. *(D)* Variation of equivalent plastic strain-rate magnitude obtained using MPM continuum modeling for slow (30 RPM) and high speed (90 RPM) wheel locomotion. See Movie S7 in the Supplementary Information at the end of this chapter for visualising the variation over time. The results in *(A)* and *(B)* are non-dimensionalized as explained in Figure 4-4.

the form $\delta h = r \cdot \psi(r\omega^2/g)$ for some function ψ. Surprisingly, we find that ψ is well-approximated by the identity function. The fit of $\delta h = r\,(r\omega^2/g)$ and the continuum modeling results in Figure 4-7C show good agreement. Combined with the understanding developed in the previous section, the form of the effective free surface is approximated using a simple partition as shown in Figure 4-7C, with the rear zone of the wheel set to have a constant free-surface height reduction h_{back} differing from the initial free-surface height (undisturbed medium height) by a term $\delta h = r\,(r\omega^2/g)$. To select the dividing angle delineating the front- and rear-affected zones of flow, we choose to equally divide the contact zone for driven wheels. Our choice is driven by the simplicity of this division, also observing a similar division of contact zones for

representing traction on wheels by Hambleton et al. [166]. This new model changes the effective free-surface heights only for the surface elements closer to the rear part of the intruding wheel surface.

By including this effective free-surface height formulation, we now arrive at DRFT, equation 4.2. We implement this DRFT model using the same implicit RFT code framework similar to that discussed earlier in section 3.2. The only diffrerence being a slight modification in calculation of RFT force to calculation of forces in accordance with eq 4.2 using $\lambda = 1$ and $\rho \approx \rho_c = 638$ kg/m^3. The effective heights of wheel grousers were also taken to be one-third of their true physical length (based on experimental PIV data) to account for the shadowing effect [156]. Convergence studies of the force response determined the discretization fineness of the wheel shape. Each inner-circumferential subsurface lug was divided into 14 elements, and each of the lug surfaces (1 normal and two side-wise) was divided into eight elements. Thus, the wheel had 570 surface elements in total. For the Dynamic RFT implementation, only the effective heights experienced by surface elements on the rear side of the wheel were modified. This height modification was based on the formulation shown in figure 4-7(C). The rear region was taken as the region of the rear half of the contact area between sand and wheel (see figure 4-7(D)). The division was based on the angle subtended by the contact region at the wheel center.

The trends of translation velocity and sinkage with respect to ω now show good agreement between experiment and DRFT (Figure 4-7 A and B). We also include, for comparison, what the solution is when only the dynamic inertial correction is used. While DRFT combines both dynamic corrections, it is clear that the dynamic structural correction dominates the dynamic inertial correction in the case of wheeled locomotion. While we have presumed for simplicity that the division between the two contact zones takes place halfway through the wheel-sand interface, it can be seen in Figure 4-5A and 4-7D that the division may actually be closer to the front of the wheel. This could explain our slight overprediction of speed for high ω (Figure 4-7A). A second set of grousered wheels tests involving a smaller wheel are included in the Supplementary Material at the end of this chapter (see Figure S1 and Section S3) and DRFT works equally well without the need to refit the function for ψ used for δh.

The agreement with DRFT suggests that the low-to-high slip transition in wheeled locomotion (where slip$= 1 - v/r\omega$ for v is the translational velocity, r is the nominal radius, and ω is the angular velocity of the wheel) occurs largely because faster spinning wheels remove material from behind the wheel, which reduces the pressure in the rear zone, thereby weakening the base of material that would otherwise provide a scaffold off of which the wheel pushes. Updating RFT by accounting for this effect has appropriately captured the dynamics of the complex wheel locomotion scenario in a reduced-order modeling framework.

4.7 Additional verification studies

The wheel tests provide a complex intrusion scenario and have a dynamic structural correction that is much larger than the inertial correction. To check the robustness of our continuum modeling approach as well as Eq 4.2 for DRFT, we now examine the converse situation with two additional sets of simulations — submerged plate intruders and locomoting runners. We choose these cases based on data from continuum solutions, validations against the literature, and the arguments of the previous section, and expect the dynamic structural correction to be small and the dynamic inertial correction to dominate. Visually, these cases represent two separate classes of intruders. While the dragged plates represent forced motion, the runners represent a class of self-propelling locomotors that may appear similar to the prior studied wheels. Yet, force responses in both cases are dominated by the dynamic inertial correction (more details in the following sections) and do not mimic the behavior of the grousered wheel. Thus, these distinct cases test the breadth of the modeling capability of DRFT.

***Submerged horizontal intrusion*:** Thin plates submerged in granular media at various fixed depths (20-40 mm) are dragged horizontally at different speeds using continuum modeling. The continuum model runs in plane strain, where the plate has a length of 0.016 m and the effective medium density is 900 kg/m^2. The chosen density is similar to that of ground coal or marble. The filled circles in Figure 4-8A show the observed drag force variations with the drag speed. Experimental studies by Schiebel et al. [165] found the variation of drag forces in such a scenario to follow the trend $K|z| + \lambda\rho A v^2$ (see Figure S1 of Supplementary Information at the end of this chapter), where K and λ are constants, $|z|$ is the depth of the plate below the free surface, ρ is the effective granular density, A is plate area, and v is horizontal plate velocity. Our continuum modeling also obtains the same trend (Figure 4-8A). In the slowest cases ($v \sim 0$), we obtain a linear force versus depth relation, $F_{\text{drag}} = K|z|$ for $K = 580$ N/m. As speed increases, we find that continuum predictions match the data well at three different depths, for $\lambda = 1.1$. Incidentally, the same value of λ also matches the rate dependence observed in the Schiebel et al. [165] experiments for horizontally driven intruders at the free surface.

A comprehensive understanding of the resultant form of the drag force trends can be obtained by observing continuum modeling results in the context of DRFT. Figure 4-8B shows the deformation profiles around the plate at two selected speeds (which differ by about an order of magnitude). The profiles in Figure 4-8B of high and low-speed intrusion suggest that the intruder tractions arise from pressing the granular material in front of the plate upward and to the right, toward a common free surface height, h_{front}. The rear flow zone, which changes in slow versus high-speed intrusion, is either in the separated phase or newly consolidated as it falls and fills

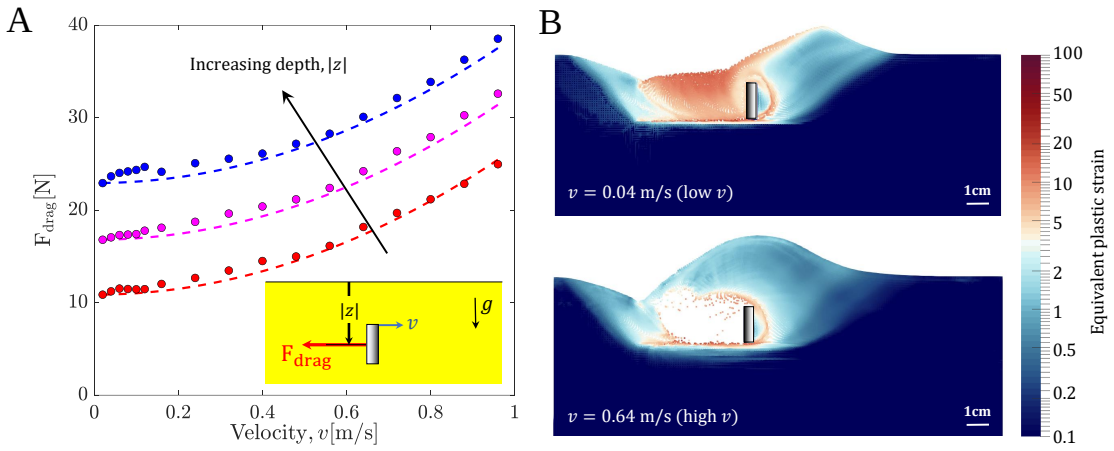

Figure 4-8: **Modeling slow-to-rapid plate intrusion:** *(A)* Continuum MPM data (colored circles) and $K|z| + \lambda\rho A v^2$ fits (dotted lines) for horizontal intrusions at various depths ($|z|$) ([20,30,40] mm), where $K = 580$ N/m and $\lambda = 1.1$. Variation of equivalent plastic strain rate for *(B, top)* low Velocity (0.04 m/s) and *(B, bottom)* high velocity (0.64 m/s) intrusion cases (at 30 mm depth). See Movie S2 in the Supplementary Information at the end of this chapter for the video. Simulations are plane-strain.

in the gap behind the moving plate. Likewise, the rear media makes a negligible contribution to the resistive plate force; no part of the rear face of the plate is a 'leading edge' satisfying $\hat{\boldsymbol{n}} \cdot \boldsymbol{v} > 0$, so forces approximately vanish there. This is in contrast to the grousered wheel case, where, due to rotation, a significant portion of the back half of the wheel is a leading-edge that can interact non-trivially with media behind the wheel. We thus expect a negligible dynamic structural correction for horizontal plate drag, due to the lack of leading-edge on the rear face of the plate and an approximately speed-independent h_{front}. Indeed, the obtained force relation $F_{\text{drag}} = K|z| + \lambda\rho A v^2$, which we obtained from experiments as well as continuum modeling, displays only the dynamic inertial correction of DRFT as expected. These results concur with our hypothesis and confirm the DRFT prediction for submerged sideways intrusion. For similar reasons as just discussed, we expect symmetric vertical intrusion of plates to also invoke a negligible structural correction; see Supplementary Information (Figure S3) at the end of this chapter for details and confirmation against DRFT. Note that in our plate drag studies, we have restricted our intrusion depths to within an $O(1)$ factor of the plate width. This depth range indicates the approximate limits of RFT, as beyond such depths, the assumptions of RFT (such as a linear dependence of granular resistance with depth) begin to degrade [119].

Four-flap runner: While the dragged plates are forced to move at set speeds, we also study a self-propelling locomotor, a four-flap runner, whose locomotion speed is determined via the interactions of the locomotor's self actuated limbs (flap motion) and the substrate dynamics (geometric details are in Table 4.3). The low number of flaps, along with the large flap length to inner radius ratio minimizes the interaction between neighboring flap intrusions of the runner's resultant granular flow.

Table 4.3: Four-flap wheel dimensions

1. Inner Diameter, D	50 mm
2. Wheel width, W	1 m
3. Flap length, h_{flap}	70 mm
4. Flap width, w_{flap}	14 mm
5. Gravity, g	9.8 kg/m^2
6. Mass of wheel, m	10.5 kg

The runner takes inspiration from the experiments of Li et al. [93] and Zhang et al. [167] with running C-legged robots (similar to Fig 4-1C). Li et al. [93] drove their robots with dimensionless spin ratios (ω/ω_o) ranging over $0-1.25$ $\big((\omega_{max}, \omega_o) = (240, 190)$ RPM$\big)$ and observed a decreasing slip with increasing angular velocity in their experiments. Similarly, Zhang et al. [167] tested locomotion over a larger ω/ω_o range of $0-3.8$ $\big((\omega_{max}, \omega_o) = (720, 190)$ RPM$\big)$ and observed that in the higher range of spins, the sinkage in their experiments breaks away from trends observed by Li et al[93], i.e. robots elevating above their resting depth. Their running robots display qualitatively opposite behaviors to grousered wheels: as spin increases, runners sink less and move faster whereas wheels sink more and travel slower. We explore if the fundamental physics of such qualitatively reversed behavior is already embedded in our continuum modeling and consequent DRFT framework. Our current continuum modeling capabilities being limited to plane-strain (2D) problems, we cannot implement a full C-legged robot running in 3D. We take the four-flap runner as a representative of the family of runners, which show a decrease in effective-slip and sinkage with increasing angular rotation rates, and explore our 2D continuum model's capability in modeling such behaviors.

In the continuum modeling, the dimensionless mass ratio of the runner, given by $m/\rho_c \ell^2 W$ for W the out-of-plane width, is set to be in the same range ($\approx$6) as the corresponding twenty-grousered wheels shown previously to keep the comparison between runners and grousered wheels relevant. For similar reasons, we keep the runner diameter similar to that of grousered wheel (190 mm vs 212 mm). The angular velocity of the runner is varied over a range of 10 RPM to 300 RPM which corresponds to a dimensionless spin ratio range varying from $\omega/\omega_o = 0-4.5$ ($\omega_o = 65$

RPM). The continuum results (see Figure 4-9B and C) show qualitative agreement with the findings of Li et al. [93] and Zhang et al. [167] — with increasing spin rate, a decrease in effective slip and an elevation of the wheel above the rest depth is observed. Incidentally, the turnover in elevation for our runners was found at a spin ratio ~ 1.4, similar to that obtained by Zhang et al. [167].

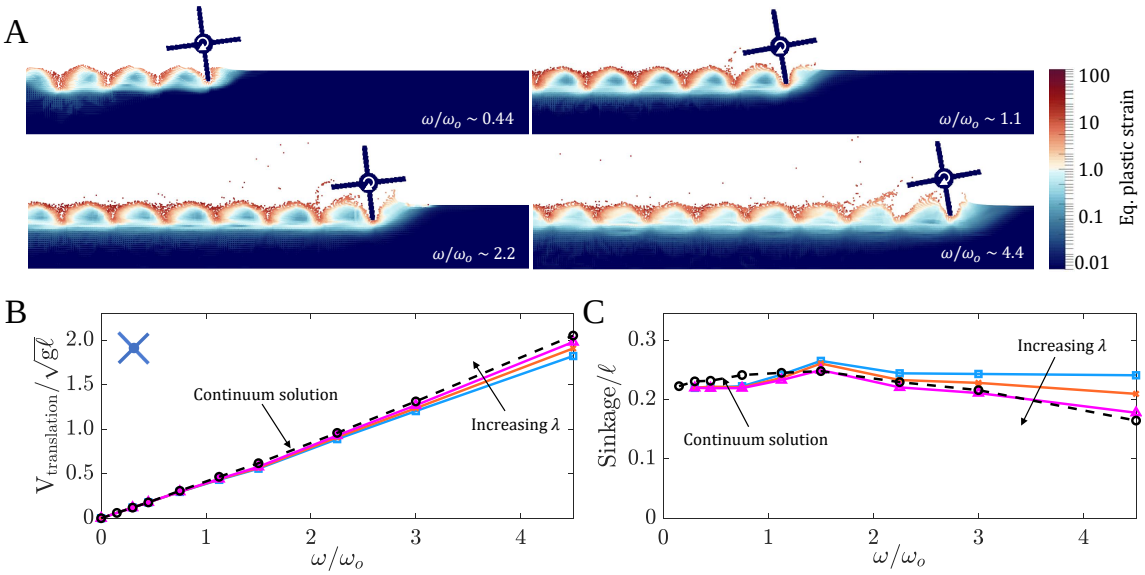

Figure 4-9: **Running on granular media:** *(A)* Variation of equivalent plastic strain at increasing angular velocities ω for four-flap runner locomotion ($\omega_o = 65$ RPM). See Movie S8 in the Supplementary Information at the end of this chapter. Continuum solutions from MPM (black dotted line with 'o' markers) and DRFT solutions (solid lines) for translational velocity *(B)* and sinkage *(C)* versus angular velocity, ω, in four-flap runner locomotion. DRFT solutions for $\lambda = 0, 2, 4$ pictured. The results in *(B)* and *(C)* are non-dimensionalized as explained in figure 4-4 with $\ell = 190$ mm (runner's outer-diameter).

We now use the continuum model as a baseline reference to evaluate the DRFT performance for runners. Figure 4-9A shows the variation of the equivalent plastic strain for four different angular velocities in the continuum model. As expected, due to the relatively large separation between intruding legs, there is no visible self-interaction of the granular material between intrusions, and the free surface height directly behind intruding legs remains unchanged, which suggests a minimal role of the dynamic structural correction. This observation guides us to model these scenarios using DRFT with typical, $O(1)$, λ values ($\lambda = 0, 2, 4$) and *no* dynamic structural correction. Figure 4-9B and C show the resulting steady-state sinkage and translation velocity at various angular velocities from DRFT calculations (solid

lines). It seems that DRFT captures the kinematic trends of the reference solution, approaching quantitative accuracy for $\lambda \sim 4$. With this result, it is encouraging to note that DRFT has captured the dependence on ω in both runners and grousered wheels, which behave in opposite ways as ω increases.

Our four-flap runner study also explains the observations of the above-mentioned C-legged robot studies. We believe the quasistatic RFT modeling in Li et al. [93] was sufficient because the dynamic inertial correction was still small in their tested range (in our study, the dynamic inertial correction becomes noticeable only above a ω-ratio of ~ 1.2). Zhang et al. [167] go to higher spins, revealing the non-trivial elevation and slip trends due to the rate that we see in continuum and DRFT solutions.

4.8 Conclusion

The success of NDPM based continuum approach in modeling granular intrusion up to high speeds in this work has led to two surprising conclusions for us—

First, a continuum model based only on a constant friction coefficient and tension-free separation is able to model complex granular intrusions well in a variety of scenarios. Note that though we use this model for modeling two intrusions scenarios in Chapter 2— (1) submerged cylinder intrusions and (2) two plates (multi-body) intrusions, both these cases corresponded to quasi-static intrusions. Thus the scenarios explored in this chapter indicate a different aspect (velocity sensitivity) of the model than what was explored in chapter 2. Second, we find that just two macro-inertial corrections to RFT allow successful modeling of granular intrusions across speed regimes can be easily incorporated in 2D-RFT form to develop a dynamic RFT.

These results were obtained progressively. By analyzing the simple continuum model's solutions, an understanding of the key physics involved in such complex intrusion scenarios was identified, which in turn motivated the ingredients of the dynamic resistive force theory (DRFT). DRFT allows for robust, near real-time modeling of granular intrusion in a large variety of cases, including self-propulsion. Our study of rigid intrusion into granular media indicates that the force response upon intrusion consists of two primary rate-dependent modifications: (1) a dynamic inertial correction and (2) a dynamic structural correction. The dynamic inertial correction accounts for the momentum transfer to the surrounding material, whereas the dynamic structural correction describes how a rapidly moving intruder can change the pressure head by modifying the free surface. Both effects are related to the macro-inertia of the media. For the scenarios considered here, micro-inertial effects (per a $\mu(I)$ rheology) are not significant even if the motion appears 'fast' — previous work on rapid projectile penetration [109] indicates that the high pressures that develop around rapid intruders

keep I relatively small. Hence, the observed rate-dependent dynamics arise under rate-independent rheology, as we have used, since macro-inertia (stemming from $\rho \dot{v}_i$ in the momentum PDE) alone brings about the observed rate effects. In terms of limitations, it is known that quasistatic RFT loses accuracy when intruders are too deep, as the linear force versus depth dependence eventually plateaus in the lift direction [119] for slow intruders. We expect the same constraints on depth to apply to DRFT as well.

Dynamic RFT has enough generality to explain two opposing scenarios: weakening of the media during grousered wheel locomotion, as well as strengthening of the media during rapid running. We have shown that DRFT accurately predicts the system behaviors in the limiting cases, i.e. when one of the two dynamic effects is dominant. Further studies will be required to fully test the model for mixed cases where both dynamic corrections are significant. We have assumed additivity, in line with previous notions of a 'static' component and an inertial component of the intrusion force [94, 161, 128, 165]. However, it is possible a more complicated functional combination may arise.

Although this study mainly focused on dry non-cohesive granular media, the formulation of DRFT in granular flows suggests the existence of other similar reduced-order models in other materials. A combination of experiments and continuum modeling proved vital in this study for verifying the underlying physics. The proposed continuum framework can easily be modified to cater to a large variety of materials once their constitutive equations are known. Future work may explore faster methods of predicting flows, along with various complex intruders, to systematically determine the form of the dynamic structural correction. Further studies could also explore the existence of similar reduced-order models for related classes of materials like non-critical state granular media, cohesive sands/muds, and fluid-saturated sands.

In the next chapter, we take inspiration from the outcomes of this study and explore the next logical step in expanding the limits of RFT. i.e. exploring the existence and the form of RFT in three dimensions.

Chapter 5

Extending resistive force theory to three dimensions: 3D-RFT

5.1 Introduction

As we discussed in earlier chapters, real-time modeling of granular intrusions is critical for various real-life applications such as path planning and efficient maneuvering in extra-terrestrial and off-terrain rover locomotions. Additionally, such capabilities enable developing a heuristic understanding and quick insight into a variety of phenomenons like circum-mutation [168] and robotics [169]. While the full-field numerical modeling approaches are computationally expensive, low and high-speed RFTs discussed in chapters 3 and 4 have limited use in real-life three-dimensional scenarios. Thus, this chapter explores the existence of an RFT in three-dimensions and proposes a three-dimensional version of RFT, 3D-RFT. We verify the 3D-RFT against a variety of granular intrusions scenarios, consisting of the arbitrary motion of many symmetric and unsymmetric shapes, and find an excellent match between the reference results and 3D-RFT predictions.

5.2 Form of a generic RFT

As discussed in earlier chapters, the success of fluid-RFT motivated many [91, 92, 93] to explore the existence of a similar theory in granular media. Li et al [93] proposed a plane strain (or 2-dimensional) version of RFT for granular media (2D-RFT) which we have used as the base for RFT related research in this thesis. In 2D-RFT, at low-speeds, the rate-independent nature of granular media (characterized by a low value of the non-dimensional *inertial number* I [53, 54, 94]) and low macro-inertia (ρv^2) makes the dependence of intrusion force independent of the velocity magnitude. See section 4.5 of Chapter 4 for more details on these topics in regards to quasi-static

RFT. Assuming local-pressure-dependent bulk strength and gravitational loading pressure results in Li's form for 2D RFT

$$\boldsymbol{F}_{\text{total}} = \int_{\text{surf}} \left((\alpha_x^{\text{mat}}(\beta,\gamma), \alpha_z^{\text{mat}}(\beta,\gamma)) \right) |z| \, ds \,. \tag{5.1}$$

Here, $\boldsymbol{F}_{\text{total}}$ represents the total force on a large surface, which is divided into smaller plane sub-surfaces of area ds and depth $|\boldsymbol{z}|$ from the free surface. The *tilt angle* β and *angle of attack* γ characterize the orientation and motion of each surface element of the intruding body (see Fig 5-1).

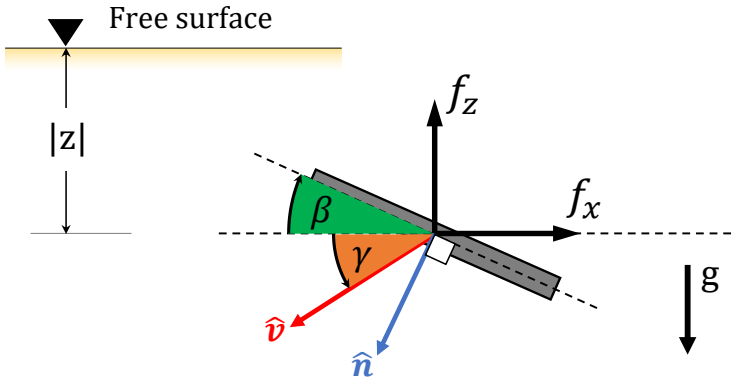

Figure 5-1: *2D RFT sub-surface characterization*: Any moving sub-surface is represented using a set of two characteristic angles — plate tilt angle (β, green) which represents the plate orientation (or normal direction, $\hat{\boldsymbol{n}}$), and velocity angle (γ, orange) which represents the velocity direction ($\hat{\boldsymbol{v}}$).

The vector-valued function of angles $\boldsymbol{\alpha}^{\text{mat}} = (\alpha_x^{\text{mat}}, \alpha_z^{\text{mat}})$ represents the force per unit area per unit depth; this function must be obtained a priori through experiments or simulations of plate drag and depends on the material properties of the granular media, the intruder surface interaction, and the value of gravity. Of note, Eq 5.1 assumes no cross-correlation between the forces on different sub-surfaces; only details local to a surface element determine the force on that element [91]. A comprehensive comparison of various existing reduced-order methods for modeling granular intrusions, including 2D-RFT and a *terramechanical* model, can be referred from Agarwal et al. [95].

Our primary aim is to extend RFT to a 3D theory by ultimately adding one new plate angle, ψ the *angle of twist*, and a third component of the force. Doing so involves consideration of a wide number of issues, outlined in Sec 5.4. To aid in the

endeavor, it helps to note that 2D RFT could be re-expressed as

$$\boldsymbol{F}_{\text{total}} = \int_{\text{surf}} \boldsymbol{\alpha}^{\text{mat}}(\hat{\boldsymbol{n}}, \hat{\boldsymbol{v}}, \boldsymbol{g})|\boldsymbol{z}|\, ds\,. \tag{5.2}$$

Here, the $\boldsymbol{\alpha}^{\text{mat}}$ function is expressed in terms of three vectors, the outward surface normal $\hat{\boldsymbol{n}}$, velocity direction $\hat{\boldsymbol{v}}$, and gravity $\boldsymbol{g}$. This more generic way of expressing 2D-RFT will motivate the form chosen for 3D-RFT.

In recent years, it has been shown that plasticity-based PDE models can also obtain the forms of 2D granular RFT [146]. More recently [108, 109, 17, 95, 16], the performance of the continuum approach in modeling a variety of granular intrusions has been demonstrated for wheeled locomotion, impact and penetration, and multi-body intrusion. Thus, while experimental observations primarily drove the original RFT discoveries, the availability of faster computational methods, the success of 2D RFTs, and a need for better real-time 3D granular intrusion methods have driven the exploration of 3D-RFT. Our work combines the capabilities of the continuum approach with a few symmetry requirements and DEM data to accurately and efficiently model the physics of 3-dimensional granular intrusion to develop a 3D-RFT form. We briefly discuss the details of the continuum approach next.

5.3 Theoretical motivator: Continuum modeling

We use the NDPM based continuum modeling discussed in chapter 2 as the primary theoretical motivator as well as the main reference data generation tool in this work. For implementing the model, we use the 3D numerical implementation of MPM developed by Baumgarten and Kamrin [13] for this study which has been successfully used for modeling complex problems in the past [13, 63]. The constitutive flow equations representing the material's separation behavior, shear yield condition, and tensorial co-directionality, respectively, are shown below:

$$\begin{aligned}
&(\rho - \rho_c)P = 0 \qquad \text{and} \quad P \geq 0 \quad \text{and} \quad \rho \leq \rho_c,\\
&\dot{\gamma}(\tau - \mu_{\text{int}}P) = 0 \quad \text{and} \quad \dot{\gamma} \geq 0 \quad \text{and} \quad \tau \leq \mu_{\text{int}}P,\\
&D_{ij}/\dot{\gamma} = \sigma'_{ij}/2\tau \quad \text{if} \quad \dot{\gamma} > 0 \quad \text{and} \quad P > 0
\end{aligned}$$

where, $i, j = 1, 2, 3$. In these equations, $\boldsymbol{\sigma}$ represents the Cauchy stress tensor and σ'_{ij} $(= \sigma_{ij} + P\delta_{ij})$ represents the deviatoric part of $\boldsymbol{\sigma}$ where $P(= -\sigma_{ii}/3)$ represents the hydrostatic pressure. $\tau(= \sqrt{\sigma'_{ij}\sigma'_{ij}/2})$ represents the equivalent shear stress on the system. μ_{int} and ρ_c represent the bulk friction coefficient and critical close-packed density of the granular volume. $D_{ij}(= (\partial_i v_j + \partial_j v_i)/2)$ represents the (plastic) flow

rate tensor, and $\dot{\gamma}(= \sqrt{2D_{ij}D_{ij}})$ represents the equivalent shear rate. We assume surface friction coefficient μ_{surf} describes the interaction of the granular continuum with intruder surfaces. ***We also highlight that in this chapter, we use μ_{int} as a substitute for μ_s, and μ_{surf} as a substitute for μ_f unlike Chapter 2. This change is meant only for a better understanding of the readers with no academic/theoretical reason(s).***

We verify the accuracy of this implementation against various **3D** in-plain out-of-plane motions to reliably use the data generated by this approach in determining a 3D-RFT. We test this in two scenarios:

In the first test case, we check if the 3D-continuum simulations can regenerate the experimental variation of force/depth/area on flat plates in submerged granular beds from Li et al.[93]. This experimental data was also used by Li et al.[93] in the generation of 2D-RFT form. We use an effective materials density of $\rho_c = 1450$ kg/m^3 (loose glass beads, $\rho_g = 2500$ kg/m^3, $\phi_c = 0.58$) inline with Li et al.[93] experiments and an approximate internal friction value for glass beads as $\mu_{\text{s}} = 0.4$. The media-plate surface friction was taken as $\mu_{\text{surf}} = 0.4$. The relative values of the forces from continuum results remarkably match the experimental observations. The absolute values from continuum results, however, are higher than experiments by a constant multiplicative factor of ~ 1.1. A smaller value of μ_{s} for glass beads could have provided a closer match to the experiments as the graphs are not expected to change their shape with changing internal friction values [93]. But we do not attempt the exact calibration as the purpose of the test was to verify the accuracy of the continuum formulation and implementation. These results establish sufficient efficacy of the continuum model for plate motions in which the velocity, plate normal, and gravity or co-planar.

In the second test case, we assess the quantitative accuracy of the continuum approach in modeling in-plane as well as out-of-plane forces. We consider a study Maladen et al.[170] which measured the normal and tangential forces on submerged plates moving horizontally in granular media as a function of plate twist (see Fig 5-3 (top) for angles definition). The material properties are provided in the figure caption. The continuum results match observations from Maladen et al.[170] well. The combination of the above two studies establishes the overall accuracy of the continuum model and its implementation for both in-plane and out-of-plane inputs and outputs in plate intrusion problems.

5.4 3D-RFT premises

We begin by systematically summarizing the physical assumptions and constraints we use to arrive at a generic 3D-RFT (the next section will provide further details

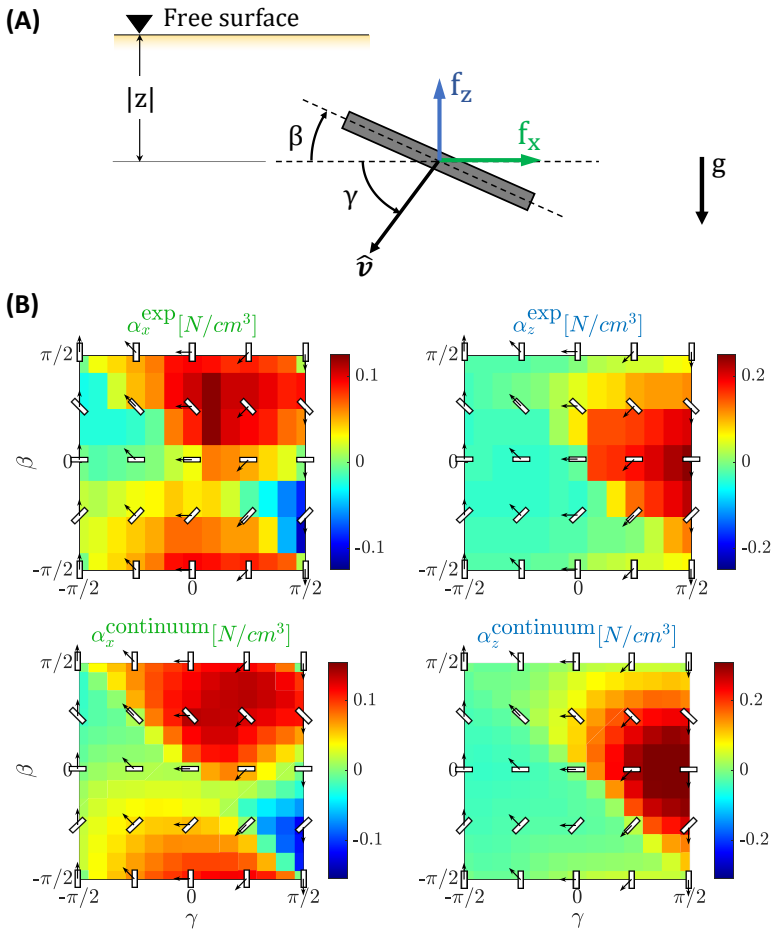

Figure 5-2: *Experiment vs Simulations — Qualitative match for in-plane plate motion*: *(A)*Schematic of plate orientation angle β and γ for in-plane motion study conducted using 3D simulation setup shown in figure 5-6. *(B)*Force/area/depth ($\boldsymbol{\alpha}$) from Li et al.[93] experiments (top) and continuum simulations(bottom). The plate configurations are also overlayed on graphs for clarity. The plates had no twist ($\psi = 0$) in regards to 3D-RFT definitions in these tests. Both the experiments and the simulations use glass beads with grain density (ρ_g) of 2500 kg/m^3 and a packign farction (ϕ_c) of 0.58. We use internal friction value, $\mu_s = 0.4$ and surface friction, $\mu_{surf} = 0.4$ for continuum simulations as reported by Li et al.[93]. The colorbar limits are slightly different between the experiments and the simulations because we do not attempt exact property calibration (μ_s and μ_{surf}) for this test case although we keep them in same the practically expected range.

on how these premises are used). These premises act as the guiding principles for establishing the form of 3D-RFT and are also useful for understanding the limits of

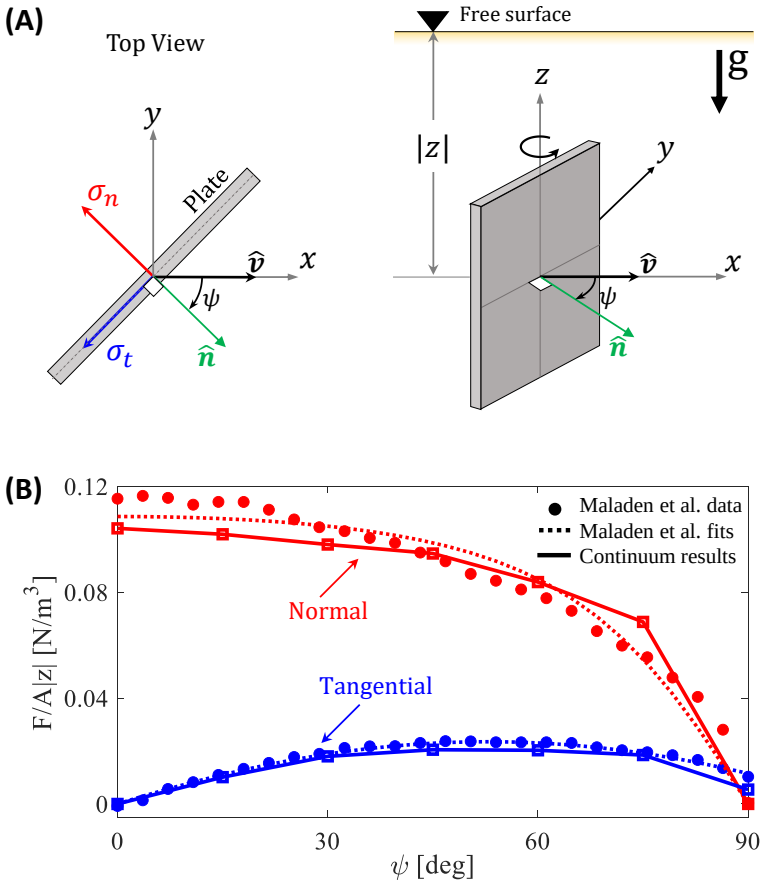

Figure 5-3: *Experiments vs Continuum modeling: Twisted plates*: (A) Schematic of plate orientations, and (B) variations of normal (red) and tangential (blue) forces from Maladen et al [170] experiments (• marker), their analytical fits to their results (dotted lines), and continuum simulations (■ marker with solid line). The forces are normalized by the plate center-depth ($|\boldsymbol{z}|$) and plate area. Experiments (loosely packed 3 mm glass particles) as well as simulation use glass beads ($\rho_g = 2500$ kg/m^3 and $\rho_c = 0.6$) as the granular media. Continuum simulations use $\mu_s = 0.4$ and $\mu_{surf} = 0.27$ in accordance with reported experimental data. The original Maladen et al. [170] results used a twist angle ($\beta_d = \pi/2 - \psi$) as the x-axis in their plots. We have modified the plots to have $\psi = \pi/2 - \beta_d$ on x-axis for simplifying the discussion.

3D-RFT.

1. *Premise-1:* ***Localization and de-coupling of forces*** This hypothesis assumes that the force on any sub-surface of an intruding body is independent of the motion experienced by any other sub-surface of the body. This is the

primary order-reduction hypothesis inherent to all RFT's, e.g. it is used in Eq 5.1.

2. *Premise-2:* ***Leading-edge hypothesis*** This hypothesis assumes that only the *leading edges* of a body (surfaces moving 'into' and not 'away from' a granular volume) experience resistive forces. Mathematically, such surfaces have a positive *dot product* $(\cdot)$ between their own surface normals and velocity directions $(\hat{\boldsymbol{v}} \cdot \hat{\boldsymbol{n}} \geq 0)$. The hypothesis applies only to non-cohesive media. Section C.5 in the Supporting Information provides evidence in support of this hypothesis in three dimensions.

3. *Premise-3:* ***Neglect of shadowed subsurfaces*** The 'no-shadowing' hypothesis assumes that forces vanish on parts of the surface that satisfy the leading-edge condition but lie in the immediate wake behind another part of the intruder [156]. Such surfaces are more pronounced in intruders with complex shapes or fine geometric features. A careful implementation (accounting for this effect) helps with this issue.

4. *Premise-4:* ***Validity of the continuum model*** We hypothesize that the medium is well-represented by the continuum model shown in Eq 2.3, which is used to guide the theory for 3D-RFT. This is akin to other advances in RFT stemming from this same basic continuum model [146, 16]. Consequently, the resistive force on a plate depends on the same limited set of material parameters that govern the continuum model: ρ_c (the critical density), μ_{int} (the internal friction), and μ_{surf} (the media-surface friction).

5. *Premise-5:* ***Force dependence on material internal friction*** We assume that normal forces on a plane surface only depend on the media's internal friction (μ_{int}). We use extensive data analysis to explore the dependence of resistive forces on μ_{int}. We observe that the normal forces maintain their relative values (with regards to $\hat{\boldsymbol{n}}$, $\hat{\boldsymbol{v}}$, $\hat{\boldsymbol{g}}$, and μ_{surf}) at a given μ_{int} for a large range of internal friction ($\mu_{\text{int}} = 0.3 - 0.9$) (see Fig C-1). Between different μ_{int}, the normal forces appear to only vary by a multiplicative factor ξ_n as discussed in Sec 5.5.

6. *Premise-6:* ***Force dependence on media-intruder surface friction*** We assume that normal forces on a plane surface weakly depend on μ_{surf} and tangential forces strongly depend on μ_{surf}. We use a similar analysis as done in the previous hypothesis to explore the dependence of surface tractions on μ_{surf}. We observe that the ratios between the magnitudes of tangential and normal stresses primarily depend on μ_{surf}. We also observe that plate-tangential resistive forces generated at a higher μ_{surf} could be used to generate the tangential

force for a lower μ_{surf}; the dependences at the lower surface friction can be obtained by limiting the magnitude of the tangential force based on the Coulomb friction limit at the lower μ_{surf}. Detailed material response graphs in this regard can be found in Sec C.3 of Supporting Information.

7. *Premise-7:* ***Isotropy of the drag force relation*** Any function providing the intrusion force on an intruder must obey a symmetry relationship whereby if the entire problem is rotated by some amount — that is the free-surface, gravity, intruder orientation/position, and intruder velocity are all rotated the same amount — then the resistive force must also rotate by this common global rotation. As we will show, this constraint, which implies the drag force relations are isotropic functions of their inputs, imposes a rather strong restriction on the three-dimensional form that 3D-RFT can take.

8. *Premise-8:* ***Consistency with lower-dimensional RFT*** We desire a 3D-RFT model that collapses back to the previously defined 2D-RFT description in the appropriate limits. Thus, in-line with the angle-based characterisation of 2D-RFT by Li et al.[93] (Fig 5-1), we desire to ultimately express 3D-RFT in terms of similar characteristic angles β and γ and a new twist angle ψ representing the angle between the planes of plate normal and velocity direction with the vertical.

In addition to the above premises, we will utilize a few operational constraints. We limit ourselves to quasi-static intruder motion, which assumes the absence of any inertial effects in the granular volumes. This was also assumed in the original 2D-RFT formulation and lets the force on a sub-surface be deemed independent of the surface's speed. More recently, an inertia-sensitive 2D-RFT has also been proposed and validated [16]. We use a combination of granular inertial number (I) and Froude Number (Fr), to determine the quasi-static conditions in a granular intrusion system. Low values of I and Fr indicate insignificant *micro-inertial* and *macro-inertial* effects, in gravity-loaded granular intrusion systems. In general, 3D-RFT formulation can be applied to systems with $I < 0.1$ and $Fr < 0.4$. See Appendix C.1 for details. We also require that intruders are only submerged to a shallow depth. This comes from limits on the linearity of granular material's resistance with depth $|z|$ in a gravity-loaded system and limits us to considering depths only up to a $O(1)$ factor of the size of the object being intruded [17, 119]. Lastly, the RFT form assumes a scale-separation by treating granular media with a local continuum model. The assumption holds when the intruding object's length scales are large compared to grain diameter. RFT is expected to have a limited performance in regions of sharp corners on intruders where the media begins to show its granular nature and direct grain-size effects may be important.

In addition to the above premises, we will utilize a few operational constraints. We limit ourselves to quasi-static intruder motion, which assumes the absence of any inertial effects in the system. This was also assumed in the original 2D-RFT formulation and lets the force on a sub-surface be deemed independent of the surface's speed. More recently, an inertia-sensitive 2D-RFT has also been proposed and validated [16]. We also require that intruders are only submerged to a shallow depth. This comes from limits on the linearity of granular material's resistance with depth $|z|$ in a gravity-loaded system and limits us to considering depths only up to a $O(1)$ factor of the size of the object being intruded [17, 119]. Lastly, the RFT form assumes a scale-separation by treating granular media with a local continuum model. The assumption holds when the intruding object's length scales are large compared to grain diameter. RFT is expected to have a limited performance in regions of sharp corners on intruders where the media begins to show its granular nature, and direct grain-size effects may be important.

5.5 Proposed form of 3D-RFT

In light of Premise 1, we propose a 3D-RFT taking the same form as Eq 5.2 — the force per area grows proprotional to depth $|z|$ and depends on some vector-valued function of the input vectors $\{\hat{\boldsymbol{n}}, \hat{\boldsymbol{v}}, \boldsymbol{g}\}$, which are now three-dimensional. In particular, referring to Premise 4, we write

$$\boldsymbol{\alpha}^{\text{mat}}(\hat{\boldsymbol{n}}, \hat{\boldsymbol{v}}, \boldsymbol{g}) = \boldsymbol{\alpha}(\hat{\boldsymbol{n}}, \hat{\boldsymbol{v}}, \boldsymbol{g}; \rho_c, \mu_{\text{s}}, \mu_{\text{surf}})\,. \tag{5.3}$$

Further, we assume the force per area per depth can be decomposed into normal and tangential parts with the following property dependences, which align with Premises 5 and 6:

$$\boldsymbol{\alpha} = \boldsymbol{\alpha}_n(\hat{\boldsymbol{n}}, \hat{\boldsymbol{v}}, \boldsymbol{g}; \rho_c, \mu_{\text{s}}) + \boldsymbol{\alpha}_t(\hat{\boldsymbol{n}}, \hat{\boldsymbol{v}}, \boldsymbol{g}; \rho_c, \mu_{\text{s}}, \mu_{\text{surf}})\,, \tag{5.4}$$

where $\boldsymbol{\alpha}_n$ and $\boldsymbol{\alpha}_t$ represent normal and tangential contributions to $\boldsymbol{\alpha}$. We propose the following simplifying functional forms

$$\boldsymbol{\alpha}_n = \rho_c g \hat{f}(\mu_{\text{s}})\, |\boldsymbol{\alpha}_n^{\text{gen}}(\hat{\boldsymbol{n}}, \hat{\boldsymbol{v}}, \hat{\boldsymbol{g}})|\, (-\hat{\boldsymbol{n}}) \tag{5.5}$$

$$\boldsymbol{\alpha}_t = \rho_c g \hat{f}(\mu_{\text{s}}) \min\left(\frac{\mu_{\text{surf}}\, |\boldsymbol{\alpha}_n^{\text{gen}}(\hat{\boldsymbol{n}}, \hat{\boldsymbol{v}}, \hat{\boldsymbol{g}})|}{|\boldsymbol{\alpha}_t^{\text{gen}}(\hat{\boldsymbol{n}}, \hat{\boldsymbol{v}}, \hat{\boldsymbol{g}})|},\, 1\right) \boldsymbol{\alpha}_t^{\text{gen}}(\hat{\boldsymbol{n}}, \hat{\boldsymbol{v}}, \hat{\boldsymbol{g}})\,. \tag{5.6}$$

The prefactor $\rho_c g \hat{f}(\mu_{\text{s}})$, which we collectively refer to as ξ_n, is a media dependent scaling coefficient reflecting the overall intrusive strength of the system. The presence of the multiplicative $\rho_c g$ factor is required on dimensional grounds [146]. Additionally,

we find that $\hat{f}$ follows a cubic dependence on μ_s (see Fig C-2 in Appendix C for more details). This dependence is in-line with the observations of many researchers in the past in simpler vertical intrusions of flat plates in granular volumes (a sub-case of 3D-RFT)[77]. Section C.2 provides the detailed material response graphs in this regard.

The *generic* RFT functions shown with superscript 'gen' are labeled as such because we model them to be approximately universal across all systems. The min function in the formula for $\boldsymbol{\alpha}_t$ acts as a cut-off that ensures the ratio of tangential and normal forces on a plate does not exceed the media-surface friction coefficient μ_{surf}, as per Premise 6.

The largest meaningful value of μ_{surf} is $\mu_{\text{surf}} = \mu_s$, which is the fully-rough limit wherein the min function is always 1. In this case, we have $\boldsymbol{\alpha} = \xi_n \boldsymbol{\alpha}^{\text{gen}}$ where

$$\boldsymbol{\alpha}^{\text{gen}} \equiv \boldsymbol{\alpha}_n^{\text{gen}} + \boldsymbol{\alpha}_t^{\text{gen}} \,. \tag{5.7}$$

The 3D-RFT model we are proposing is closed upon choosing the scalar-valued function $\hat{f}$ and the vector valued function $\boldsymbol{\alpha}^{\text{gen}}$. Upon selection of these two functions, Eqs 5.5 and 5.6 can be used to determine $\boldsymbol{\alpha}$, and hence $\boldsymbol{\alpha}^{\text{mat}}$, for any choice of μ_s and μ_{surf}.

5.6 Further simplifications

5.6.1 Symmetry constraints

We use symmetry constraints inherent to the drag problem (Premise 7) to the constrain the functional form of $\boldsymbol{\alpha}^{\text{gen}}$. Our strategy is to constrain the function space to satisfy symmetry constraints *'by design'* rather than leaving it to chance based on the choice of fit functions. Moreover, by enforcing the symmetry constraints directly, we reduce the space of admissible functions, thereby reducing the amount of fitting that must be done.

Consider a small plate intruder characterized with $\hat{\boldsymbol{n}}$, $\hat{\boldsymbol{v}}$, ds, $|\boldsymbol{z}|$, and $\boldsymbol{g}$. For large μ_{surf}, the force on the plate according to RFT is $\boldsymbol{df} = \xi_n \boldsymbol{\alpha}^{\text{gen}}(\hat{\boldsymbol{n}}, \hat{\boldsymbol{v}}, \boldsymbol{g})|z|ds$. If the entire system is rotated — including the intruder, the granular bed, and gravity — the resistive force on the intruder must rotate by the same amount. This is because rotating the entire system should be consistent with a fixed system and a rotation of the observer. Figure 5-5A visualizes this action. Thus, for any rotation $\boldsymbol{R}$, we expect that $\boldsymbol{R}\,\boldsymbol{df} = \xi_n \boldsymbol{\alpha}^{\text{gen}}(\boldsymbol{R}\hat{\boldsymbol{n}}, \boldsymbol{R}\hat{\boldsymbol{v}}, \boldsymbol{R}\hat{\boldsymbol{g}})|z|ds$, and thus

$$\boldsymbol{\alpha}^{\text{gen}}(\boldsymbol{R}\hat{\boldsymbol{n}}, \boldsymbol{R}\hat{\boldsymbol{v}}, \boldsymbol{R}\hat{\boldsymbol{g}}) = \boldsymbol{R}\boldsymbol{\alpha}^{\text{gen}}(\hat{\boldsymbol{n}}, \hat{\boldsymbol{v}}, \hat{\boldsymbol{g}}) \,. \tag{5.8}$$

This *'global rotation constraint'* implies the $\boldsymbol{\alpha}^{\text{gen}}$ is an isotropic functions of its inputs. Thus, in accord with Isotropic Representation Theory (IRT)[171] the generic function must have the following specific form:

$$\boldsymbol{\alpha}^{\text{gen}}(\hat{\boldsymbol{n}}, \hat{\boldsymbol{v}}, \hat{\boldsymbol{g}}) = f_1\hat{\boldsymbol{n}} + f_2\hat{\boldsymbol{v}} + f_3\hat{\boldsymbol{g}}\,, \tag{5.9}$$

where f_1, f_2, and f_3 are three mutually-independent arbitrary scalar-valued functions of coordinate-invariant *dot-products* between the three directions vectors, that is $f_i = f_i(\hat{\boldsymbol{g}} \cdot \hat{\boldsymbol{v}}, \hat{\boldsymbol{g}} \cdot \hat{\boldsymbol{n}}, \hat{\boldsymbol{n}} \cdot \hat{\boldsymbol{v}})$. Equation 5.9 has reduced the problem of fitting $\boldsymbol{\alpha}^{\text{gen}}$ from determining a vector-valued function of six independent variables (three vectors with unital constraints) to determining a vector-valued function of three independent variables (three dot products). Note that the form given in Eqs 5.5-5.6 continues to satisfy Eq 5.16 and the IRT requirement Eq 5.9. A detailed proof in this regard is provided in section C.4.

We next introduce the methodology for parametrizing subsurfaces in terms of three angles to arrive at our ultimate description of $\boldsymbol{\alpha}^{\text{gen}}$.

5.6.2 Sub-surface characterization

Use of a local coordinate frame

The proposed form of 3D-RFT (Eqs 5.5-5.9) defines the stress-per-depth on a sub-surface, $\boldsymbol{\alpha}$, only using $\hat{\boldsymbol{n}}$, $\hat{\boldsymbol{v}}$, and $\hat{\boldsymbol{g}}$ directions (beside material properties). Thus, to simplify 3D-RFT outputs, we define a local cylindrical coordinate frame at each sub-surface based on its local velocity ($\hat{\boldsymbol{v}}$) and gravity direction ($\hat{\boldsymbol{g}}$). We choose the direction opposite to the gravity (upward in general) as the positive z-direction and use the horizontal component of $\hat{\boldsymbol{v}}$ as the positive $\hat{\boldsymbol{r}}$ direction. The remaining $\hat{\boldsymbol{\theta}}$ direction is chosen as the cross product between $\hat{\boldsymbol{r}}$ and $\hat{\boldsymbol{z}}$. The free-surface is taken as the reference ($z = 0$) for the z-direction.

$$\begin{aligned}
\text{local } z-\text{direction} \quad &: \quad \hat{\boldsymbol{z}} = -\hat{\boldsymbol{g}} \\
\text{local } r-\text{direction} \quad &: \quad \hat{\boldsymbol{r}} = \frac{\boldsymbol{v} - (\boldsymbol{v}\cdot\hat{\boldsymbol{z}})\hat{\boldsymbol{z}}}{|\boldsymbol{v} - (\boldsymbol{v}\cdot\hat{\boldsymbol{z}})\hat{\boldsymbol{z}}|} \\
\text{local } \theta-\text{direction} \quad &: \quad \hat{\boldsymbol{\theta}} = \hat{\boldsymbol{z}} \times \hat{\boldsymbol{r}}
\end{aligned} \tag{5.10}$$

When $|\boldsymbol{v} - (\boldsymbol{v}\cdot\hat{\boldsymbol{z}})\hat{\boldsymbol{z}}|$ is zero (a sub-surface moves up or down), $\hat{\boldsymbol{r}}$ is set to the direction of horizontal component of the surface-normal i.e. $\hat{\boldsymbol{r}} = (\hat{\boldsymbol{n}} - (\hat{\boldsymbol{n}}\cdot\hat{\boldsymbol{z}})\hat{\boldsymbol{z}})/|\hat{\boldsymbol{n}} - (\hat{\boldsymbol{n}}\cdot\hat{\boldsymbol{z}})\hat{\boldsymbol{z}}|$. Next, in line with Premise 8, we cast the plate orientation and motion in terms of angles β, γ, and ψ. We also highlight that though the 3D-RFT form obtained in eq 5.9 could have been a valid candidate for 3D-RFT form, the use of $\{\hat{\boldsymbol{r}}, \hat{\boldsymbol{\theta}}, \hat{\boldsymbol{z}}\}$ instead

of $\{\hat{\boldsymbol{n}}, \hat{\boldsymbol{v}}, \hat{\boldsymbol{g}}\}$ as the co-ordinate basis has numerous advantages. First, the choice enables expressing system states in terms of charateristic angles $\{\beta, \gamma, \psi\}$ which in turn helps us meet our desire to maintain a consistency of 3D-RFT with 2D-RFT form (premises-8). Secondly, unlike $\{\hat{\boldsymbol{n}}, \hat{\boldsymbol{v}}, \hat{\boldsymbol{g}}\}$, $\{\hat{\boldsymbol{r}}, \hat{\boldsymbol{\theta}}, \hat{\boldsymbol{z}}\}$ represent an orthogonal co-ordinate frame. Use of this choice improves the physical interpretation of the generic values of $\boldsymbol{\alpha}^{\text{gen}}$ for being mutually orthogonal and thus help making design decisions based on 3D-RFT easier, if so required.

Sub-surface orientations

We use the sub-surface's normal direction $\hat{\boldsymbol{n}}$ to characterize its orientation in the local coordinate frame. We use two angles, the angle of twist (ψ or ψ) and the angle of tilt (β) for this characterization. See figure 5-4B for a visual representation of ψ and β.

Surface twist angle (ψ): We define ψ as the azimuthal angle between the r-axis and the projection of the surface normal onto the $r\theta$-plane, denoted by $\hat{\boldsymbol{n}}_{r\theta}$.

$$\begin{aligned}
\beta \quad = \quad & -\cos^{-1}(\hat{\boldsymbol{n}} \cdot \hat{\boldsymbol{z}}) && \text{if} \quad \hat{\boldsymbol{n}} \cdot \hat{\boldsymbol{r}} \geq 0 \quad \& \quad \hat{\boldsymbol{n}} \cdot \hat{\boldsymbol{z}} \geq 0 \\
& +\pi - \cos^{-1}(\hat{\boldsymbol{n}} \cdot \hat{\boldsymbol{z}}) && \text{if} \quad \hat{\boldsymbol{n}} \cdot \hat{\boldsymbol{r}} \geq 0 \quad \& \quad \hat{\boldsymbol{n}} \cdot \hat{\boldsymbol{z}} < 0 \\
& \cos^{-1}(\hat{\boldsymbol{n}} \cdot \hat{\boldsymbol{z}}) && \text{if} \quad \hat{\boldsymbol{n}} \cdot \hat{\boldsymbol{r}} < 0 \quad \& \quad \hat{\boldsymbol{n}} \cdot \hat{\boldsymbol{z}} \geq 0 \\
& -\pi + \cos^{-1}(\hat{\boldsymbol{n}} \cdot \hat{\boldsymbol{z}}) && \text{if} \quad \hat{\boldsymbol{n}} \cdot \hat{\boldsymbol{r}} < 0 \quad \& \quad \hat{\boldsymbol{n}} \cdot \hat{\boldsymbol{z}} < 0
\end{aligned} \tag{5.11}$$

Surface tilt angle (β): We define β as the polar angle between the r-axis and the $r\theta$-plane. To be clear, β measures the angle between the $r\theta$-plane and one of the $\hat{\boldsymbol{n}}$ and $-\hat{\boldsymbol{n}}$, whichever lies in $[-\pi/2, \pi/2]$ range. This choice is not problematic because at any time, only one of $-\hat{\boldsymbol{n}}$ and $\hat{\boldsymbol{n}}$ surfaces experiences resistive forces. The side experiencing the forces can be identified using the leading edge condition ($\hat{\boldsymbol{v}} \cdot \hat{\boldsymbol{n}} \geq 0$) of Premise 2.

$$\begin{aligned}
\psi \quad &= \quad \tan^{-1}\left((\hat{\boldsymbol{n}}_{r\theta} \cdot \hat{\boldsymbol{r}})/(\hat{\boldsymbol{n}}_{r\theta} \cdot \hat{\boldsymbol{r}})\right) \\
\text{where,} \quad \hat{\boldsymbol{n}}_{r\theta} &= \quad \frac{\hat{\boldsymbol{n}} - (\hat{\boldsymbol{n}} \cdot \hat{\boldsymbol{z}})\hat{\boldsymbol{z}}}{|\hat{\boldsymbol{n}} - (\hat{\boldsymbol{n}} \cdot \hat{\boldsymbol{z}})\hat{\boldsymbol{z}}|}
\end{aligned} \tag{5.12}$$

If $|\hat{\boldsymbol{n}} - (\hat{\boldsymbol{n}} \cdot \hat{\boldsymbol{z}})\hat{\boldsymbol{z}}| = 0$, set $\psi = 0$.

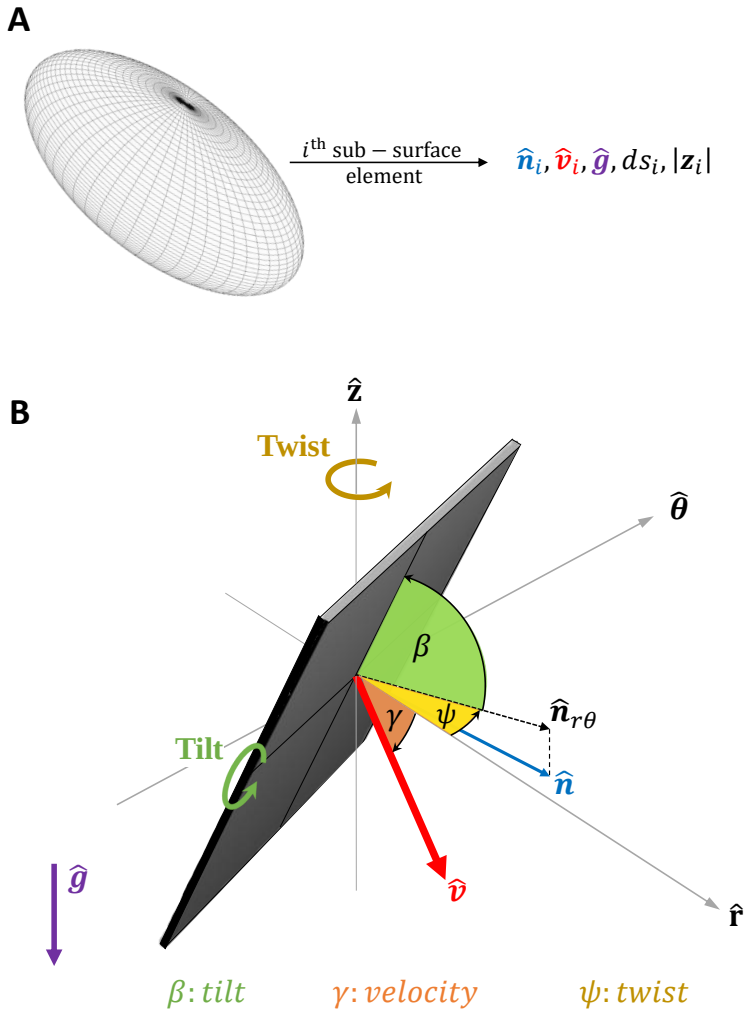

Figure 5-4: *3D-RFT sub-surface characterization*: (A) Any moving sub-surface is represented using a set of 5 system variables: surface normal ($\hat{\boldsymbol{n}}$), area magnitude (ds), depth ($|\boldsymbol{z}|$), velocity direction ($\hat{\boldsymbol{v}}$), and ($\hat{\boldsymbol{g}}$). For further simplification of the representation, $\hat{\boldsymbol{n}}$ and $\hat{\boldsymbol{v}}$ are expressed using (B) three characteristic angles — plate tilt angle (β, green), plate twist angle (ψ, yellow), and velocity angle (γ, orange), in the local coordinate frame $\{\hat{\boldsymbol{r}}, \hat{\boldsymbol{\theta}}, \hat{\boldsymbol{z}}\}$. The functional forms of these angles and local coordinate frame are given in eq 5.10 and 5.18- 5.20.

Velocity direction

The local coordinate frame definitions (Eq 5.10) keep the velocity vector completely within the rz-plane. Thus, once $\{\hat{\boldsymbol{r}}, \hat{\boldsymbol{\theta}}, \hat{\boldsymbol{z}}\}$ are determined, only one angle is needed to represent the velocity direction. We call this angle γ (see Fig 5-4B). We define γ

as the angle between the velocity direction vector and the local positive r-axis.

$$\begin{aligned} \gamma \quad &= \quad \cos^{-1}(\hat{\boldsymbol{v}} \cdot \hat{\boldsymbol{r}}) \quad \text{if} \quad \hat{\boldsymbol{v}} \cdot \hat{\boldsymbol{z}} \leq 0 \\ &\quad\; -\cos^{-1}(\hat{\boldsymbol{v}} \cdot \hat{\boldsymbol{r}}) \quad \text{if} \quad \hat{\boldsymbol{v}} \cdot \hat{\boldsymbol{z}} \geq 0 \end{aligned} \tag{5.13}$$

In case both $\hat{\boldsymbol{v}}$ and $\hat{\boldsymbol{n}}$ align to $\hat{\boldsymbol{z}}$ ($\gamma = \pm\pi/2$ and $\psi = 0$), set $\hat{\boldsymbol{r}}$ in global x-direction.

Based on the above definitions, the variations of each of the system characteristic angles (β, γ, ψ) is restricted to $[-\pi/2, \pi/2]$ for any leading-edge surface. We use these limits in the generation of reference 3D-RFT data. Mathematical formulas for the angles in terms of vector components in a fixed cartesian frame are provided in the Material and Methods section.

We express the final form of $\boldsymbol{\alpha}^{\text{gen}}$ in the local coordinate frame $\{\hat{\boldsymbol{r}}, \hat{\boldsymbol{\theta}}, \hat{\boldsymbol{z}}\}$ by expressing $\{\hat{\boldsymbol{n}}, \hat{\boldsymbol{v}}, \hat{\boldsymbol{g}}\}$ as:

$$\begin{aligned} &\hat{\boldsymbol{g}} = -\hat{\boldsymbol{z}}, \qquad\qquad \hat{\boldsymbol{v}} = \cos\gamma\, \hat{\boldsymbol{r}} - \sin\gamma\, \hat{\boldsymbol{z}} \\ &\hat{\boldsymbol{n}} = \sin\beta\cos\psi\, \hat{\boldsymbol{r}} + \sin\beta\sin\psi\, \hat{\boldsymbol{\theta}} - \cos\beta\, \hat{\boldsymbol{z}} \end{aligned} \tag{5.14}$$

Substitution of definitions in Eq 5.9 gives the expressions for the r, θ, and z components of $\boldsymbol{\alpha}^{\text{gen}}$ as follows:

$$\boldsymbol{\alpha}^{\text{gen}} = \alpha_r^{\text{gen}} \hat{\boldsymbol{r}} + \alpha_\theta^{\text{gen}} \hat{\boldsymbol{\theta}} + \alpha_z^{\text{gen}} \hat{\boldsymbol{z}} \tag{5.15}$$

$$\begin{aligned} \alpha_r^{\text{gen}}(\beta, \gamma, \psi) &= f_1 \sin\beta\cos\psi + f_2 \cos\gamma \\ \alpha_\theta^{\text{gen}}(\beta, \gamma, \psi) &= f_1 \sin\beta\sin\psi \\ \alpha_z^{\text{gen}}(\beta, \gamma, \psi) &= -f_1 \cos\beta - f_2 \sin\gamma - f_3 \end{aligned} \tag{5.16}$$

where, $f_1 = f_1(x_1, x_2, x_3)$, $f_2 = f_2(x_1, x_2, x_3)$, and $f_3 = f_3(x_1, x_2, x_3)$ are three functions of $\{x_1, x_2, x_3\}$ defined as:

$$\begin{aligned} &x_1 = \hat{\boldsymbol{g}} \cdot \hat{\boldsymbol{v}} = \sin\gamma, \qquad x_2 = \hat{\boldsymbol{g}} \cdot \hat{\boldsymbol{n}} = \cos\beta, \\ &x_3 = \hat{\boldsymbol{n}} \cdot \hat{\boldsymbol{v}} = \cos\psi\cos\gamma\sin\beta + \sin\gamma\cos\beta\,. \end{aligned} \tag{5.17}$$

The 3D-RFT model is closed upon fitting the three functions $f_i(x_1, x_2, x_3)$. Note that by building the functional relationships for α_r^{gen}, $\alpha_\theta^{\text{gen}}$, and α_z^{gen} from IRT (Eq 5.16), the model automatically satisfies many *easy-to-observe* local constraints regardless of the choice of the f_i's. These constraints include (i) *'plate twist symmetry'* (figure 5-5B), which requires that the sub-surface forces in the r- and z-direction should be even functions of plate twist (ψ), and that force in the θ-direction should be an odd function of ψ; (ii) *'plate tilt symmetry'* (figure 5-5C) which requires that

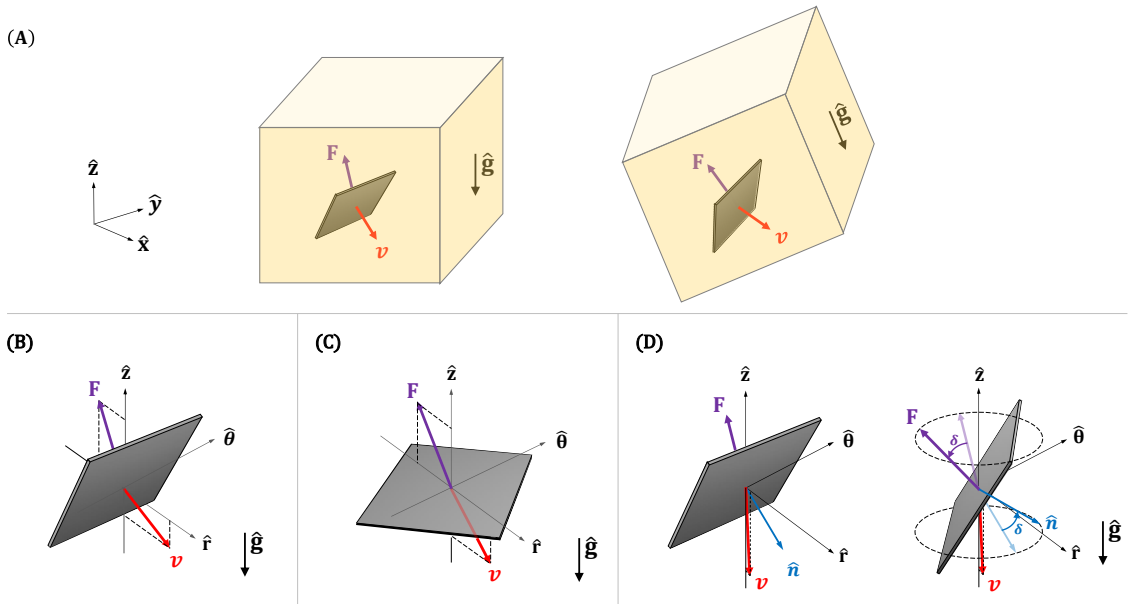

Figure 5-5: *3D-RFT symmetry constraints*: *(A) Global rotational constraint* requiring the drag force to be an isotropic function of the plate normal, motion direction, and gravity direction. Some consequences of this constraint are *plate twist symmetry*, *plate tilt symmetry*, and *vertical motion symmtry*. *(B)* A special case of *plate twist symmetry*: $F_\theta(\beta, \gamma, \psi = 0) = 0$. *(C)* A special case of *plate tilt symmetry*: $F_\theta(\beta = 0, \gamma, \psi) = 0$, and *(D) Vertical motion symmetry*: $(\beta, \gamma = \pm\pi/2, \psi = 0) \rightarrow (\beta, \gamma = \pm\pi/2, \psi = \delta)$ causes $(F_r, F_\theta = 0, F_z) \rightarrow (F_r \cos\delta, F_r \sin\delta, F_z)$. Violet, red, and blue arrows show force, velocity, and surface-normal direction, respectively.

when the plate faces upwards or downwards ($\beta = 0$), the sub-surface force in the θ-direction should vanish, the force magnitude should depend only on γ, and the twist angle ψ should have no influence on the force; and (iii) *'vertical motion symmetry'* (figure 5-5D), which requires that as $\gamma \rightarrow \pm\pi/2$ (approaching an upward or downward motion) any azimuthal rotation (changing ψ at constant β) of a sub-surface should rotate the resultant force on the sub-surface by the same angle. We use third degree polynomials fit f_1, f_2, and f_3 (see table C.3 and table C.4 in Appendix C).

5.7 Reference data and the form of 3D-RFT

We use a large number of combinations (~ 3000) of material properties $(\rho_c, \mu_s, \mu_{surf})$ and 3D-RFT reference variables (β, γ, ψ) to generate continuum modeling-based reference data for evaluating the 3D-RFT form. In regards to the material properties we use five material internal friction values ($\mu_s = [0.3, 0.4, 0.5, 0.7, 0.9]$) with two values of surface friction (μ_{surf}) in each case. For $\mu_s = 0.4$ we use 3 instead of 2 μ_{surf}

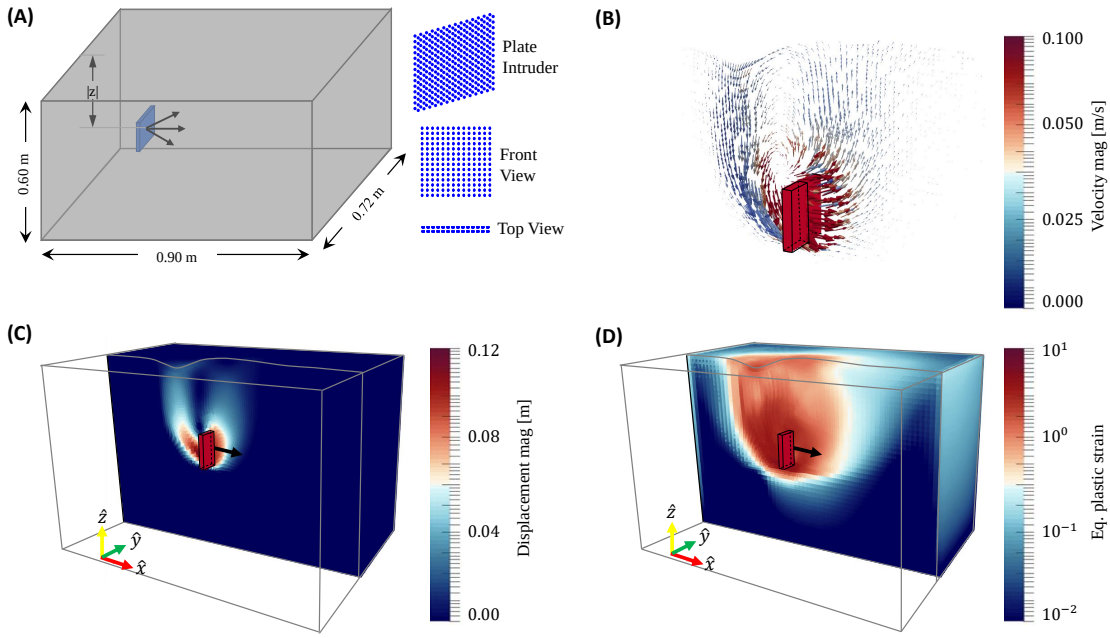

Figure 5-6: *Reference data collection for 3D-RFT*: (A) We use a thin plate (0.105m×0.105m×0.015m) intrusion setup as shown in the schematic for reference data collection for 3D-RFT. We use material point method (MPM) based continuum modeling for data collection. We run 13 combinations of plate tilt angle ($\beta = -\pi/2 : \pi/6 : \pi/2$ rad), 13 combinations of velocity direction angle ($\gamma = -\pi/2 : \pi/6 : \pi/2$ rad), and 7 combinations of plate twist angle ($\psi = 0 : \pi/6 : \pi/2$. (B) material flow, (C)displacement magnitude, and (D)equivalent plastic strain magnitude variation from one of the test setups. Material properties are provided in Appendix-I

values. For each of the 11 combinations of μ_s and μ_{surf}, we conduct plate intrusions at 7 combinations of plate tilt angle ($\beta = -\pi/2 : \pi/6 : \pi/2$ rad), 7 combinations of velocity direction angle ($\gamma = -\pi/2 : \pi/6 : \pi/2$ rad), and 4 combinations of plate twist angle ($\psi = 0 : \pi/6 : \pi/2$). For the $\{\mu_s = 0.40, \mu_{surf} = 0.15\}$, we use 13 combinations of β ($\pi/2 : \pi/6 : \pi/2$ rad), 13 combinations of γ ($-\pi/2 : \pi/6 : \pi/2$ rad), and 4 combinations of ψ ($0 : \pi/6 : \pi/2$). Additionally, we conduct plate intrusion simulations at $\{\mu_s = 0.2, \mu_{surf} = 0.2\}$ and $\{\mu_s = 0.1, \mu_{surf} = 0.1\}$ at $\psi = 0$ to evaluate ξ_n at $\mu_s = 0.1$ and 0.2. We do not explore ψ in $[-\pi/2 : 0]$ range for the reference data as α_r, α_z, and α_θ are known to be even, even, and odd (resp.) in ψ from 'plate twist symmetry'. The polynomial fits for $\hat{f}_1$, $\hat{f}_2$, and $\hat{f}_3$ are provided in the Appendix C (Table C.3 and Table C.4).

The polynomial fits for f_1, f_2, and f_3 are provided in the Appendix C (Table C.3 and table C.4). Figure 5-6 show the simulation setup used for the data collection.

While both the β and the γ angles are varied over the interval $[-\pi/2, \pi/2]$, ψ was varied only in $[0, \pi/2]$ taking advantage of *'plate twist symmetry'* discussed earlier.

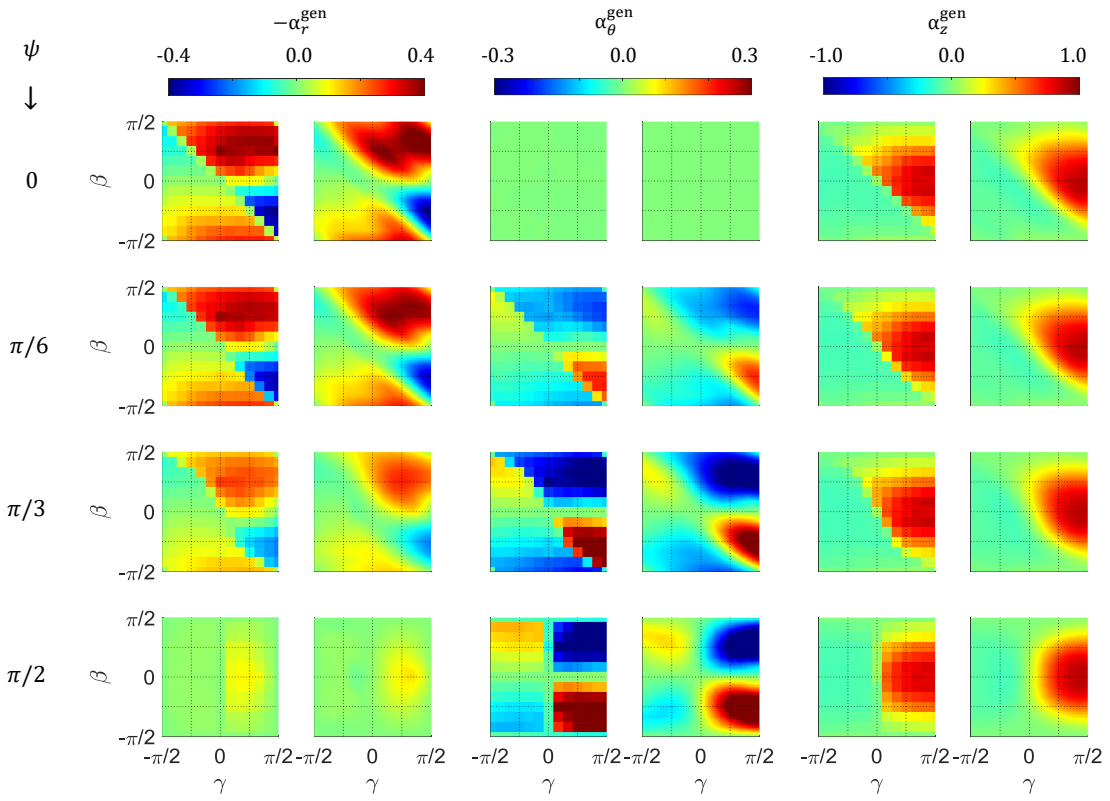

Figure 5-7: *Sample 3D-RFT fittings*: Reference normalized forces $(F/A|\boldsymbol{z}|\xi_n)$ and functional fittings (right) for plate intrusions at various plate twists ($\psi = [0, \pi/6, \pi/3, \pi/2]$ rad), plate inclinations ($\beta = -\pi/2 : \pi/6 : \pi/2$ rad), and velocity directions ($\gamma = -\pi/2 : \pi/6 : \pi/2$ rad) for a material with $\mu_s = 0.4$, $\rho_c = 3000$ kg/m^3, and $\mu_{surf} = 0.15$. The reference data is normalized with $\xi_n = 0.92 \times 10^6$ N/m^3.

Figure 5-7 shows an example of 3D-RFT fittings aginst reference data. Odd columns in the figure show the data obtained using continuum simulations as a function of β and γ at four ψ values. The material properties were $\mu_s = 0.4$, $\rho_c = 3000$ kg/m^3, and $\mu_{surf} = 0.15$. Corresponding 3D-RFT fittings are plotted on the even columns. We find the values of scaling coefficient ξ_n to be 0.92×10^6 N/m^3 for this material. While the eq 5.16 represents the most generic form of 3D-RFT derived using systems constraints, the choice of $\hat{f}_{1,2,3}\{x_1, x_2, x_3\}$ decides the complexity and accuracy of 3D-RFT form. All the results presented in this work use 3rd degree polynomial fits in $\{x_1, x_2, x_3\}$ (Table C.3) for $\hat{f}_1$, $\hat{f}_2$, and $\hat{f}_3$. Higher order polynomials

which better fit the reference data could be obtained using higher degree polynomial fits. We provide one such form in Appendix C (Table C.4). The performance of 3D-RFT does not changes significantly between 3$^{\text{rd}}$ and 4$^{\text{th}}$ degree polynomial fits. The latter form fits the trends of $|\boldsymbol{\alpha}_t|/|\boldsymbol{\alpha}_n|$ better but has inconsequencial effects on 3D-RFT predictions for the test cases used in this study.

The 3D-RFT model we propose is summarized by Eqs 5.2-5.7, with $\hat{f}$ fit as shown in Fig C-2, and with $\boldsymbol{\alpha}^{\text{gen}}$ expressed using Eqs 5.14-5.16 in terms of directions $\{\hat{\boldsymbol{r}}, \hat{\boldsymbol{\theta}}, \hat{\boldsymbol{z}}\}$ and angles $\{\beta, \gamma, \psi\}$ as fit functions shown in Fig 5-6. To numerically implement the model, we discretize the intruder surface into small plate elements and determine $\{\beta, \gamma, \psi\}$ and $\{\hat{\boldsymbol{r}}, \hat{\boldsymbol{\theta}}\}$ for each element. The model then provides the force on each element that is on the leading edge of the intruder. A step-by-step implementation strategy for 3D-RFT is given in section 5.8.

5.8 Step-by-step 3D-RFT implementation

We use an explicit iterative scheme to implement 3D-RFT in this study. The strategy primarily consists three parts — (1) discretizing the intruder surface into small sub-surfaces, (2) finding the sub-surface forces using sub-surface orientation angles (β and ψ), velocity angle (γ), area (ds), and depth from the free surface ($|\boldsymbol{z}|$), and (3) summing over all sub-surfaces to find the net resistive force and moment response. A step-by-step implementation of the strategy is provided below:

Step 1: Discretize the intruder surface into smal plane sub-surface elements. We use the open-source software, 'Blender' (version 2.91) for modeling and discretizing various intruder geometries in our study (using .wrl format).

Step 2: Calculate the velocity direction vector $\hat{\boldsymbol{v}}$, surface normal $\hat{\boldsymbol{n}}$, and depth from the free surface $|\boldsymbol{z}|$ for each sub-surface. And repeat step 3-11 for each sub-surface.

Step 3: Check if $\hat{\boldsymbol{n}} \cdot \hat{\boldsymbol{v}} \geq 0$ (sub-surface is a 'leading edge') and $z < 0$ (sub-surface is submerged in the media). If both the conditions are met, follow step 4-11. If they are not, set the sub-surface resistive force to zero and consider the next sub-surface.

Step 4: Find local coordinate frame $\{\hat{\boldsymbol{r}}, \hat{\boldsymbol{\theta}}, \hat{\boldsymbol{z}}\}$ using eq 5.10.

Step 5: Find RFT characteristic angles (β, γ, ψ) using $\hat{\boldsymbol{v}}$, $\hat{\boldsymbol{n}}$, and local coordinate frame $\{\hat{\boldsymbol{r}}, \hat{\boldsymbol{\theta}}, \hat{\boldsymbol{z}}\}$ as follows:

Find the surface characteristic angle β as :

$$\begin{aligned}
\beta \quad = \quad & -\cos^{-1}(\hat{\boldsymbol{n}}\cdot\hat{\boldsymbol{z}}) && \text{if} \quad \hat{\boldsymbol{n}}\cdot\hat{\boldsymbol{r}} \geq 0 \quad \& \quad \hat{\boldsymbol{n}}\cdot\hat{\boldsymbol{z}} \geq 0 \\
& +\pi - \cos^{-1}(\hat{\boldsymbol{n}}\cdot\hat{\boldsymbol{z}}) && \text{if} \quad \hat{\boldsymbol{n}}\cdot\hat{\boldsymbol{r}} \geq 0 \quad \& \quad \hat{\boldsymbol{n}}\cdot\hat{\boldsymbol{z}} < 0 \\
& \cos^{-1}(\hat{\boldsymbol{n}}\cdot\hat{\boldsymbol{z}}) && \text{if} \quad \hat{\boldsymbol{n}}\cdot\hat{\boldsymbol{r}} < 0 \quad \& \quad \hat{\boldsymbol{n}}\cdot\hat{\boldsymbol{z}} \geq 0 \\
& -\pi + \cos^{-1}(\hat{\boldsymbol{n}}\cdot\hat{\boldsymbol{z}}) && \text{if} \quad \hat{\boldsymbol{n}}\cdot\hat{\boldsymbol{r}} < 0 \quad \& \quad \hat{\boldsymbol{n}}\cdot\hat{\boldsymbol{z}} < 0
\end{aligned} \tag{5.18}$$

Remember that this β corresponds to only *'leading edges'* as non 'leading-edge' sub-surface never reach this step.

Find the velocity characteristic angle γ as :

$$\begin{aligned}
\gamma \quad = \quad & \cos^{-1}(\hat{\boldsymbol{v}}\cdot\hat{\boldsymbol{r}}) && \text{if} \quad \hat{\boldsymbol{v}}\cdot\hat{\boldsymbol{z}} \leq 0 \\
& -\cos^{-1}(\hat{\boldsymbol{v}}\cdot\hat{\boldsymbol{r}}) && \text{if} \quad \hat{\boldsymbol{v}}\cdot\hat{\boldsymbol{z}} \geq 0
\end{aligned} \tag{5.19}$$

Find the surface characteristic angle ψ as :

$$\psi \quad = \quad \tan^{-1}\left((\hat{\boldsymbol{n}}_{r\theta}\cdot\hat{\boldsymbol{r}})/(\hat{\boldsymbol{n}}_{r\theta}\cdot\hat{\boldsymbol{r}})\right) \tag{5.20}$$

$$\text{where,} \quad \hat{\boldsymbol{n}}_{r\theta} = \quad \frac{\hat{\boldsymbol{n}} - (\hat{\boldsymbol{n}}\cdot\hat{\boldsymbol{z}})\hat{\boldsymbol{z}}}{|\hat{\boldsymbol{n}} - (\hat{\boldsymbol{n}}\cdot\hat{\boldsymbol{z}})\hat{\boldsymbol{z}}|}$$

If $|\hat{\boldsymbol{n}} - (\hat{\boldsymbol{n}}\cdot\hat{\boldsymbol{z}})\hat{\boldsymbol{z}}| = 0$, set $\psi = 0$. In case both $\hat{\boldsymbol{v}}$ and $\hat{\boldsymbol{n}}$ align to $\hat{\boldsymbol{z}}$ ($\gamma = \pm\pi/2$ and $\psi = 0$), set $\hat{\boldsymbol{r}}$ in global x-direction.

Step 6: Calculate $\{x_1, x_2, x_3\}$ using Eq 5.17 and calculate f_1, f_2, f_3 using table C.3 (or table C.4).

Step 7: Calculate the values of $\{\alpha_r^{\text{gen}}, \alpha_\theta^{\text{gen}}, \alpha_z^{\text{gen}}\}$ using Eq 5.16 and table C.3.

Step 8: Estimate the media specific scaling factor ξ_n using expected functional form of ξ_n from section C.2 and Fig C-2 of the Supporting Information if the media effective density (ρ_c), gravity magnitude (g), and media internal friction coefficient (μ_{int}) are known. Alternatively, obtain ξ_n from vertical plate intrusion experiments (intrusion of a thin flat plate of area ds at $\beta = 0$, $\psi = 0$, and $\gamma = \pi/2$) using the following formula:

$$\xi_n = \frac{F_{\text{vertical}}}{\alpha_z^{\text{gen}}\big(\beta = 0, \gamma = \pi/2, \psi = 0\big) \times ds \times |\boldsymbol{z}|} \tag{5.21}$$

where, $|\boldsymbol{z}|$ corresponds to the average depth of the plate from the free surface at which the force is measured.

Step 9: Calculate the system specific $\boldsymbol{\alpha}_n$ and $\boldsymbol{\alpha}_t$ in the local coordinate frame using Eq 5.5-5.6 and add them up (Eq 5.4) to get $\boldsymbol{\alpha}$.

Step 10: Calculate $\{\alpha_x, \alpha_y, \alpha_z\}$ using Eq 5.15 by substituting triad $\{\hat{\boldsymbol{r}}, \hat{\boldsymbol{\theta}}, \hat{\boldsymbol{z}}\}$ from Eq 5.10.

Step 11: Calculate the net resistive force on the sub-surface by multiplying the triad $\{\alpha_x, \alpha_y, \alpha_z\}$ with sub-surface depth ($|\boldsymbol{z_i}|$), and area (ds_i)

Step 12: Sum up the forces on all the sub-surfaces to find the net force and moment on the intruder using locality and additivity of granular resistive forces.
Once the net resistive force on the intruder is known, one can use momentum balance equations to further model the intruder motion. Convergence studies are also done to determine the discretization.

5.9 Verification studies: Using continuum modeling

We first verify the accuracy of the proposed form of 3D-RFT by comparing its predictions for ten arbitrary intruding objects to full continuum model solutions of the same intrusions. We use the material properties $\mu_{\text{int}} = 0.4$, $\rho_c = 3000$ kg/m^3, and $\mu_{\text{surf}} = 0.4$ for these cases. The intruder shapes include *(1)*a 5 cm radius sphere, *(2)* an ellipsoid with $[7.5, 4.5, 4.5]$ cm semi-axes (x,y,z), *(3)* a 7.5 cm edge cube rotated by $\pi/4$ radian along the z-axis passing through its center from the initial alignment to the cartesian coordinate frame, *(4)* a 7.5 cm cube sequencially rotated by $\pi/3$ and $\pi/4$ radians along the y-axis and the z-axis passing through its center from the initial alignment to the cartesian coordinate frame, *(5)* a 7.5 cm cube sequentially rotated by $\pi/6$ and $\pi/3$ radians along y-axis and z-axis passing through its center respectively from its initial alignment to cartesian coordinate frame, *(6)* an iscosceles right angle prism with 7.5 cm equal sides and 10.5 cm width, *(7)* a quarter ellipsoid with $[7.5, 4.5, 4.5]$ cm semi-axes ($x > 0$ and $y > 0$), *(7)* a iscosceles right angle prism with equal sides of 10.5 cm and 7.5 cm width, *(9)* an half-ellipsoid with $[7.5, 4.5, 4.5]$ cm semi-axes ($y > 0$), and *(10)* a monkey shape from the open-source 3D computer graphics software *'Blender'* at a scale factor of 0.075 and facing $\pi/4$ rad from the positive x-direction in xy-plane. A representation of the objects and their dimensions are provided in Fig 5-8 and its caption. The object length scales are kept to be 7 cm in all the cases, and the objects are submerged to an initial depth of 27 cm (vertical distance between the free surface and the geometric center of the shape). The ob-

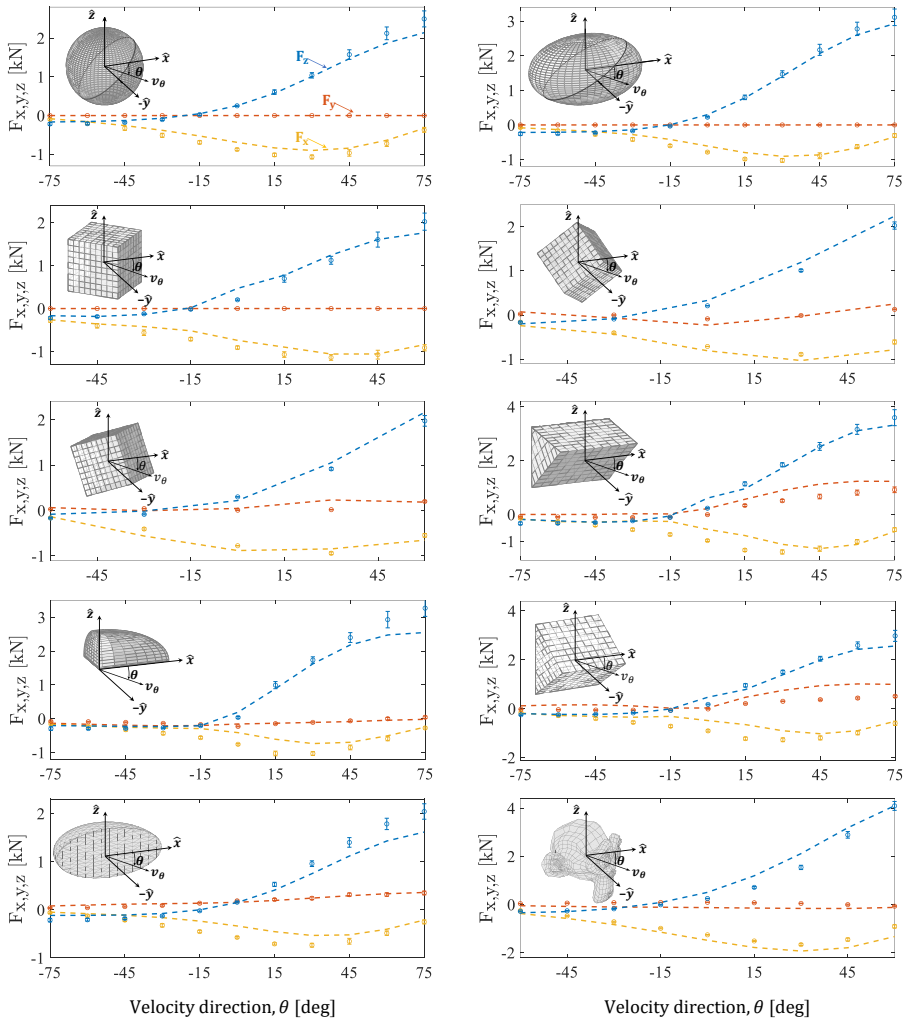

Figure 5-8: *3D-RFT Verification studies 1-10*: Variation of different force components (F_x: yellow, F_y: orange, and F_z: blue) during motions of various rigid objects (intruders) obtained from continuum modeling ('o' markers) and 3D-RFT (dashed lines) at various velocity directions ($\hat{\boldsymbol{v}}_\theta$). All the studies were conducted at a velocity magnitude of 0.1 m/s. θ represents the angle between $\hat{\boldsymbol{v}}_\theta$ and the positive x-axis in clockwise direction. All the velocities completely lie in $x-z$ plane. A pictorial representation of each intruder is provided in the corresponding sub-figure. The continuum modeling simulations use a effective material density ($\rho_c = \phi_c \times \rho_g$) of 3000 kg/m^3, an internal friction (μ_s) of 0.4, and surface friction (μ_{surf}) of 0.4. All the objects were submerged to an initial center-depth of 27 cm.

jects are moved at a speed of 0.1 m/s in different directions in the xz-plane. These directions are characterized using θ, which represents the angle between a velocity

direction ($\hat{\boldsymbol{v}}_\theta$) and the positive x-axis in a clockwise direction (same as γ definition for a plate element). Negative θ represents upward motion, positive θ represents downward motion, and $\theta = 0$ represents horizontal motion along x-axis. The variations of net-force (F_x, F_y, and F_z) with θ are plotted in figure 5-8. We expect no *micro-inertial* effects in these test cases as we use a rate-independent constitutive law for modeling reference solutions. We find the $Fr \approx 0.12$ ($L \approx 0.07\,\mathrm{m},\ v = 0.1\,\mathrm{m/s}$). Thus, 3D-RFT is a valid approach for modeling these cases. 3D-RFT agrees with the continuum solutions well in modeling all the intrusion test scenarios considered in Fig 5-8. The matches are better in some cases than others. Objects with sharp corners generally show weaker fits to those with smoother shapes. This could be because sharp corners are difficult to represent with our material point method. Similarly, symmetric objects show better fits than asymmetric objects.

5.10 Verification studies: Using detailed DEM modeling

We further verify the performance of 3D-RFT with two DEM studies. In these studies, we measure net moment, net force, as well as resistive force distribution on bodies intruding into granular volumes with simultaneous rotation and translation velocities. We use a 50/50 split of 3 mm and 3.4 mm diameter (d) grains with a grain density of 2470 kg/m^3 and the granular volumes had an effective bulk density of $\sim$ 1410 kg/m^3 ($\phi = 0.57$) in both the DEM studies. We determine the internal coefficient of friction μ_s as 0.21 using a simple shear simulation setup. Section C.6 of Appendix C provides more details of the simple shear test setup and detailed material properties. We use a scaling coefficient (ξ_n) value of 0.136×10^6 N/m^3 for equivalent 3D-RFT studies based on the relations between $\xi_n/\rho_c g$ and μ_s in figure C-2. See Table C.1 and section C.2 for more details.

Cylinder Drill

In this test, we model simultaneous rotation and translation (drilling) of a *solid cylindrical* (diameter= 0.05 m, length=0.14 m) intruder along z-axis in a granular volume. The setup consists of approximately 6×10^5 particles in a ($100d\times100d\times70d$) sized granular bed. The setup dimensions and setup schematic are provided in figure 5-9. We find $I \approx 0.01$ and $Fr \approx 0.14$ ($L \approx 0.05\,\mathrm{m}$, $\omega = 4\pi\,\mathrm{rad/s}$, $v_\mathrm{intruder} = 0.1\,\mathrm{m/s}$) for this case. Thus, 3D-RFT is a valid approach for modeling this system. The figure also shows the variations of forces and moments on the intruder over time from DEM studies and 3D-RFT modeling. In addition, the figure shows the variation of stress over the intruder shape from DEM and 3D-RFT. All reported components (net force and moments, as well as stress distributions) show a strong match between the two approaches.

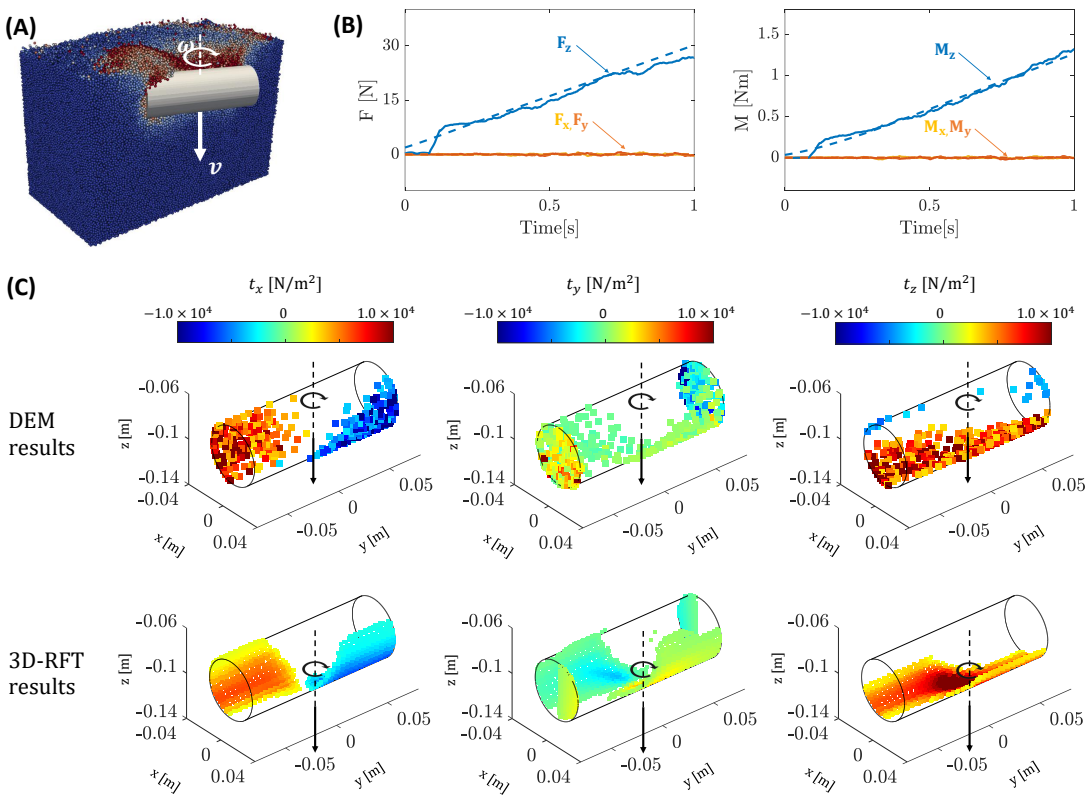

Figure 5-9: *DEM based 3D-RFT verification: Cylinder drill*: *(A)* A snapshot of the cylinder drill setup where a 5cm diameter and 14cm length cylinder was simultaneously rotated ($\omega = 4\pi$rad/s, clockwise) and translated ($v = 0.1$m/s, downwards) along z-axis. The grains are colored with velocity magnitudes. The simulation domain consisted $\sim 6 \times 10^5$ particle (50/50 split of 3 mm and 3.4 mm diameter (d) grains) spread over $100d \times 100d \times 70d$ physical space. *(B)* Variation of net force (F, left) and moment (M, right) components (x: yellow, y: orange, and z: blue) from DEM (solid lines) and 3D-RFT (dotted lines) . *(C)* Variation of various force commponets from DEM (Top) and 3D-RFT (Bottom) at a 10cm depth below the free surface ($t = 1s$). The DEM material properties are provided in table C.2 of the section C.6.

Bunny Drill

In this test, we model the drilling motion of a *Stanford Bunny*[172] shaped rigid intruder in a granular volume. The shape is an excellent example of a complex asymmetric 3D object, unlike the previous geometrically-simple solid cylinder shape, for testing the performance of 3D-RFT in modeling complex intruders. The granular

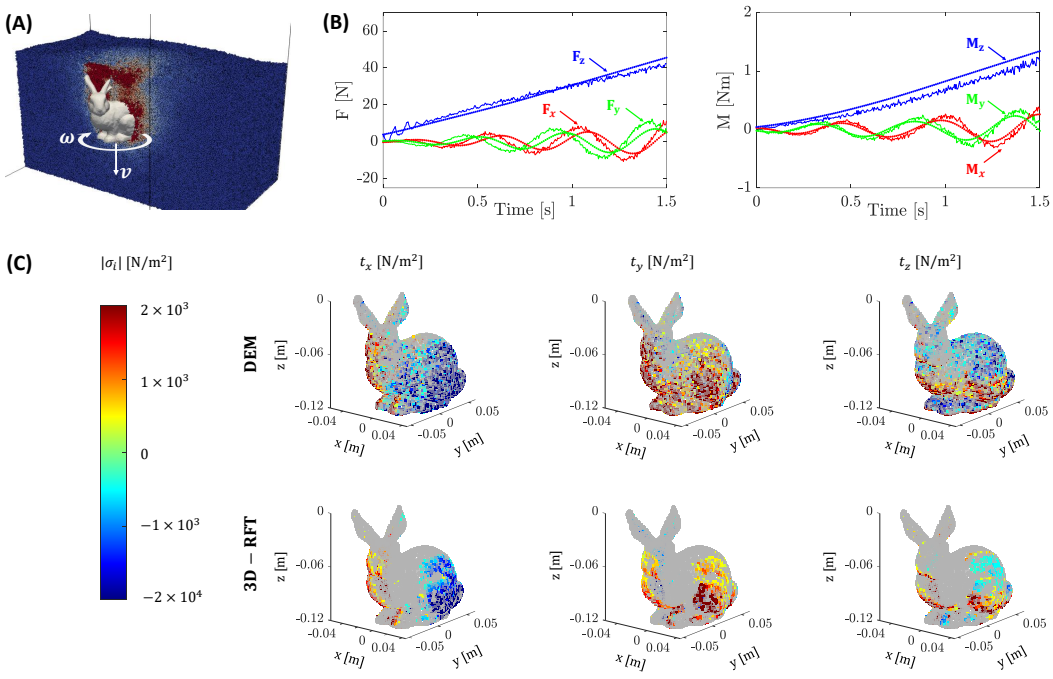

Figure 5-10: *DEM based 3D-RFT verification: Bunny drill*: *(A)* A snapshot of the Stanford-Bunny drill setup where a 10cm high stanford-bunny was simultaneously rotated ($\omega = 4\pi$rad/s, clockwise) and translated ($v = 0.1$m/s, downwards) along z-axis. The grains are colored with velocity magnitudes. The simulation domain consisted $\sim 2.1 \times 10^6$ particle (50/50 split of 3 mm and 3.4 mm diameter (d) grains) spread over $150d \times 150d \times 88d$ physical space. *(B)* Variation of net force (F, left) and moment (M, right) components (x: yellow, y: orange, and z: blue) from DEM (solid lines) and 3D-RFT (dotted lines). *(C)* Variation of various force commponets from DEM (Top) and 3D-RFT (Bottom) at a 6cm bunny-center-depth below the free surface. The DEM material properties are provided in table C.2 of the section C.6..

bed consists of approximately 2.1×10^6 particles spread over a $(150d \times 150d \times 88d)$ sized domain. The bunny shape was slightly modified from the standard shape — the shape was proportionally scaled in such a way that the bunny height measures 0.1 m, and the bunny base was flattened to make the base a plane surface without an inward extrusion. We find $I \approx 0.007$ and $Fr \approx 0.10$ ($L \approx 0.10\,\text{m}$, $\omega = 4\pi\,\text{rad/s}$, $v_{\text{intruder}} = 0.1\,\text{m/s}$) for this case. Thus, 3D-RFT is a valid approach for modeling this system. Figure 5-10 shows the simulation setup where the grains are colored with velocity magnitudes. Figure 5-10 also shows the variation of stresses over the intruder shape from DEM and 3D-RFT. All the reported components (net force and moments, as well as stress distributions) show a strong match between the two approaches.

5.11 Conclusion

3D-RFT is an important step towards developing a generic real-time modeling technique capable of modeling granular intrusion of arbitrarily shaped objects over a large range of low and high-speed scenarios in diverse materials and environments. Until this work, RFT has shown great potential to model the motion of arbitrary objects in the plane strain conditions at high and low speeds. We have proposed an extension of RFT to three dimensions in a fashion consistent with a continuum description of the material and symmetry constraints. The accuracy of the proposed 3D-RFT was demonstrated against a variety of full-field intrusion simulations, both continuum and DEM. The most immediate opportunity to expand 3D-RFT would be to combine 3D-RFT with Dynamic RFT [16] to build a high-speed three-dimensional RFT (3D-DRFT). Effects of multibody intrusions [125, 17], density variations [136], inertial and non-inertial velocity effects [128, 164, 16], cohesion [173], and inclines [174] on the resistive forces experienced by bodies intruding into granular volumes are among other aspects for further exploration toward the ultimate goal of a generic and fast granular intrusion modeling technique for potential use in modeling terradynamical motions[175], modeling granular impact system [41, 176], efficient locomotor designing [177] and many other similar applications. This work also presents a systematic approach towards developing reduced-order models in other similar systems with a combination of mathematical analysis and experiments/simulation-based data collection.

Chapter 6

Conclusion, impact, and future directions

6.1 Conclusion

In this thesis, we have worked on developing reduced-order modeling methods for modeling a variety of granular intrusion systems that are commonly seen in real-life situations. Such methods are of great interest in applications requiring limited information from granular intrusion systems. One of the biggest applications of such methods lies in the field of *terramechanics* for optimizing the locomotion of vehicles on off-road loose soil terrain on earth and beyond. To achieve this goal, we first explored the origins of granular resistive forces on rigid bodies intruding into the granular volumes as a function of the body, media, and their interaction properties. Once we understand these origins, we attempted to enhance pre-existing reduced-order approaches to model a large variety of granular intrusions.

To understand the origins of granular resistive forces, we used continuum modeling as our primary analysis tool. The continuum description of the granular volumes provided numerous advantages over the commonly used particle modeling approach(DEM) for developing reduced-order models. First, the continuum approach provided a computationally cheaper alternative to DEM, which was useful for generating a large amount of reference data and thereby developing an empirical understanding of such systems. Second, the method provided a meso-scale characterization of the systems instead of a micro-scale characterization that DEM provides. This meso-scale characterization was more useful than micro-scale characterization for developing macro-scale reduced-order methods. And last, though granular constitutive models were limited by the amount of physics included in their functional forms, the shortcoming worked to our advantage in understanding systems physics. Fine control over the ingredients of the constitutive laws provided us with a systematic approach

for correlating the constitutive law ingredients with the physical phenomena at hand. And thus, separating the origins of forces became easier.

Drawing from the cases we study in this thesis, we concluded that when applied with appropriate implementation methods, continuum modeling can model a large variety of granular intrusion problems with fairly simple and basic constitutive models. We published these results in the form of journal publications for the granular community, which can greatly benefit from a larger adoption of the continuum modeling approach for modeling granular media. We also hope that the Matlab-based applications developed in this thesis help new researchers get started with this approach. No doubt, there are limitations to what continuum modeling can model due to its continuum representation of discrete grains and its dependence on the sufficiency of physics included in constitutive models to capture the phenomenon at hand. Thus, an in-depth analysis of the systems, before modeling them with this approach, is indeed quintessential for its use in an application. Advanced methods such as hybrid DEM-continuum models, two-phase models, etc., should be used if the system dynamics demands it.

We build upon the insights we gain from continuum approaches and modify an existing empirical approach, 2D-RFT, for modeling various granular intrusions in nearly real-time. We develop two enhanced versions of RFT, namely 2D-Dynamic RFT, which enables the use of 2D-RFT in high-speed intrusions, and 3D-RFT, which extends 2D-RFT to three dimensions, a crucial step in improving the adoption of RFT to in real-life applications. With multiple verifications against results from literature, experiments, and continuum and DEM simulations, we verify the accuracy of these forms and find an excellent match between the predictions and reference results.

6.2 Impact

This thesis work has led to follwing journal publications which the readers can refer for more details:

[1] **Agarwal, Shashank**, Carmine Senatore, Tingnan Zhang, Mark Kingsbury, Karl Iagnemma, Daniel I. Goldman, and Ken Kamrin. "Modeling of the interaction of rigid wheels with dry granular media." Journal of Terramechanics 85 (2019): 1-14.

[2] Schiebel, Perrin E., Henry C. Astley, Jennifer M. Rieser, **Shashank Agarwal**, Christian Hubicki, Alex M. Hubbard, Kelimar Diaz, Joseph R. Mendelson III, Ken Kamrin, and Daniel I. Goldman. "Mitigating memory effects during undulatory lo-

comotion on hysteretic materials." Elife 9 (2020): e51412.

[3] **Agarwal, Shashank**, Andras Karsai, Daniel I. Goldman, and Ken Kamrin. "Efficacy of simple continuum models for diverse granular intrusions." Soft Matter 17, no. 30 (2021): 7196-7209.

[4] **Agarwal, Shashank**, Andras Karsai, Daniel I. Goldman, and Ken Kamrin. "Surprising simplicity in the modeling of dynamic granular intrusion." Science Advances 7, no. 17 (2021): eabe0631.

[5] **Agarwal, Shashank**, Daniel I. Goldman, and Ken Kamrin. "Towards real-time modeling of arbitrary three-dimensional granular intrusion " (In preparation, Chapter 5)

6.3 Future directions

Though our work has advanced RFT, numerous avenues remain to be explored for reaching the ultimate goal of developing an all-terrain, all-speed, generic RFT. We discuss a few essential avenues in this regard next:

1. **3D Dynamic RFT:** As discussed in chapter 5's conclusion, this is the immediate step in RFT extension. DRFT and 3D-RFT, proposed in this work, could be combined to develop a three dimensional dynamic resistive force theory (3D-DRFT) for three-dimensional high-speed intrusions.

2. **Dynamic inertial correction in DRFT:** DRFT leaves the $O(1)$ dynamic inertial correction prefactor to be determined on a case-to-case basis using pre-existing data, rather than providing an exact functional form for it. Many studies in the past have explored such prefactors during vertical intrusions with a variety of intruder shapes, but none have given a generic form of $O(1)$ prefactor. A characterization of this inertial prefactor for various shapes and directions would be of great value to the community besides improving DRFT form.

3. **Shadowing effects and multibody intrusions:** Section 2.4.2 of Chapter 2 briefly touches upon the effects of multibody intrusions on resistive forces experienced by intruders. We observe that the presence of other bodies in a granular volume generally restricts the media flow, increasing the resistive forces on intruders. But the length scales and magnitudes of these increments remain to be characterized. Additionally, the shadowing effect, a reduction in forces experienced by a surface due to the presence of another co-moving surface ahead

of it, also remains weakly explored. A detailed investigating of these topics could greatly improve RFT. Besides, both the topics have their independent applications in decreasing/increasing tractions on granular intruders/anchors.

4. **RFTs for density sensitive materials:** Section 2.4.3 of Chapter 2 briefly touches upon the effects of density variations on granular resistive forces. The current RFTs assume a constant media state in granular volume which may not be true in many natural terrains. In this regard, a detailed study on characterizing the role of variable media density on resistive forces over time and space would be very interesting and useful for RFT. These effects could also add system-dependent length scales (as seen in Section 2.4.3) to RFT, which is missing in its current forms.

5. **RFTs for cohesive materials:** Cohesion remains the least explored but another major limitation of RFT. The current forms of RFTs are limited to non-cohesive granular volumes, but the naturally occurring terrains such as mud and snow often show cohesion. The *terramechanical* models in this regard outperform RFTs and work for other classes of materials such as snow and mud. Exploring the existence of RFTs in cohesive granular volumes would also be very useful.

6. **RFTs for inclines:** Similar to cohesion-less and constant density assumptions, RFTs also assume granular intrusions to occur near flat granular surfaces where the material slopes are insignificant. Characterizing the effects of incline angles on RFTs and changes required to enable it to model motion on inclines (possibly by changes in effective depths) would also be another vital addition to RFTs.

7. **RFTs for flexible intruders:** With increasing advancements in the field of soft robotics, it would be exciting to see the performance of RFT in modeling flexible intruders in granular volumes and what strategies could be adopted to incorporate intruder elasticity in RFT implementations.

Final thoughts

RFT presents a beautiful example of the simplicities hiding behind the complexities of diverse natural systems. We hope our extensive work on developing better versions of RFTs and the existence of numerous opportunities to expand them will motivate future researchers to work on expanding its capabilities. We also hope that the methods and techniques developed in this thesis will be useful for future researchers in carrying out their research and systematically developing reduced-order models in granular and other media.

Appendix A

Additional resources on continuum modeling of granular intruions in Chapter 2

A.1 Movies for visualizing intrusion studies

In addition to the figures shown in this chapter, readers can refer to movies showing the variation of various system variables across granular intrusion domains from the link below. A representative image of each movie is provided below.
`https://pubs.rsc.org/en/content/articlelanding/2021/SM/d1sm00130b`.

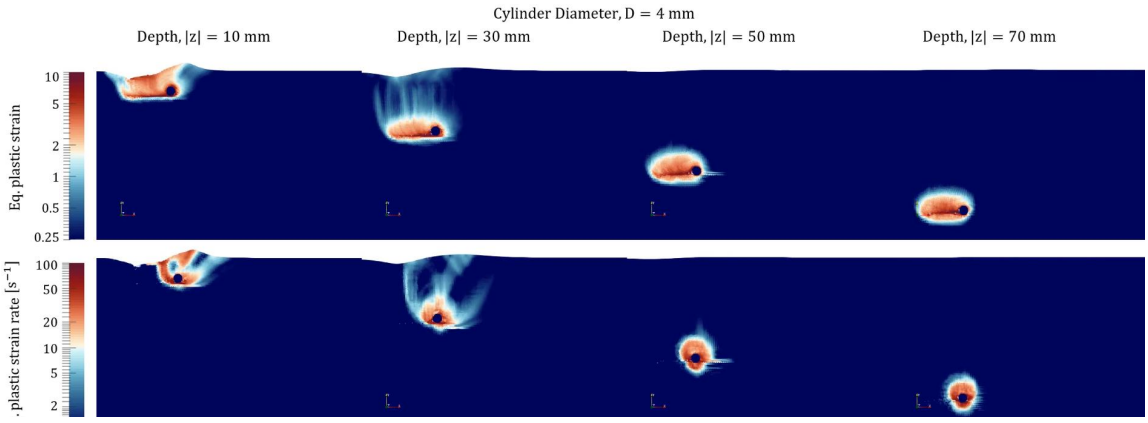

Movie S1: Variation of equivalent plastic strain and equivalent plastic strain rates over time for cylinders at depths |z| of [10,30,50,70] mm left to right. Cylinder had a diameter of 4 mm and other material properties are provided in section 2.4.1

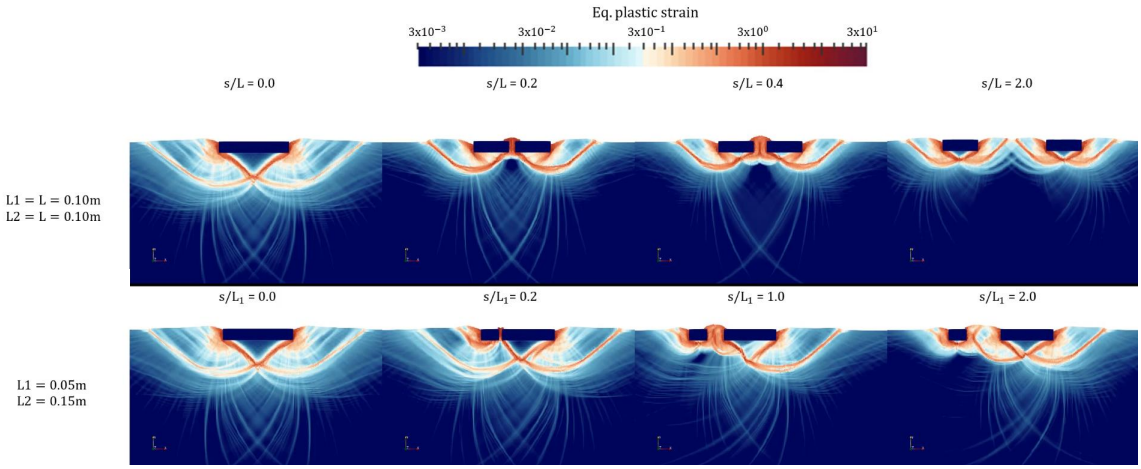

Movie S2: Variation of equivalent plastic strain over time during two-plate granular intrusions for equal plates ($L = 0.1$ m, top) and unequal plates ($L_1 = 0.05$ m and $L_2 = 0.15$ m, bottom) at multiple plate separations. The separation values are mentioned in the movie. Other material properties are provided in section 2.4.2

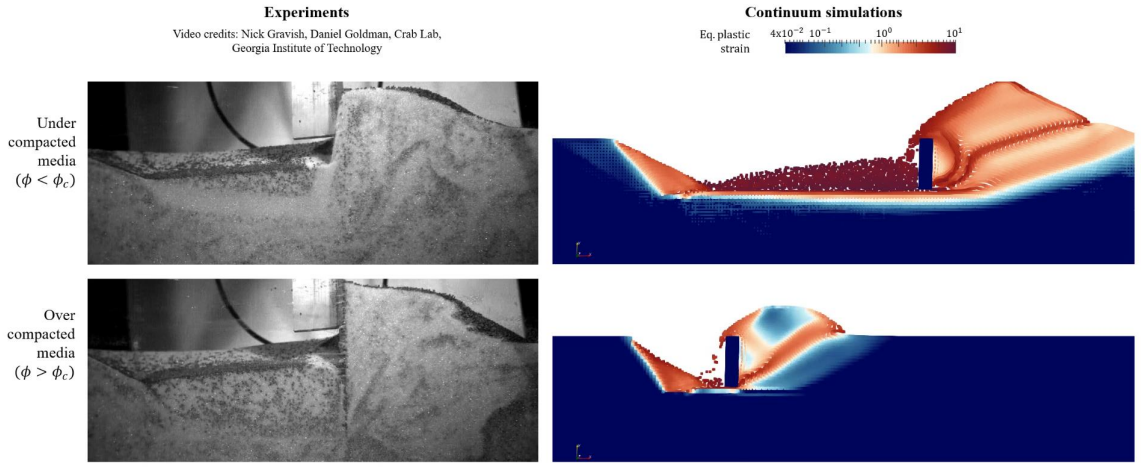

Movie S3: Material flow encountered during plowing of granular media in experiments (left) and simulations (right) in under-compacted (top) and over-compacted (botom) media. The flows clearly show continuous and descret formation of shear flow zones in under- and over-compacted media. More details of simulations and experiments are provided in section 2.4.3

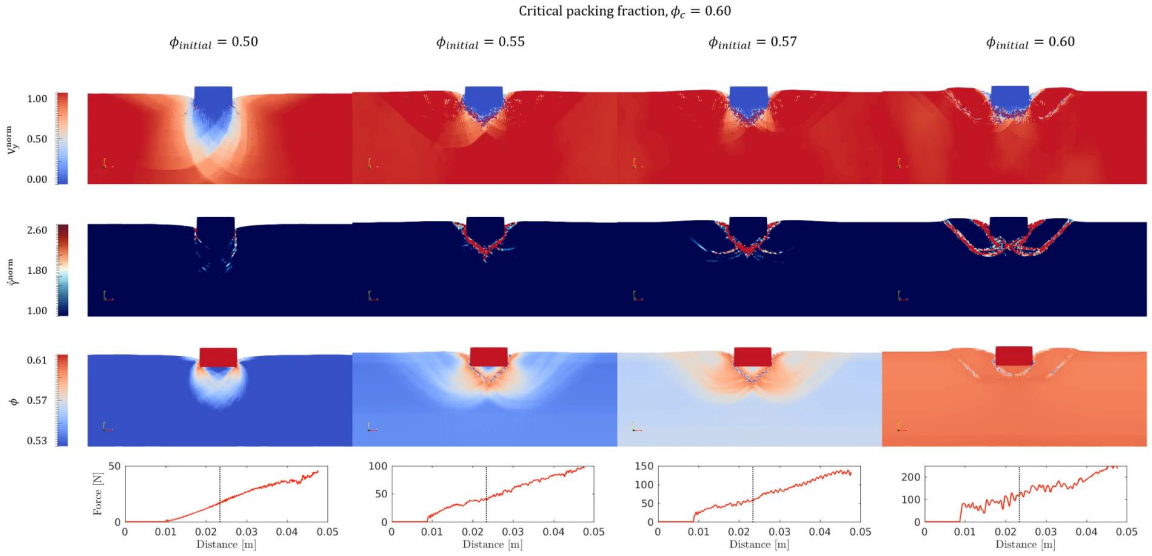

Movie S4: Variations of vertical components of velocities, equivalent plastic strain rate, packing fraction in granular volume, and net upward force on intruder at various initial packing fractions ($\psi_{initial}$) in a material with $\psi_c = 0.60$ over time. Other material properties are identical across four simulations and are provided in section 2.4.4

A.2 Open source app for continuum modeling

We also developed an open-source, Matlab-based implementation of NDPM with continuum modeling as a part of this work. The implementation models various arbitrary granular intrusions and granular flows imported as images in the Matlab-based interactive app. Figure A-1 shows a snapshot of the app interface. The app allows for constrained as well as free intrusion scenarios. A link to download the application is provided below. Readers can find more details at the provided link.

https://www.mathworks.com/matlabcentral/fileexchange/75928-granular-intrusion-continuum-modeling-matlab-2018a?s_tid=srchtitle

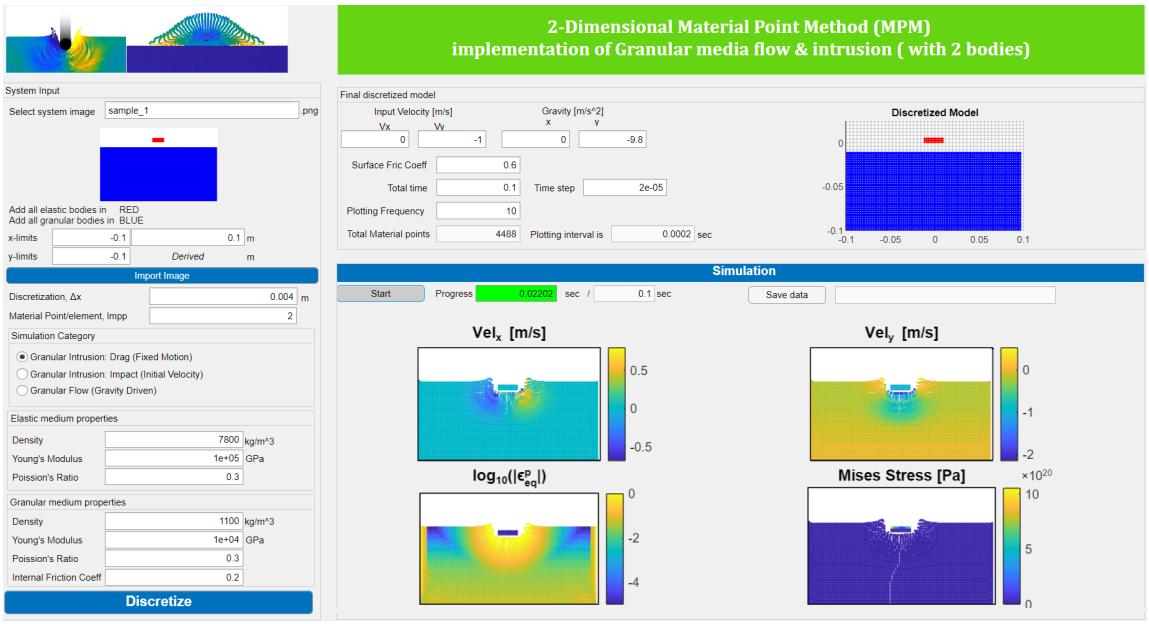

Figure A-1: Interface of Matlab based Continuum modeling application for modeling arbitrary intrusions of arbitrary shaped bodies. The app also allows modeling granular in variety of granular flow situations. The app-interface allows for inputing system details in form of image files and uses implementation discussed in Dunatunga and Kamrin [108]

Appendix B

Supplementary Information on DRFT

B.1 Verification of DRFT in a dynamic inertial correction dominated scenario

To further verify the robustness of DRFT, we simulate a smaller version of the grousered wheel with continuum modeling as well as DRFT. Doing so also demonstrates the use of scaling analysis in characterizing the free surface profiles for any given class of intruders, using grousered wheels as the test case. The new wheel is similar in shape and composition to the one used in the original study (details in Table 4.1) but is halved in its spatial dimensions. The granular media is kept the same. The shape and other dimensionless variables $\{\rho_{wheel}/\rho_c, \mu_s, h_g/D, N\}$ are kept the same between the two wheels, and hence we assume that the free surface function ψ takes the same form as the reference case for the larger wheel, $\psi = r\omega^2/g$. With this, we can perform DRFT to predict the dynamics of the small wheel.

We plot the results from the earlier larger wheel case (in blue) as well as the new scaled-down wheel case results (in black) in Figure S1. We use continuum modeling for verifying the accuracy of the results. The new wheel data from DRFT (black dashed lines with '$\times$' markers) matches the reference continuum solution with good accuracy, verifying the robustness of DRFT.

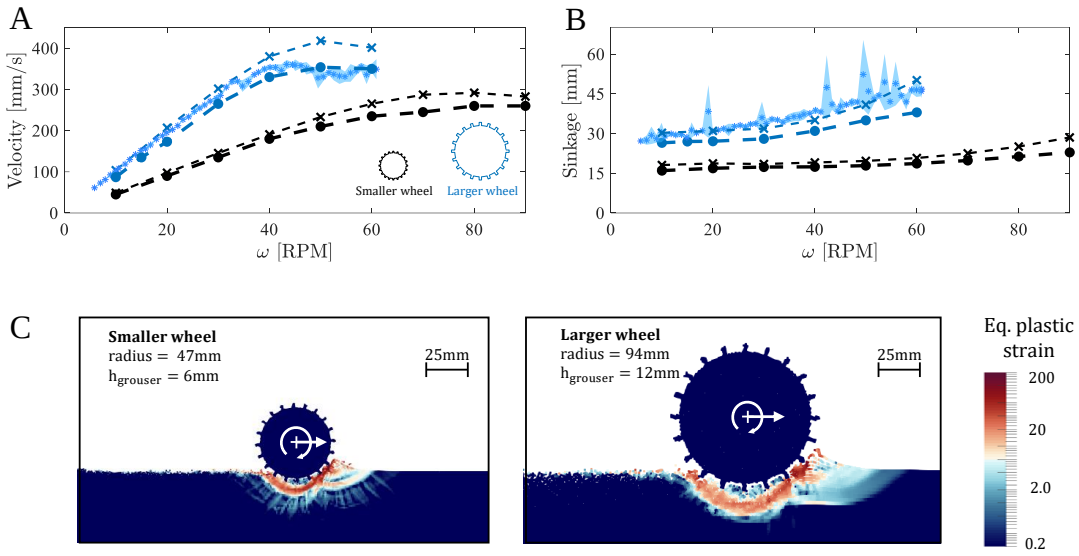

Figure B-1: **DRFT performance check for wheels of different dimensions**: Variation of (A) Translation velocity, and (B) Sinkage from experiments (blue data with $*$ markers), continuum modeling (thin dashed line with filled $\bullet$ markers) and DRFT modeling (thick dashed line with $\times$ markers) with respect to angular velocity, ω. Two differently sized wheels are used. The blue color represents the data corresponding to the wheel used in the original study, and the black color corresponds to the data from the new smaller wheel. (C) and (D) show the spatial variation of equivalent plastic strain rate in smaller and larger wheel cases at 90 and 60 RPM resp.

B.2 Theoretical derivation of expected linearity between angular and translation velocity from quasistatic RFT

In the following analysis, we present a general proof of linearity between the steady-state translation and the angular velocities for round bodies undergoing free locomotion based on quasistatic RFT. For a rigid body (with fixed mass and shape), if there exists a quasistatic RFT solution with steady-state (V_{cm}, ω_{cm}), then there exists another steady-state solution $(\lambda V_{cm}, \lambda\omega_{cm})$ for any value of λ, having the same sinkage, $|z|$.

Proof: As per quasistatic RFT, the resistive force per area on any subsurface element of the body can be given as, $\mathbf{t} = \mathbf{t}(\beta, \gamma, z)$, where β represents the orientation of the subsurface, γ represents the local velocity direction of the subsurface, and $|z|$ is subsurface depth. Thus, every subsurface experiences a resistive force as a function

of its position, orientation, and velocity direction. At a steady-state, the sum of these forces in the horizontal direction equals zero, and in the vertical direction, the sum balances the weight of the locomoting body. Any change in the velocity magnitude is not expected to change these forces since the resistive forces have no dependence on the magnitude of the velocity, only the direction. A multiplicative increase/decrease in the translational and angular velocity of the wheel by the same constant factor (λ) will not affect the velocity direction at any subsurface of the body for a given orientation. i.e. $\gamma_{new} = \gamma_{old}$ for any subsurface at a given orientation. Thus, at a given sinkage and orientation, the forces on any subsurface do not change for any value of λ, leading to no variation in the net force on the locomoting body. Thus, because the forces at any orientation in state (V_{cm}, ω_{cm}) result in a steady-state, forces at any orientation in state $(\lambda V_{cm}, \lambda\omega_{cm})$ will also result in a steady-state.

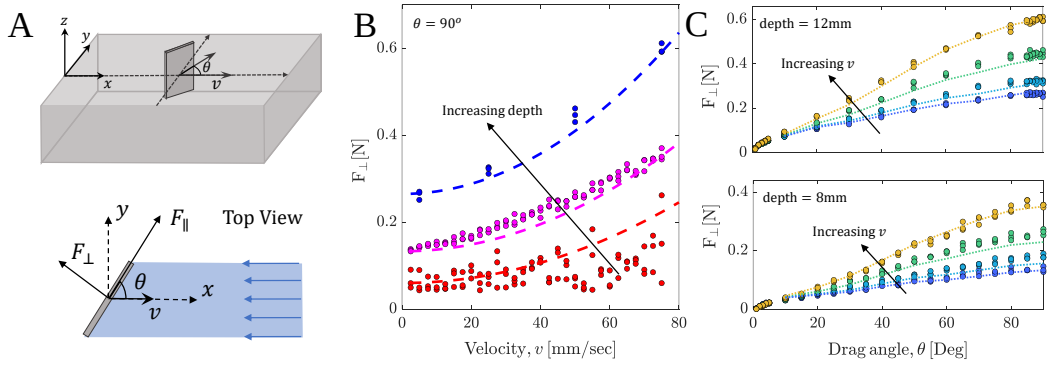

Figure B-2: **DRFT in horizontal intrusion of plates at different oblique angles:** *(A)* Schematic of intrusion scenarios. Experiments (from [165]) use a 30×30 mm^2 thin rigid plate moving with speed v partially-submerged to different depths in a dry granular media of effective bulk density, $\rho = 1450$kg/m^3 ($\rho_g = 2500$ kg/m^3; ϕ=0.58). The plate is rotated to an angle θ with respect to the velocity direction in the xy (horizontal) plane. *(B)-(C)* Comparisons of experimental measurements of the normal drag component compared to results of the "static-plus-ρv^2" drag model, $t_n = t_{\text{static}}(\theta)H(-z)|z| + \lambda\rho v_n^2$, where t_n and v_n are the normal components of the force-per-area and velocity, respectively. We use $\lambda = 1.1$ in all the fittings in this figure and extract $t_{\text{static}}(\theta)$ from the lowest-speed experimental data. *(B)* Experimental data (colored circles) and model results (dashed lines) for normal drag force on plates at a constant angle $\theta = 90^o$ for three depths ($[6, 8, 12]$ mm, measured from free-surface to plate bottom). Black arrows show the direction of increasing depths. *(C)* Experimental data (filled circle) and model results (dashed lines) for normal drag force on plates with velocities $[50, 250, 500, 750]$ mm/s (shown by different colors) at various θ and two depths ($[8, 12]$ mm). Black arrows show the direction of increasing velocities at each depth.

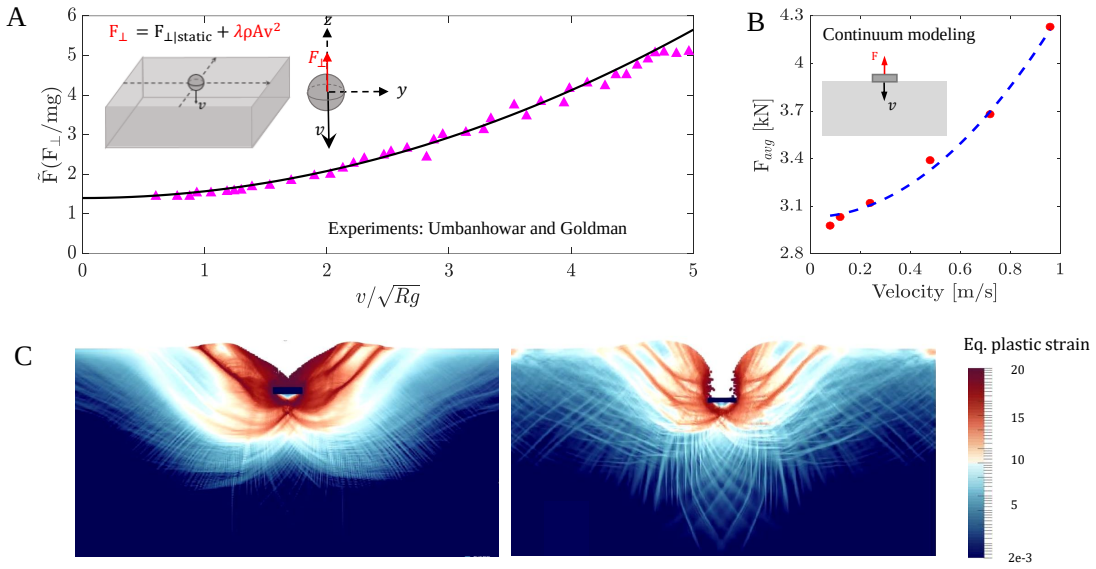

Figure B-3: **DRFT in downward intrusion:** *(A)* Schematic and normalised force variation for vertical intrusion based on Umbanhowar and Goldman [161] sphere intrusion data at critical state packing fraction (at a fixed depth). Umbanhowar and Goldman generated this data by measuring the acceleration of spheres impacting the granular beds at fixed depths being impacted at various different initial velocities. Triangles (pink) represent experimental data, and solid line (black) represents the $\lambda\rho v^2$ fit to the data. We find $\lambda = 1.4$ to be an appropriate value. *(B)* Data (red circles) and *(C)* visualization of equivalent 2D plane-strain continuum simulations for vertical plate intrusions at low-speed (left) and high-speed (right). The continuum data in *(B)* can be qualitatively compared to experiments in *(A)* but not quantitatively because the two utilize different intruder shapes and out-of-plane conditions. For *(B)* 0.16 m plates were intruded in a granular volume of density 2500 kg/m^3 and internal friction $\mu = 0.62$; $\lambda = 2.8$ was used for DRFT fittings (blue dotted lines). The MPM plots in *(C)* visualize the material flow field around the intruding body. These results indicate the dominance of the dynamic inertial correction in the drag forces. The reason is that similar to horizontal plate intrusions, which in the plane-strain approximation often have only one bulk flow region (creating a Coulomb-wedge structure [94]), the vertical plate intrusions also create two non-interacting bulk flow regions to either side. The free surface regions where flow trajectories emanating terminate remain at the same height on both sides, in both the low and high-speed intrusions. Thus, the resistive force response encounters minimal contribution from dynamic structural correction; the dynamic inertial correction dominates.

This analysis holds only when the long-time motion of the locomotor is truly

steady — for example, a non-round wheel has a (wobbly) limit cycle as its long-time behavior but not a steady state. In the latter case, the analysis still approximately holds if the velocity variations of the wheel do not result in accelerations comparable to g. Accelerations of the order of g add a new timescale to the problem, completely changing the problem's dynamics. Similarly, linearity in the locomoting body can break down if the characteristic time scale associated with a flexible body is comparable to the characteristic time scale $\sqrt{L/g}$. The above hypothesis is also bound to fail if any contributions used in modeling the system are dependent on the velocity magnitude.

B.3 Momentum balance approach for granular intrusion

The essential reason that a velocity-squared additive pressure contribution seems a sensible way to account for macro-inertia can be understood through analysis of the momentum balance equations. In a reference frame moving with an intruder, balance of momentum at steady state is expressed as

$$0 = \rho g_i + \sum_{j=1}^{3} \frac{\partial}{\partial x_j} \big(\sigma_{ij}(\mathbf{x}) - \rho v_i(\mathbf{x}) v_j(\mathbf{x}) \big). \tag{S1}$$

Consider a reference case in the quasistatic limit, having slow intruder velocity, V_i^R, in the lab frame. Let $\sigma_{ij}^R(\mathbf{x})$ and $v_i^R(\mathbf{x})$ represent the corresponding quasistatic stress and flow solutions in the intruder frame. Thus,

$$0 = \rho g_i + \sum_{j=1}^{3} \frac{\partial}{\partial x_j} \sigma_{ij}^R(\mathbf{x}). \tag{S2}$$

Let us suppose the velocity of the intruder is scaled up to a non-negligible value $V_i = C\, V_i^R$, causing the resultant flow field to exit the quasistatic limit. Consider the candidate intruder-frame flow field $v_i(\mathbf{x}) = C v_i^R(\mathbf{x})$ and stress field $\sigma_{ij}(\mathbf{x}) = \sigma_{ij}^R(\mathbf{x}) + \rho(v_i(\mathbf{x}) v_j(\mathbf{x}) - V_i V_j)$. The proposed flow field assumes similarity of flow between slow and high-speed cases, and the stress field properly reduces to the quasistatic solution when C is small. If we suppose the far-field flow vanishes in the lab frame, these candidate fields comprise a valid solution in that they necessarily satisfy equation S1, by design, while preserving the far-field stress condition from σ_{ij}^R. Also, kinematic constraints such as incompressibility are guaranteed to transfer from the quasistatic solution to the high-speed solution. In the intruder frame, the velocity field vanishes at the leading intruder-grain interface, so evaluating the stress at a point $\mathbf{x}^I$ on the

intruder interface gives $\sigma_{ij}(\mathbf{x}^I) = \sigma^R_{ij}(\mathbf{x}^I) - \rho V_i V_j$. It can thus be seen that, under the assumptions made herein, the presence of macro-inertia adds an extra pressure at the intruder-grain interface that goes as density times intruder-velocity squared.

We emphasize the approximate nature of this analysis. First, even if $\{\sigma^R_{ij}, v^R_i\}$ exactly satisfies the frictional-plastic constitutive relation, the proposed solution $\{\sigma_{ij}, v_i\}$ may not. In the main text, we add an additional order-one factor of λ ahead of the ρv^2 term to account for deviations caused by this potential mismatch. Also, importantly, this analysis has assumed the fast flow is a scaled version of the slow flow, which can be an overreaching approximation, particularly in cases where dynamic structural corrections modify the granular geometry.

B.4 Movies for better understanding high-speed locomotions

In addition to the figures shown in this chapter, readers can refer to movies showing high and low-speed locomotion in a variety of cases using experiments and continuum simulations from the following link.
`https://www.science.org/doi/10.1126/sciadv.abe0631`.

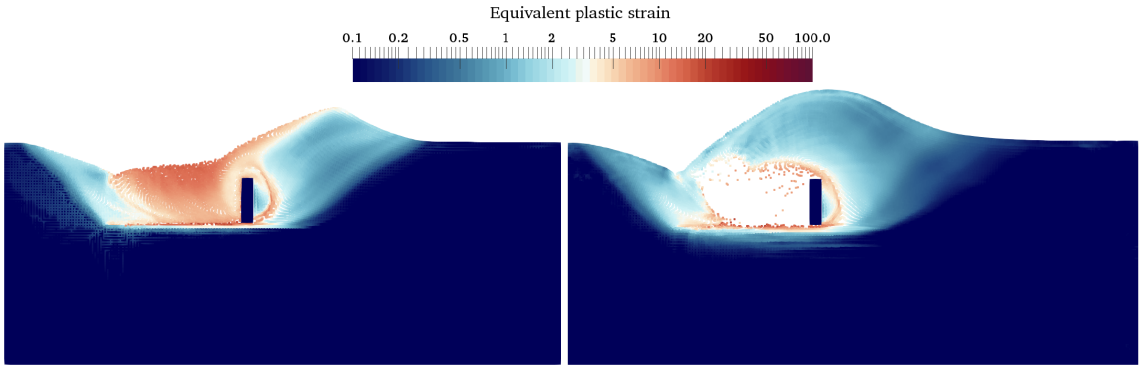

Movie S1: Variation of equivalent plastic strain in 2D plane-strain continuum simulations for horizontal plate intrusion at both low (0.04 m/s, left) and high speeds (0.64 m/s, right). The videos show that the material flow profile (a Coulomb-wedge structure) ahead of the intruding plates, where most of the drag originates, does not change between low and high-speed intrusions. As a result, the free surface height, the material flow geometry, and the shape around the intruders remain similar regardless of intrusion rate. Thus, the resistive force response encounters minimal contribution from the dynamic structural correction, and the speed dependence is dominated by the dynamic inertial correction.

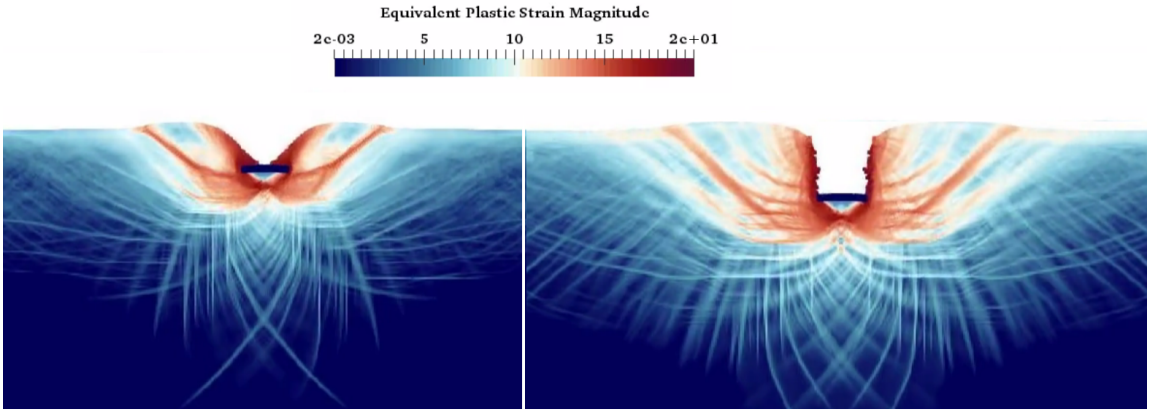

Movie S2: Variation of equivalent plastic strain in 2D plane-strain continuum simulations for vertical plate intrusion at low-speed (left) and high-speed (right). The videos show that similar to horizontal intrusions, two independent Coulomb-wedge type structures are formed during the vertical intrusion of plates. The free surface height, the material flow geometry, and the shape around the intruders remain similar regardless of intrusion rate. Thus, the resistive force response encounters minimal contribution from the dynamic structural correction, but has a significant dynamic inertial correction.

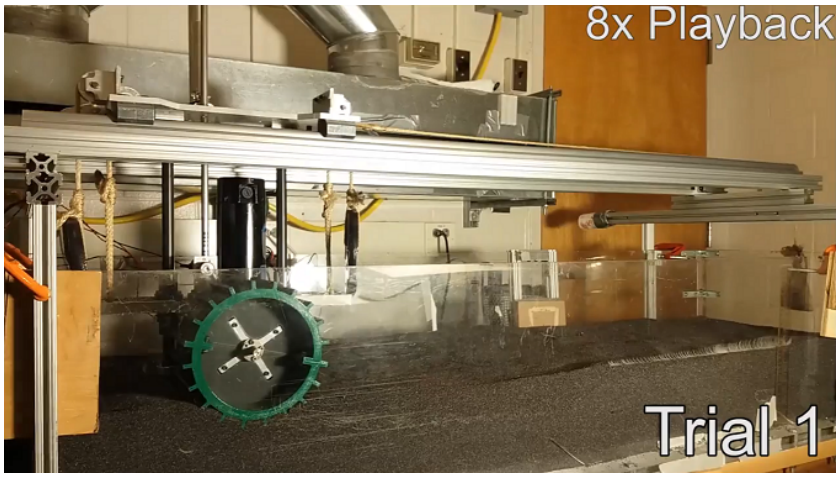

Movie S3: Sample experimental runs of free wheel locomotion: Lateral motion of the wheel is restricted with a double rail and bearing system. The granular material is reset to a loose packing state at the beginning of each trial by air fluidization of the granular bed. The details of the setup, along with the Grousered wheel and the granular media used in the experiments, are provided in section 4.2, Table 4.1, and Table 4.2. Photo Credit: Andras Karsai, Crab Lab, Georgia Institute of Technology.

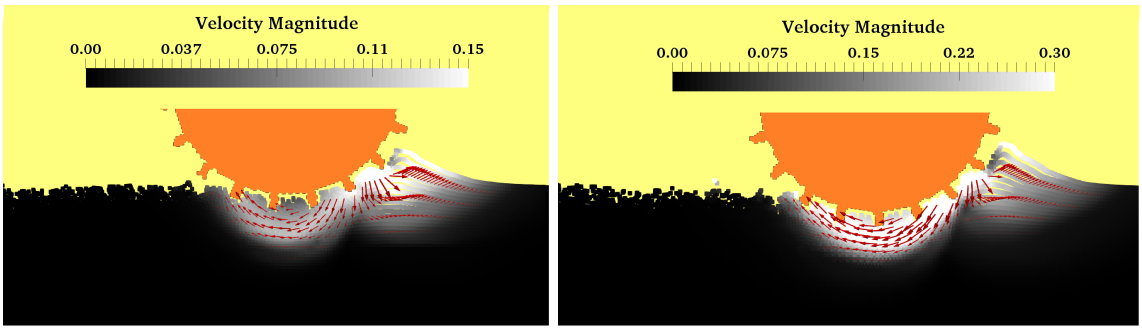

Movie S4: Visualization of material flow using continuum modeling at 30 RPM and 60 RPM wheel locomotion: The color bars indicate the variation of velocity magnitude in the granular media domain. The material flow clearly indicates an increase in the size of the flow zone with increasing rotation rates.

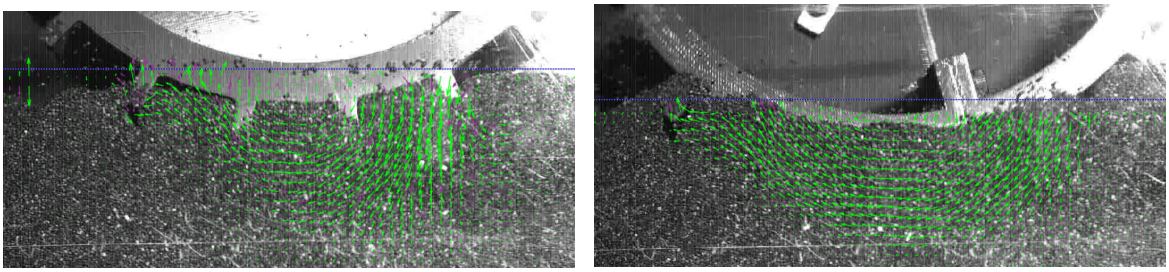

Movie S5: A PIV visualization of 30 RPM (left) and 60 RPM (right) wheel locomotion experiment. The movies show similar flows to continuum modeling movie. Additionally, an increasing flow zone size with increasing rotation rate (30 to 60 RPM), similar to those observed in the continuum modeling (Movie S4), are observed in experiments. Photo Credit: Andras Karsai, Crab Lab, Georgia Institute of Technology.

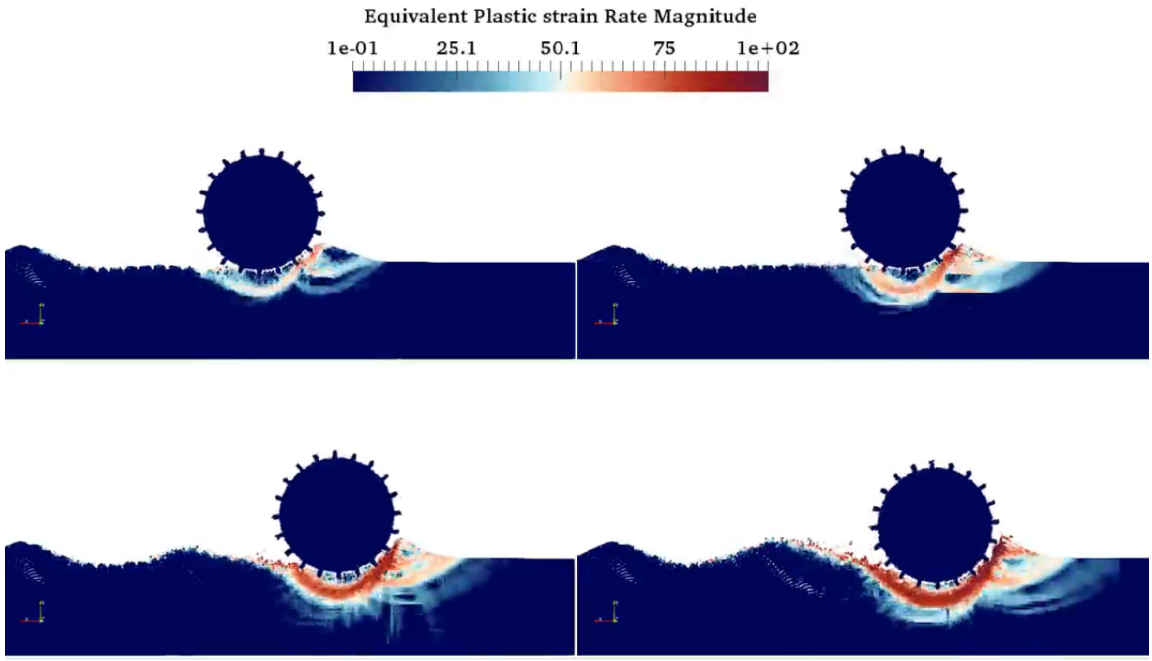

Movie S7: Visualization of material flow during wheel locomotion at [10,30,60,90] RPM. We plot equivalent plastic strain rate from continuum modeling, a scalar measure of the size of plastic strain. For a better visualization, all the wheels start at the same rotation rate of 30 RPM in the beginning of the simulations and switch to [10,30,60,90] RPM after a fixed finite horizontal motion, which is synchronized to be the beginning of the video.

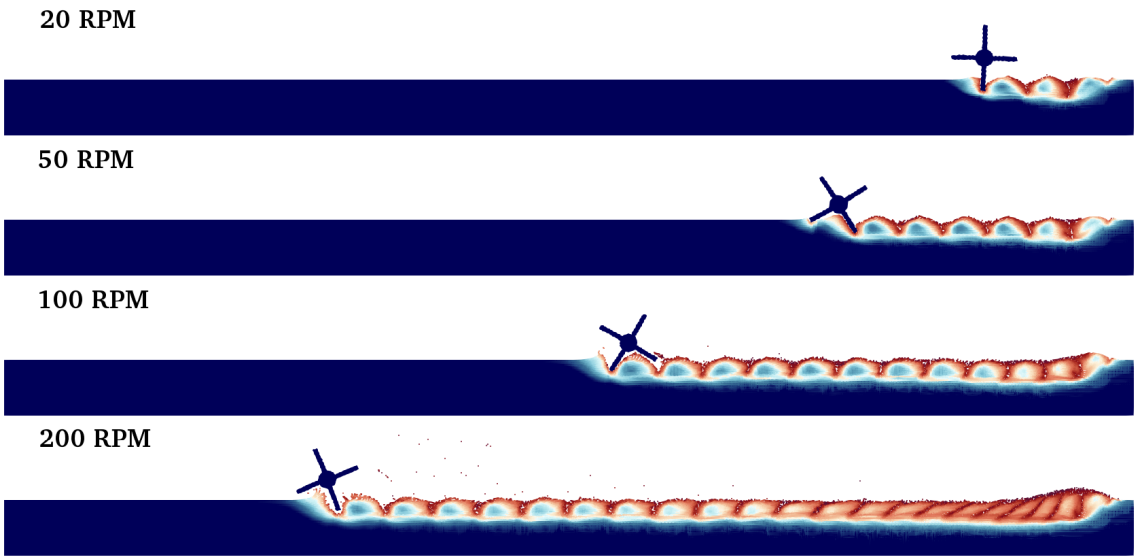

Movie S8: Visualization of material flow during 4-flap runner locomotion at [20,50,100,200] RPM. We plot equivalent plastic strain from the continuum model, a scalar measure of the size of plastic strain. As expected, the flowing regions are separated by flap intrusions and thus do not interact enough to cause an effective free surface change for the material trajectories. Thus, only a dynamic inertial update was used in the DRFT modeling of this case.

Appendix C

Supporting Information on 3D-RFT

C.1 Evaluation of quasi-static conditions in a system for deciding the applicability of 3D-RFT in it

We use following definitions of inertial number (I) and Froude number (Fr) for evaluating applicability of 3D-RFT in modeling granular resistive forces in a system.

$$I = \dot{\gamma}/\sqrt{P/\rho_g d^2}) \qquad Fr = v/\sqrt{gL}$$

where $\dot{\gamma}$ represents the shear rate, P represents hydro-static pressure, ρ_g represents the material grain density, d represents the material grain diameter, v represents the characteristic velocity, L represents the characteristic length, and g represents acceleration due to gravity in a granular system. If a system has both the angular and translational velocities, v is taken as $v = \max(v_{\text{intruder}}, L\omega/2\pi)$, where v_{intruder} and ω represent the intruder translation and rotation speeds, respectively.
We approximate $\dot{\gamma} = v/L$ and $P = \rho_c g L$. Where ρ_c represents the critical material density in the medium. We get following approximations for I and Fr using these definitions:

$$I = (v/L)/\sqrt{(\rho_c g L)/\rho_g d^2} = \sqrt{\frac{v^2 \rho_g d^2}{\rho_c g L^3}} \approx \sqrt{\frac{v^2 d^2}{g L^3}}$$
$$Fr = v/\sqrt{gL} \qquad v = \max(v_{\text{intruder}}, L\omega/2\pi)$$

We recommend an upper limit of 0.1 on I and an upper limit of 0.4 on Fr. While the former condition avoids the collision (micro-inertial) character of granular flows [178], the latter avoids intrusions with significant macro-inertial effects in granular

volumes that cannot be captured by proposed 3D-RFT. The later suggestion is based on the work of Agarwal et al. [16], who observed in-significant macro-inertial effects in granular locomotions at $\omega/\omega_0 < 0.4$ where the ratio ω/ω_0 represents the Froude number (Fr) as $\omega/\omega_0 = (2\pi v/L)/(2\pi\sqrt{L/g}) = v/\sqrt{gL}$. This limit is also inline with the work of Sunday et al. [179] who observed depth-dependent quasi-static forces to dominate over inertial forces, during granular intrusions at $Fr < 1.5$.

C.2 Internal friction (μ_{int}) dependence of 3D-RFT

We explore the dependence of 3D-RFT forces on material internal friction by conducting plate intrusions simulations for five different values of (μ_{int}) at two values of surface friction (μ_{surf}) each (except $\mu_{\text{int}} = 0.4$ for which we explore 3 values of (μ_{surf})). To better understand the trends in variations of $\boldsymbol{\alpha}$, we only consider normal component of $\boldsymbol{\alpha}$ i.e. $\boldsymbol{\alpha}_n$. Figure C-1 shows scaled values of $\boldsymbol{\alpha}_n$ scaled by the scaling coefficient ξ_n. These plots also conclude that ξ_n primarily depends on μ_{int} (in addition to its linear dependence of ρ_c and g, $\xi_n = \rho_c g \hat{f}(\mu_{\text{int}})$). Thus, figure C-2 shows the variation of $\xi_n/\rho_c g$ with μ_{int}. This figure uses two additional values of μ_{int}— 0.1 and 0.2. We conducted additional simulations at limited μ_{surf} and ψ for these μ_{int}'s for better understandings the ξ_n vs μ_{int} trends, as discussed in Materials and Methods section. We find superlinear dependence of ξ_n on μ_{int} which was also observed by researchers [77] in the past. Figure C-2 can be used for interpreting the value of ξ_n from ρ_c, , and μ_{int} (or angle of repose, $\theta = \tan^{-1}(\mu_{\text{int}})$) of a non-cohesive granular media. Exact values of ξ_n and μ_{int} corresponding to figure C-2 are given in table C.1.

Table C.1: Variation of ξ_n with μ_{int} at $\rho_c = 3000\,\text{kg/m}^3$

μ_{int}	$\theta_{\text{repose}}[^o]$	$\xi_n[\times 10^6\,\text{N/m}^3]$
0.0	0^o	0.0
0.1	5.7^o	0.13
0.2	11.3^o	0.28
0.3	16.7^o	0.51
0.4	21.8^o	0.92
0.5	26.5^o	1.58
0.7	35.0^o	5.32
0.9	42.0^o	12.32

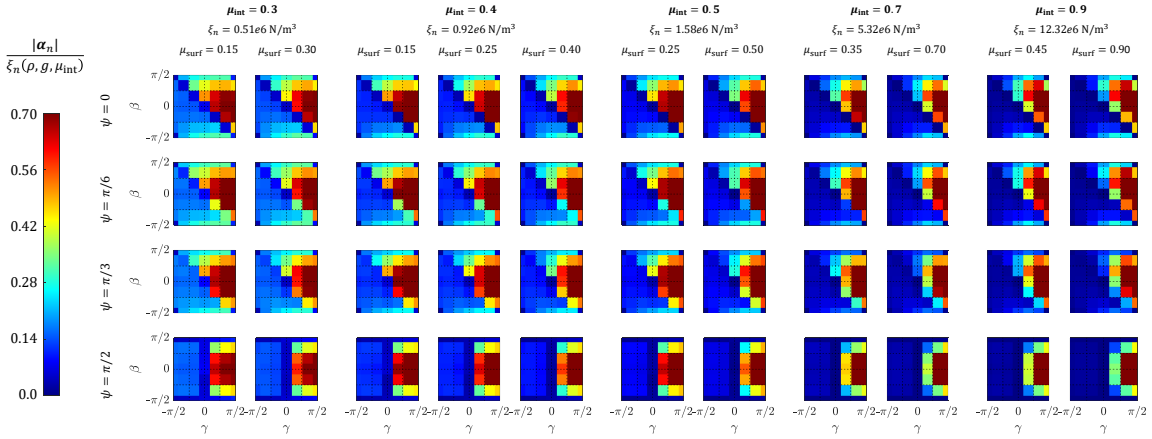

Figure C-1: *Variation of $\boldsymbol{\alpha}_n$ with μ_{int}*: Variation of normal component of stress/depth (scaled by ξ_n) for various combinations of μ_{int} and μ_{surf}. The variations of normalized ξ_n with μ_{int} are plotted in figure C-2. Corresponding values of μ_{int}, μ_{surf}, and ξ_n are written at the top of each column. The granular material had an effective density of (ρ_c) 3000 kg/m^3 in the cases.

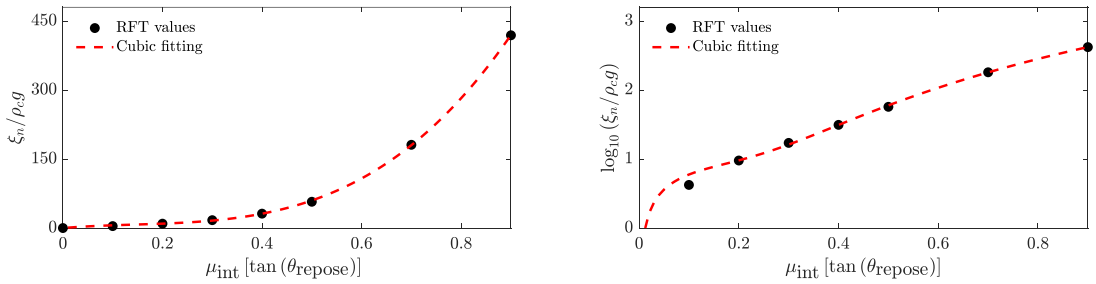

Figure C-2: *Variation of ξ_n with material properties*: Variation of normalized scaling coefficient ξ_n (normalized with density ρ_c and gravity g) with material internal coefficient of friction (μ_{int}) on (A)linear and (B) logarithmic scale. The cubic fitting (red dotted lines) is $\xi_n^{fit} = \rho_c g(894\mu_{\text{int}}^3 - 386\mu_{\text{int}}^2 + 89\mu_{\text{int}})$. Corresponding values are given in table C.1.

C.3 Surface friction (μ_{surf}) dependence of 3D-RFT

Similar to μ_{int}, we explore the dependence of 3D-RFT forces on material-body surface friction (μ_{surf}) by conducting plate intrusions at different combinations of (μ_{int}) and (μ_{surf}). To better understand the trends, we consider the ratio of normal and tangential component of $\boldsymbol{\alpha}$ i.e. $|\boldsymbol{\alpha}_t|/|\boldsymbol{\alpha}_n|$. Figure C-3 shows scaled values of $\boldsymbol{\alpha}_n$ scaled by the scaling coefficient ξ_n discussed in the previous section and shown in

figure C-2. The plots conclude the ratio $|\boldsymbol{\alpha}_t|/|\boldsymbol{\alpha}_n|$ largely remains independent of μ_{int} as the graphs remain largely identical for same values of μ_{surf} at different values of μ_{int}. We also conclude that the graphs at low values of μ_{surf} are derivable for higher values of μ_{surf} by cutting off the values from high μ_{surf} at the μ_{surf} at which new graph is required. Eq 5.6 incorporates this concept into the final form of 3D-RFT. The proposed generic 3D-RFT graphs in this study correspond to $\mu_{\text{surf}} = 0.9$.

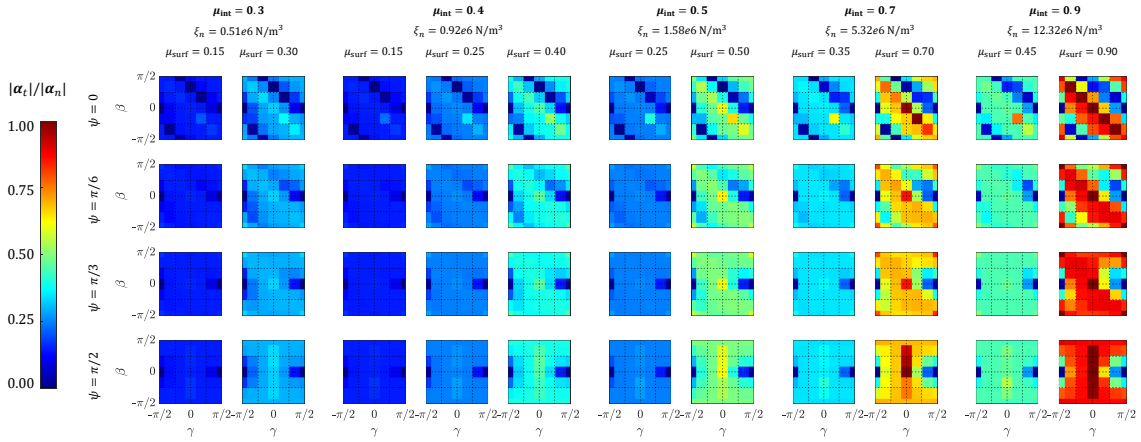

Figure C-3: *Variation of $|\boldsymbol{\alpha}_t|/|\boldsymbol{\alpha}_n|$ with material properties*: Variation of ratio of magnitude of $\boldsymbol{\alpha}$ in tangential and normal directions. The ratio never exceeds the individual μ_{surf} values in each case due to Coulomb friction condition. Corresponding values of μ_{int}, μ_{surf}, and ξ_n are written at the top of each column. The granular material had an effective density of (ρ_c) 3000 kg/m^3 in the cases.

C.4 Proof that Coulomb friction cut-off step does not affects the satisfaction of rotational symmetry by 3D-RFT form

.

To prove that eq 5.5-5.6 also follow IRT, we subtitute the form of $\boldsymbol{\alpha}$ from eq 5.4-5.6 in eq 5.9:
$\boldsymbol{\alpha}(\hat{\boldsymbol{n}}, \hat{\boldsymbol{v}}, \boldsymbol{g}; \rho_c, \mu_{\text{int}}, \mu_{\text{surf}}) = \boldsymbol{\alpha}(\boldsymbol{R}\hat{\boldsymbol{n}}, \boldsymbol{R}\hat{\boldsymbol{v}}, \boldsymbol{R}\boldsymbol{g}; \rho_c, \mu_{\text{int}}, \mu_{\text{surf}})$

where, $\boldsymbol{R}$ is a unit rotation matrix($|\boldsymbol{R}| = 1$, $\boldsymbol{R}\boldsymbol{R}^T = 1$) as follows:

$$\begin{aligned}
&\boldsymbol{\alpha}(\boldsymbol{R}\hat{\boldsymbol{n}}, \boldsymbol{R}\hat{\boldsymbol{v}}, \boldsymbol{R}\boldsymbol{g}; \rho_c, \mu_{\text{int}}, \mu_{\text{surf}}) \\
&= \rho_c g \hat{f}(\mu_{\text{int}}) |\boldsymbol{\alpha}_n^{\text{gen}}(\boldsymbol{R}\hat{\boldsymbol{n}}, \boldsymbol{R}\hat{\boldsymbol{v}}, \boldsymbol{R}\hat{\boldsymbol{g}})| (\hat{\boldsymbol{n}}) \\
&\quad + \rho_c g \hat{f}(\mu_{\text{int}}) \min\left(\frac{\mu_{\text{surf}} |\boldsymbol{\alpha}_n^{\text{gen}}(\boldsymbol{R}\hat{\boldsymbol{n}}, \boldsymbol{R}\hat{\boldsymbol{v}}, \boldsymbol{R}\hat{\boldsymbol{g}})|}{|\boldsymbol{\alpha}_t^{\text{gen}}(\boldsymbol{R}\hat{\boldsymbol{n}}, \boldsymbol{R}\hat{\boldsymbol{v}}, \boldsymbol{R}\hat{\boldsymbol{g}})|}, 1 \right) \boldsymbol{\alpha}_t^{\text{gen}}(\boldsymbol{R}\hat{\boldsymbol{n}}, \boldsymbol{R}\hat{\boldsymbol{v}}, \boldsymbol{R}\hat{\boldsymbol{g}})
\end{aligned}$$

The scalar value of α_r, α_θ, α_z only depend on the '*dot products*' of $\hat{\boldsymbol{n}}$, $\hat{\boldsymbol{v}}$, and $\hat{\boldsymbol{g}}$ which does not changes upon unit rotation of all the vectors by same rotation $\boldsymbol{R}$. Thus, the rotation $\boldsymbol{R}$ only rotates the local cordinate frame $\{\hat{\boldsymbol{r}}, \hat{\boldsymbol{\theta}}, \hat{\boldsymbol{z}}\}$ to $\{\boldsymbol{R}\hat{\boldsymbol{r}}, \boldsymbol{R}\hat{\boldsymbol{\theta}}, \boldsymbol{R}\hat{\boldsymbol{z}}\}$ without changing α_r, α_θ, α_z values. And

$$\begin{aligned}
\boldsymbol{\alpha}_t^{\text{gen}}(\boldsymbol{R}\hat{\boldsymbol{n}}, \boldsymbol{R}\hat{\boldsymbol{v}}, \boldsymbol{R}\hat{\boldsymbol{g}}) &= \boldsymbol{R}\boldsymbol{\alpha}_t^{\text{gen}}(\hat{\boldsymbol{n}}, \hat{\boldsymbol{v}}, \hat{\boldsymbol{g}}), \text{and} \\
\boldsymbol{\alpha}_n^{\text{gen}}(\boldsymbol{R}\hat{\boldsymbol{n}}, \boldsymbol{R}\hat{\boldsymbol{v}}, \boldsymbol{R}\hat{\boldsymbol{g}}) &= \boldsymbol{R}\boldsymbol{\alpha}_n^{\text{gen}}(\hat{\boldsymbol{n}}, \hat{\boldsymbol{v}}, \hat{\boldsymbol{g}})
\end{aligned}$$

Substituting the values,

$$\begin{aligned}
&\boldsymbol{\alpha}(\boldsymbol{R}\hat{\boldsymbol{n}}, \boldsymbol{R}\hat{\boldsymbol{v}}, \boldsymbol{R}\boldsymbol{g}; \rho_c, \mu_{\text{int}}, \mu_{\text{surf}}) \\
&= \rho_c g \hat{f}(\mu_{\text{int}}) |\boldsymbol{R}| |\boldsymbol{\alpha}_n^{\text{gen}}(\hat{\boldsymbol{n}}, \hat{\boldsymbol{v}}, \hat{\boldsymbol{g}})| (\boldsymbol{R}\hat{\boldsymbol{n}}) \\
&\quad + \rho_c g \hat{f}(\mu_{\text{int}}) \min\left(\frac{\mu_{\text{surf}} |\boldsymbol{R}| |\boldsymbol{\alpha}_n^{\text{gen}}(\hat{\boldsymbol{n}}, \hat{\boldsymbol{v}}, \hat{\boldsymbol{g}})|}{|\boldsymbol{R}| |\boldsymbol{\alpha}_t^{\text{gen}}(\hat{\boldsymbol{n}}, \hat{\boldsymbol{v}}, \hat{\boldsymbol{g}})|}, 1 \right) \boldsymbol{R}\boldsymbol{\alpha}_t^{\text{gen}}(\hat{\boldsymbol{n}}, \hat{\boldsymbol{v}}, \hat{\boldsymbol{g}}) \\
&= \boldsymbol{R}\boldsymbol{\alpha}(\hat{\boldsymbol{n}}, \hat{\boldsymbol{v}}, \boldsymbol{g}; \rho_c, \mu_{\text{int}}, \mu_{\text{surf}})
\end{aligned} \tag{C.1}$$

Thus, 3D-RFT form 5.5-5.6 continue to satisfy IRT requirements and thus satisfy all the constraints implied on it from *Global rotational constraint*.

C.5 Verification of leading edge hypothesis in 3D-RFT

We verify the applicability of the 'leading-edge hypothesis' (mentioned in *Premise-2*) during three-dimensional plate motion. To verify the hypothesis, we plot the variations of forces on the front and the back surface–nodes of the plate geometry used for generating the reference 3D-RFT graphs. Figure C-5 shows the variations of force magnitudes on the two surfaces the plates used for modeling intrusions. We plot these results for six plate and velocity configurations. The sides are color-coded in blue and red. In the first two cases, the front-face (in red) acts as the leading edge. In the next two cases, the back-face (in blue) acts as the leading edge. In all such cases, we measure leading edges forces, as non-leading edge forces are negligible in comparison to leading-edge forces. In the last two cases, both the faces experience

Table C.2: DEM material properties

Grain diameter (d)	50/50 split: 3 mm / 3.4 mm
Grain density (ρ_g)	2470 kg/m^3
Packing effciency (ϕ)	~ 0.59
Contact model	Hookean contact model
Elastic modulus, E	7×10^6 N/m^2
Poisson's ratio, ν	0.45
Coefficient of restitution, e	0.88
Grain-grain friction, μ_{g-g}	0.05
Grain-surface friction, μ_{g-s}	0.4
Characteristic velocity	2

equal force magnitudes with (equal tangential forces but equal and opposite normal forces). The last two cases correspond to the slicing motion of the surfaces. We take average force magnitudes for making RFT plots in such cases. We observed similar behavior in other plate and velocity configurations.

C.6 DEM simulations

In this section, we discuss the details of DEM systems used for verifications studies. We use DEM based LIGGGHTS package for modeling grains. We use a 50/50 split of 3.0 mm and 3.4 mm diameter (d) grains in all the DEM simulations. More material properties are given in table C.2. We use a simple shear simulation setup to determine the internal friction of the bulk of the granular volume. The setup consisted of a $100d \times 50d \times 90d$ granular bed in plane-strain condition and was sheared with rigid plates on the top and the bottom as shown in figure C-4. For uniform shearing at constant pressure, a uniformly distributed constant force (F_{top}) was applied on the top plate whose motion was restricted to z-direction. An identical bottom plate was moved in positive x-direction to create the quasi-static simple shear condition.

C.7 Radius of curvature corrections to Bunny drill

As discussed in Premise-6, the RFT form assumes a scale separation by treating granular media as a continua. This assumption limits the performance of 3D-RFT when objects have sharp corners. While characterizing these effects would be a work for the future, we attempt to incorporate these effects at the most basic level in bunny drill simulations. This is important in the Bunny drill case because many features of the bunny shape have competing length scales to grain size in this DEM-based

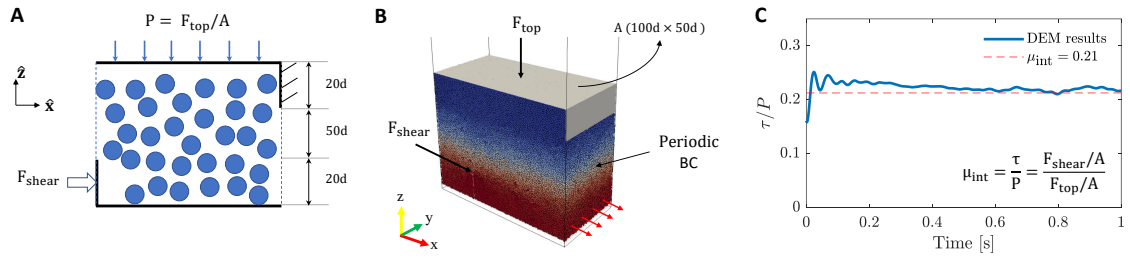

Figure C-4: *Simple shear DEM setup*: (A)2D schematic and (B)3D snapshot of the DEM simulation setup used for finding the internal friction coefficient of DEM particles used for verification studies. (C) Variation of the ratio of shear stess ($\tau = F_{shear}/A$) and pressure ($P = F_{top}/A$) as a function of time from DEM (solid blue line) and fitted estimate (red dotted line). Material properties are provided in table C.2

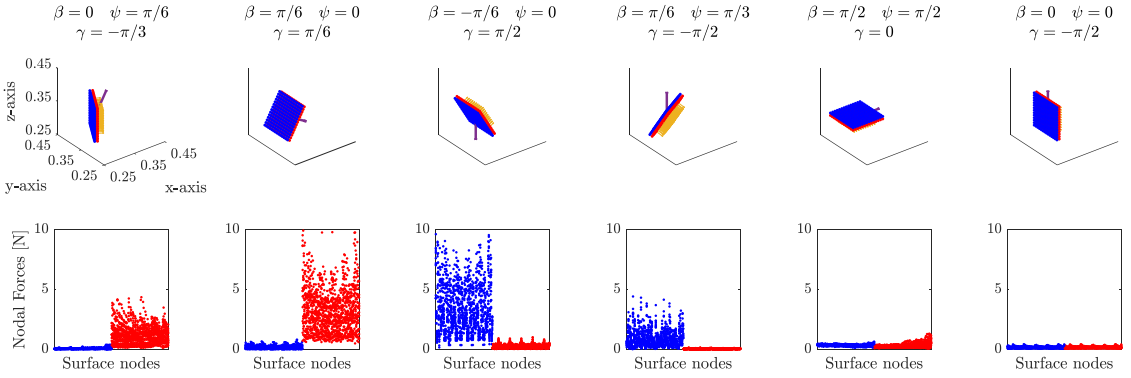

Figure C-5: *Leading edge hypothesis verification:*: Variation of the magnitude of forces on the two sides of thin plates during granular intrusions. The sides are color-coded in blue and red. The yellow arrows show front-face normals, and the violet arrow shows the velocity direction. We plot six combinations of plate configurations and velocity directions. In the first two cases, the front-face (in red) acts as the leading edge. In the next two cases, the back-face (in blue) acts as the leading edge. And in the last two cases, both the faces experience equal force magnitudes with (equal tangential forces but equal and opposite normal forces). The last two cases correspond to the slicing motion of the surfaces. We take average force magnitudes for making RFT plots in such cases.

study. The grain size could not be reduced further in this study due to limitations on computational resources. Thus, we use a simple *Radius of curvature (R_c)* based identification of low-R_c regions of this intruder. We assume that any surface with a

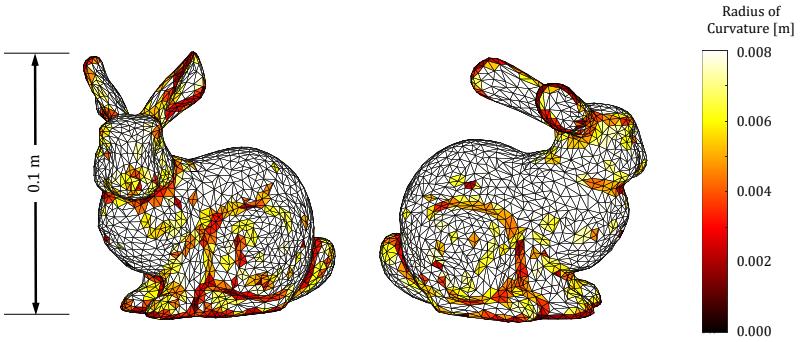

Figure C-6: *Variation of radius of curvature (R_c) on Bunny shape*: The colormap on the right shows the variations. R_c cut-off for active surfaces was set at 0.0048 m.

vertex with a radius of curvature lesser than 2 times the average grain radius will not experience any resistive force from the granular volumes. R_c was calculated using the discrete principle curvature formula from Hao Li's lecture notes [180]. Figure C-6 shows the radius of curvature estimation across the bunny shape used in this study.

Table C.3: f_1, f_2, f_3 3rd degree polynomial definitions

$f_i = \sum_k c_i^k T_k = c_i^1 + c_i^2 x_1 + \ldots\ldots + c_i^{19} x_1 x_3^2 + c_i^{20} x_1 x_2 x_3$ $\left(x_1 = \sin\gamma,\ x_2 = \cos\beta,\ \text{and}\ x_3 = \cos\psi\cos\gamma\sin(\beta) + \sin\gamma\cos\beta\right)$				
k	T_k	c_1^k	c_2^k	c_3^k
1	1	0.00212	−0.06796	−0.02634
2	x_1	−0.02320	−0.10941	−0.03436
3	x_2	−0.20890	0.04725	0.45256
4	x_3	−0.43083	−0.06914	0.00835
5	x_1^2	−0.00259	−0.05835	0.02553
6	x_2^2	0.48872	−0.65880	−1.31290
7	x_3^2	−0.00415	−0.11985	−0.05532
8	$x_1 x_2$	0.07204	−0.25739	0.06790
9	$x_2 x_3$	−0.02750	−0.26834	−0.16404
10	$x_3 x_1$	−0.08772	0.02692	0.02287
11	x_1^3	0.01992	−0.00736	0.02927
12	x_2^3	−0.45961	0.63758	0.95406
13	x_3^3	0.40799	0.08997	−0.00131
14	$x_1 x_2^2$	−0.10107	0.21069	−0.11028
15	$x_2 x_1^2$	−0.06576	0.04748	0.01487
16	$x_2 x_3^2$	0.05664	0.20406	−0.02730
17	$x_3 x_2^2$	−0.09269	0.18519	0.10911
18	$x_3 x_1^2$	0.01892	0.04934	−0.04097
19	$x_1 x_3^2$	0.01033	0.13527	0.07881
20	$x_1 x_2 x_3$	0.15120	−0.33207	−0.27519

Table C.4: f_1, f_2, and f_3 function definitions with 4^{th} degree polynomials

$f_i = \sum_k c_i^k T_k = c_i^1 + c_i^2 x_1 + \ldots\ldots + c_i^{19} x_1 x_3^2 + c_i^{35} x_1 x_2 x_3^2$ $\left(x_1 = \sin\gamma,\ x_2 = \cos\beta, \text{ and } x_3 = \cos\psi\cos\gamma\sin(\beta) + \sin\gamma\cos\beta\right)$				
k	T_k	c_1^k	c_2^k	c_3^k
1	1	0.00412	−0.06300	0.00892
2	x_1	−0.02136	−0.00336	−0.03143
3	x_2	−0.21785	−1.32520	−0.54392
4	x_3	−0.54991	0.00048	0.01939
5	x_1^2	−0.03285	−0.11116	−0.11861
6	x_2^2	0.87718	5.36790	2.03150
7	x_3^2	−0.00286	0.07983	−0.13326
8	$x_1 x_2$	−0.38369	0.08966	0.47638
9	$x_2 x_3$	0.48733	−0.11872	−0.35913
10	$x_3 x_1$	−0.16974	0.09029	0.13672
11	x_1^3	0.01923	−0.10024	0.01495
12	x_2^3	−1.82110	−7.53640	−2.44120
13	x_3^3	0.71170	−0.03393	−0.01711
14	$x_1 x_2^2$	1.03580	−0.48634	−1.14260
15	$x_2 x_1^2$	−0.06899	0.07279	0.20511
16	$x_2 x_3^2$	0.01924	0.15943	0.01142
17	$x_3 x_2^2$	−1.58070	−0.45871	0.52431
18	$x_3 x_1^2$	0.07461	0.10419	−0.03870
19	$x_1 x_3^2$	0.04814	−0.09860	0.10985
20	$x_1 x_2 x_3$	0.05565	−0.21270	−0.06686
21	x_1^4	0.02884	−0.02951	0.11721
22	x_4^4	1.10100	3.35300	0.90658
23	x_3^4	0.03094	−0.45255	0.03809
24	$x_1^3 x_2$	0.24807	0.07722	−0.25744
25	$x_1^3 x_3$	0.05269	−0.07405	−0.26752
26	$x_2^3 x_1$	−0.72304	0.32683	0.67218
27	$x_2^3 x_3$	1.15170	0.39561	−0.31197
28	$x_3^3 x_1$	0.20145	−0.13273	−0.11735
29	$x_3^3 x_2$	−0.09466	0.15479	0.06806
30	$x_1^2 x_2^2$	0.12995	0.08606	−0.12606
31	$x_1^2 x_3^2$	−0.06983	0.19846	0.18106
32	$x_2^2 x_3^2$	0.09628	0.29711	−0.02546
33	$x_1^2 x_2 x_3$	−0.57151	−0.07567	0.54032
34	$x_1 x_2^2 x_3$	−0.24520	−0.05941	−0.06226
35	$x_1 x_2 x_3^3$	0.03159	0.14051	−0.33556

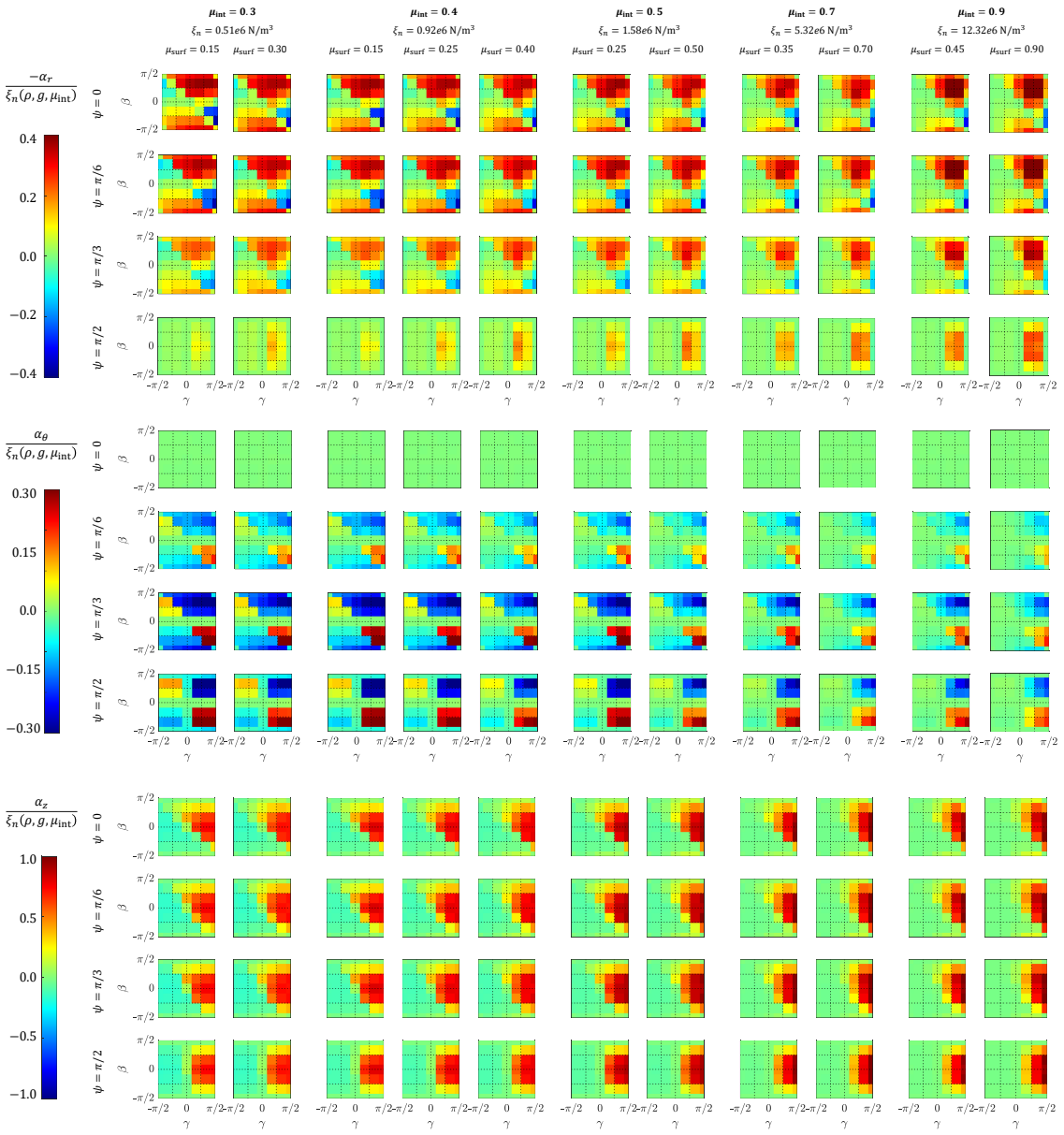

Figure C-7: *3D-RFT Raw data*: Normalized $\alpha_{r,\theta,z}$ value for 3D-RFT reference data used for generation of 3D-RFT form. Corresponding values of μ_{int}, μ_{surf}, and ξ_n are written at the top of each column.

Bibliography

[1] Patrick Richard, Mario Nicodemi, Renaud Delannay, Philippe Ribiere, and Daniel Bideau. Slow relaxation and compaction of granular systems. *Nature materials*, 4(2):121–128, 2005.

[2] Devaraj Van Der Meer. Impact on granular beds. *Annual review of fluid mechanics*, 49:463–484, 2017.

[3] Detlef Lohse, Raymond Bergmann, René Mikkelsen, Christiaan Zeilstra, Devaraj van der Meer, Michel Versluis, Ko van der Weele, Martin van der Hoef, and Hans Kuipers. Impact on soft sand: void collapse and jet formation. *Physical review letters*, 93(19):198003, 2004.

[4] Guidare sulla sabbia. A car moving in desert. .brumbrum.it, September 2020.

[5] Microgen Images/science Photo Library. Golfer in sand trap. https://fineartamerica.com/, November 2019.

[6] Jack Delulio. A bike wheel over sands. unsplash.com.

[7] Bruno Andreotti, Yoël Forterre, and Olivier Pouliquen. *Granular media: between fluid and solid*. Cambridge University Press, 2013.

[8] Dierk Raabe, M Sachtleber, Zisu Zhao, Franz Roters, and Stefan Zaefferer. Micromechanical and macromechanical effects in grain scale polycrystal plasticity experimentation and simulation. *Acta materialia*, 49(17):3433–3441, 2001.

[9] Dilip M Parikh. Handbook of pharmaceutical granulation technology. *Drugs and the pharmaceutical sciences*, 81, 2005.

[10] Gerard R Klinzing and Gregory M Troup. Modeling the air pressure increase within a powder bed during compression—a step toward understanding tablet defects. *Journal of pharmaceutical sciences*, 108(6):1991–2001, 2019.

[11] JC Cunningham, IC Sinka, and A Zavaliangos. Analysis of tablet compaction. i. characterization of mechanical behavior of powder and powder/tooling friction. *Journal of pharmaceutical sciences*, 93(8):2022–2039, 2004.

[12] T Bo Anderson and Roy Jackson. Fluid mechanical description of fluidized beds. equations of motion. *Industrial & Engineering Chemistry Fundamentals*, 6(4):527–539, 1967.

[13] Aaron S Baumgarten and Ken Kamrin. A general fluid–sediment mixture model and constitutive theory validated in many flow regimes. *Journal of Fluid Mechanics*, 861:721–764, 2019.

[14] Antonios Zavaliangos, Jeffrey M Katz, Dominick Daurio, Michael Johnson, Armen Pirjanian, and Fernando Alvarez-Nunez. Prediction of air entrapment in tableting: an approximate solution. *Journal of pharmaceutical sciences*, 106(12):3604–3612, 2017.

[15] Nariman Mahabadi and Jaewon Jang. The impact of fluid flow on force chains in granular media. *Applied Physics Letters*, 110(4):041907, 2017.

[16] Shashank Agarwal, Andras Karsai, Daniel I Goldman, and Ken Kamrin. Surprising simplicity in the modeling of dynamic granular intrusion. *Science Advances*, 7(17):eabe0631, 2021.

[17] Shashank Agarwal, Andras Karsai, Daniel I Goldman, and Ken Kamrin. Efficacy of simple continuum models for diverse granular intrusions. *Soft Matter*, 17(30):7196–7209, 2021.

[18] Christoph Kloss, Christoph Goniva, Alice Hager, Stefan Amberger, and Stefan Pirker. Models, algorithms and validation for opensource dem and cfd–dem. *Progress in Computational Fluid Dynamics, an International Journal*, 12(2-3):140–152, 2012.

[19] Nikolai V Brilliantov, Frank Spahn, Jan-Martin Hertzsch, and Thorsten Pöschel. Model for collisions in granular gases. *Physical review E*, 53(5):5382, 1996.

[20] Leonardo E Silbert, Deniz Ertaş, Gary S Grest, Thomas C Halsey, Dov Levine, and Steven J Plimpton. Granular flow down an inclined plane: Bagnold scaling and rheology. *Physical Review E*, 64(5):051302, 2001.

[21] HP Zhang and HA Makse. Jamming transition in emulsions and granular materials. *Physical Review E*, 72(1):011301, 2005.

[22] Peter A Cundall and Otto DL Strack. A discrete numerical model for granular assemblies. *geotechnique*, 29(1):47–65, 1979.

[23] Contact forces in DEM. Lammmps. Accessed on March 1, 2022.

[24] André Katterfeld and Christopher Wensrich. Understanding granular media: from fundamentals and simulations to industrial application. *Granular Matter*, 19(4):1–4, 2017.

[25] Christoph Goniva, Christoph Kloss, Niels G Deen, Johannes AM Kuipers, and Stefan Pirker. Influence of rolling friction on single spout fluidized bed simulation. *Particuology*, 10(5):582–591, 2012.

[26] Reza M Baram and Pedro G Lind. Deposition of general ellipsoidal particles. *Physical Review E*, 85(4):041301, 2012.

[27] Saviz Mowlavi and Ken Kamrin. Contact model for elastically anisotropic bodies and efficient implementation into the discrete element method. *Granular Matter*, 23(2):1–29, 2021.

[28] Reid Kawamoto, Edward Andò, Gioacchino Viggiani, and José E Andrade. All you need is shape: predicting shear banding in sand with ls-dem. *Journal of the Mechanics and Physics of Solids*, 111:375–392, 2018.

[29] Alireza Khazeni and Zahra Mansourpour. Influence of non-spherical shape approximation on dem simulation accuracy by multi-sphere method. *Powder Technology*, 332:265–278, 2018.

[30] G Lu, JR Third, and CR Müller. Discrete element models for non-spherical particle systems: From theoretical developments to applications. *Chemical Engineering Science*, 127:425–465, 2015.

[31] NH Minh and YP Cheng. A dem investigation of the effect of particle-size distribution on one-dimensional compression. *Géotechnique*, 63(1):44–53, 2013.

[32] Maria Paulick, Martin Morgeneyer, and Arno Kwade. Review on the influence of elastic particle properties on dem simulation results. *Powder Technology*, 283:66–76, 2015.

[33] Dalibor Jajcevic, Eva Siegmann, Charles Radeke, and Johannes G Khinast. Large-scale cfd–dem simulations of fluidized granular systems. *Chemical Engineering Science*, 98:298–310, 2013.

[34] Wenqi Zhong, Aibing Yu, Xuejiao Liu, Zhenbo Tong, and Hao Zhang. Dem/cfd-dem modelling of non-spherical particulate systems: theoretical developments and applications. *Powder Technology*, 302:108–152, 2016.

[35] Y Guo, KD Kafui, C-Y Wu, C Thornton, and JPK Seville. A coupled dem/cfd analysis of the effect of air on powder flow during die filling. *AIChE journal*, 55(1):49–62, 2009.

[36] Yanhui Han and Peter A Cundall. Lbm–dem modeling of fluid–solid interaction in porous media. *International Journal for Numerical and Analytical Methods in Geomechanics*, 37(10):1391–1407, 2013.

[37] Buddhima Indraratna, Nghi Minh Phan, Thanh Trung Nguyen, and Jinsong Huang. Simulating subgrade soil fluidization using lbm-dem coupling. *International Journal of Geomechanics*, 21(5):04021039, 2021.

[38] GC Yang, L Jing, CY Kwok, and YD Sobral. A comprehensive parametric study of lbm-dem for immersed granular flows. *Computers and Geotechnics*, 114:103100, 2019.

[39] BH Xu and AB Yu. Numerical simulation of the gas-solid flow in a fluidized bed by combining discrete particle method with computational fluid dynamics. *Chemical Engineering Science*, 52(16):2785–2809, 1997.

[40] Liqiang Lu. Gpu accelerated mfix-dem simulations of granular and multiphase flows. *Particuology*, 62:14–24, 2022.

[41] AS Soliman, SR Reid, and W Johnson. The effect of spherical projectile speed in ricochet off water and sand. *International Journal of Mechanical Sciences*, 18(6):279–284, 1976.

[42] Mehdi Omidvar, Magued Iskander, and Stephan Bless. Response of granular media to rapid penetration. *International Journal of Impact Engineering*, 66:60–82, 2014.

[43] Daniel Ortiz, Nick Gravish, and Michael T Tolley. Soft robot actuation strategies for locomotion in granular substrates. *IEEE Robotics and Automation Letters*, 4(3):2630–2636, 2019.

[44] NM Vriend, JN McElwaine, B Sovilla, CJ Keylock, M Ash, and PV Brennan. High-resolution radar measurements of snow avalanches. *Geophysical Research Letters*, 40(4):727–731, 2013.

[45] Karen E Daniels and Nicholas W Hayman. Force chains in seismogenic faults visualized with photoelastic granular shear experiments. *Journal of Geophysical Research: Solid Earth*, 113:B11, 2008.

[46] Joe D Goddard. Continuum modeling of granular media. *Applied Mechanics Reviews*, 66(5), 2014.

[47] David L Henann and Ken Kamrin. A predictive, size-dependent continuum model for dense granular flows. *Proceedings of the National Academy of Sciences*, 110(17):6730–6735, 2013.

[48] Ken Kamrin. Non-locality in granular flow: Phenomenology and modeling approaches. *Frontiers in Physics*, 7:116, 2019.

[49] Andrew Schofield and Peter Wroth. *Critical state soil mechanics*. McGraw-hill, 1968.

[50] Duane S Cronin, Khahn Bui, Christian Kaufmann, Grant McIntosh, Todd Berstad, and Duane Cronin. Implementation and validation of the johnson-holmquist ceramic material model in ls-dyna. In *Proc. 4th Eur. LS-DYNA Users Conf*, volume 1, pages 47–60, 2003.

[51] Saba Gharehdash, Lu Ming Shen, Yi Xiang Gan, and EA Flores-Johnson. Numerical investigation on fracturing of rock under blast using coupled finite element method and smoothed particle hydrodynamics. In *Applied Mechanics and Materials*, volume 846, pages 102–107. Trans Tech Publ, 2016.

[52] Jianxiu Wang, Yao Yin, and Chuanwen Luo. Johnson–holmquist-ii (jh-2) constitutive model for rock materials: Parameter determination and application in tunnel smooth blasting. *Applied Sciences*, 8(9):1675, 2018.

[53] Pierre Jop, Yoël Forterre, and Olivier Pouliquen. A constitutive law for dense granular flows. *Nature*, 441(7094):727–730, 2006.

[54] GDR MiDi. On dense granular flows. *The European Physical Journal E*, 14(4):341–365, 2004.

[55] Yonghao Yue, Breannan Smith, Peter Yichen Chen, Maytee Chantharayukhonthorn, Ken Kamrin, and Eitan Grinspun. Hybrid grains: adaptive coupling of discrete and continuum simulations of granular media. *ACM Transactions on Graphics (TOG)*, 37(6):1–19, 2018.

[56] Wei Hu, Milad Rakhsha, Lijing Yang, Ken Kamrin, and Dan Negrut. Modeling granular material dynamics and its two-way coupling with moving solid bodies using a continuum representation and the sph method. *Computer Methods in Applied Mechanics and Engineering*, 385:114022, 2021.

[57] Deborah Sulsky, Zhen Chen, and Howard L Schreyer. A particle method for history-dependent materials. *Computer methods in applied mechanics and engineering*, 118(1-2):179–196, 1994.

[58] Donald A Drew. Mathematical modeling of two-phase flow. *Annual review of fluid mechanics*, 15(1):261–291, 1983.

[59] ZY Zhou, SB Kuang, KW Chu, and AB Yu. Discrete particle simulation of particle–fluid flow: model formulations and their applicability. *Journal of Fluid Mechanics*, 661:482–510, 2010.

[60] Shlomo P Neuman. Theoretical derivation of darcy's law. *Acta mechanica*, 25(3):153–170, 1977.

[61] IC Sinka, JC Cunningham, and A Zavaliangos. The effect of wall friction in the compaction of pharmaceutical tablets with curved faces: a validation study of the drucker–prager cap model. *Powder Technology*, 133(1-3):33–43, 2003.

[62] IC Sinka, JC Cunningham, and A Zavaliangos. Analysis of tablet compaction. ii. finite element analysis of density distributions in convex tablets. *Journal of Pharmaceutical Sciences*, 93(8):2040–2053, 2004.

[63] Aaron S Baumgarten and Ken Kamrin. A general constitutive model for dense, fine-particle suspensions validated in many geometries. *Proceedings of the National Academy of Sciences*, 116(42):20828–20836, 2019.

[64] Marsha J Berger and Joseph Oliger. Adaptive mesh refinement for hyperbolic partial differential equations. *Journal of computational Physics*, 53(3):484–512, 1984.

[65] John E Sadler, F Thomas Johnston, and Mostafa H Mahmoud. Designing silo walls for flow patterns. *Structural Journal*, 92(2):219–228, 1995.

[66] Greg Mehos, Mike Eggleston, Shawn Grenier, Christopher Malanga, Grishma Shrestha, and Tristan Trautman. Designing hoppers, bins, and silos for reliable flow. *The Best of Equipment Series*, page 33, 2018.

[67] Dietmar Schulze. Storage of powders and bulk solids in silos. *Dietmar Schulze. com*, 2006.

[68] Masataku Sutoh, Kenji Nagaoka, Keiji Nagatani, and Kazuya Yoshida. Design of wheels with grousers for planetary rovers traveling over loose soil. *Journal of Terramechanics*, 50(5-6):345–353, 2013.

[69] ANJ Stevenson and IM Hutchings. Development of the dry sand/rubber wheel abrasion test. *Wear*, 195(1-2):232–240, 1996.

[70] Thomas JR Hughes. *The finite element method: linear static and dynamic finite element analysis*. Courier Corporation, 2012.

[71] Wikipedia. Rule of thumb. Accessed on March 1, 2022.

[72] Wikipedia. Rule of thumb. Accessed on March 1, 2022.

[73] RD Wismer and HJ Luth. Off-road traction prediction for wheeled vehicles. *Journal of Terramechanics*, 10(2):49–61, 1973.

[74] Dimensionless_numbers. Dimensionless numbers in fluid mechanics. Accessed on March 1, 2022.

[75] Qiong Zhang, Stephen Townsend, and Ken Kamrin. Expanded scaling relations for locomotion in sloped or cohesive granular beds. *Physical Review Fluids*, 5(11):114301, 2020.

[76] James Slonaker, D Carrington Motley, Qiong Zhang, Stephen Townsend, Carmine Senatore, Karl Iagnemma, and Ken Kamrin. General scaling relations for locomotion in granular media. *Physical Review E*, 95(5):052901, 2017.

[77] Wenting Kang, Yajie Feng, Caishan Liu, and Raphael Blumenfeld. Archimedes' law explains penetration of solids into granular media. *Nature communications*, 9(1):1–9, 2018.

[78] David Syrett. *The Eyes of the Desert Rats: British Long-Range Reconnaissance Operations in the North African Desert 1940-43*. Helion, Limited, 2014.

[79] Mieczyslaw Gregory Bekker. Introduction to terrain-vehicle systems. *University of Michigan Press*, 1969.

[80] J. Y. Wong and A. R. Reece. Prediction of rigid wheel performance based on analysis of soil-wheel stresses, Part I. Performance of driven rigid wheels. *Journal of Terramechanics*, 4(1):81–98, 1967.

[81] J. Y. Wong and A. R. Reece. Prediction of rigid wheel performance based on analysis of soil-wheel stresses, Part II. Performance of towed rigid wheels. *Journal of Terramechanics*, 4(2):7–25, 1967.

[82] Z. Janosi and B. Hanamoto. Analytical determination of drawbar pull as a function of slip for tracked vehicles in deformable soils. In *Proceedings of the 1st International Conference on Terrain-Vehicle Systems*, Turin, Italy, 1961.

[83] J Y Wong, M Garber, and J Preston-Thomas. Theoretical prediction and experimental substantiation of the ground pressure distribution and tractive performance of tracked vehicles. *Proceedings of the Institution of Mechanical Engineers, Part D: Journal of Automobile Engineering*, 198(4):265–285, 1984.

[84] J. Y. Wong. *Terramechanics and Off-Road Vehicle Engineering*. Elsevier, UK, 2nd edition, 2010.

[85] R. G. Pope. The effect of sinkage rate on pressure sinkage relationships and rolling resistance in real and artificial clays. *Journal of Terramechanics*, 6(4):31–38, 1969.

[86] M. G. Bekker. *Introduction to Terrain-Vehicle Systems*. The University of Michigan Press, Ann Arbor, 1969.

[87] J. Y. Wong. *Theory Of Ground Vehicles*. John Wiley & Sons, New York, 3rd edition, 2001.

[88] Shashank Agarwal et al. Development of a reduced-order modeling technique for granular locomotion. Master's thesis, Massachusetts Institute of Technology, 2019.

[89] James Gray and GJ Hancock. The propulsion of sea-urchin spermatozoa. *Journal of Experimental Biology*, 32(4):802–814, 1955.

[90] Charles J Brokaw. Flagellar propulsion. *Journal of Experimental Biology*, 209(6):985–986, 2006.

[91] Ryan D Maladen, Yang Ding, Chen Li, and Daniel I Goldman. Undulatory swimming in sand: subsurface locomotion of the sandfish lizard. *science*, 325(5938):314–318, 2009.

[92] Tingnan Zhang and Daniel I Goldman. The effectiveness of resistive force theory in granular locomotion. *Physics of Fluids*, 26(10):101308, 2014.

[93] Chen Li, Tingnan Zhang, and Daniel I Goldman. A terradynamics of legged locomotion on granular media. *Science*, 339(6126):1408–1412, 2013.

[94] Nick Gravish, Paul B. Umbanhowar, and Daniel I. Goldman. Force and flow at the onset of drag in plowed granular media. *Physical Review E*, 89(4), apr 2014.

[95] Shashank Agarwal, Carmine Senatore, Tingnan Zhang, Mark Kingsbury, Karl Iagnemma, Daniel I Goldman, and Ken Kamrin. Modeling of the interaction of rigid wheels with dry granular media. *Journal of Terramechanics*, 85:1–14, 2019.

[96] Joost H van der Linden, Guillermo A Narsilio, and Antoinette Tordesillas. Machine learning framework for analysis of transport through complex networks in porous, granular media: A focus on permeability. *Physical Review E*, 94(2):022904, 2016.

[97] Connor Schenck, Jonathan Tompson, Sergey Levine, and Dieter Fox. Learning robotic manipulation of granular media. In *Conference on Robot Learning*, pages 239–248. PMLR, 2017.

[98] Mohamed-Rafik Bouguelia, Ramon Gonzalez, Karl Iagnemma, and Stefan Byttner. Unsupervised classification of slip events for planetary exploration rovers. *Journal of Terramechanics*, 73:95–106, 2017.

[99] Ramon Gonzalez, Samuel Chandler, and Dimi Apostolopoulos. Characterization of machine learning algorithms for slippage estimation in planetary exploration rovers. *Journal of Terramechanics*, 82:23–34, 2019.

[100] Nicole Mazouchova, Paul B Umbanhowar, and Daniel I Goldman. Flipper-driven terrestrial locomotion of a sea turtle-inspired robot. *Bioinspiration & Biomimetics*, 8(2):026007, apr 2013.

[101] David Muir Wood. *Soil behaviour and critical state soil mechanics*. Cambridge University Press, 1990.

[102] Richard P Jensen, Peter J Bosscher, Michael E Plesha, and Tuncer B Edil. Dem simulation of granular media—structure interface: effects of surface roughness and particle shape. *International Journal for Numerical and Analytical Methods in Geomechanics*, 23(6):531–547, 1999.

[103] Richard P Jensen, Michael E Plesha, Tuncer B Edil, Peter J Bosscher, and Nabil Ben Kahla. Dem simulation of particle damage in granular media—structure interfaces. *International Journal of Geomechanics*, 1(1):21–39, 2001.

[104] Ken Kamrin and Georg Koval. Nonlocal constitutive relation for steady granular flow. *Physical Review Letters*, 108(17):178301, 2012.

[105] Seongmin Kim and Ken Kamrin. Power-law scaling in granular rheology across flow geometries. *Physical Review Letters*, 125 (8):088002, 2020.

[106] Conlain Kelly, Nicholas Olsen, and Dan Negrut. Billion degree of freedom granular dynamics simulation on commodity hardware via heterogeneous datatype representation. *Multibody Systems Dynamics*, 5:355–379, 2020.

[107] Hai-Sui Yu. Non-coaxial theories of plasticity for granular materials. In *Keynote lecture. Proc. 12th Int. Conf. IACMAG, Goa, India*, volume 1, pages 361–378. Citeseer, 2008.

[108] Sachith Dunatunga and Ken Kamrin. Continuum modelling and simulation of granular flows through their many phases. *Journal of Fluid Mechanics*, 779:483–513, 2015.

[109] Sachith Dunatunga and Ken Kamrin. Continuum modeling of projectile impact and penetration in dry granular media. *Journal of the Mechanics and Physics of Solids*, 100:45–60, 2017.

[110] Donald W Taylor. *Fundamentals of soil mechanics*, volume 66. LWW, 1948.

[111] Gilles Daviet and Florence Bertails-Descoubes. A semi-implicit material point method for the continuum simulation of granular materials. *ACM Transactions on Graphics (TOG)*, 35(4):1–13, 2016.

[112] Gilles Daviet and Florence Bertails-Descoubes. Nonsmooth simulation of dense granular flows with pressure-dependent yield stress. *Journal of Non-Newtonian Fluid Mechanics*, 234:15–35, 2016.

[113] César Dávalos, Juan Cante, JA Hernández, and Javier Oliver. On the numerical modeling of granular material flows via the particle finite element method (pfem). *International Journal of Solids and Structures*, 71:99–125, 2015.

[114] Chong Peng, Xiaogang Guo, Wei Wu, and Yongqi Wang. Unified modelling of granular media with smoothed particle hydrodynamics. *Acta Geotechnica*, 11(6):1231–1247, 2016.

[115] Ahmed Jarray, Hao Shi, Bert J Scheper, Mehdi Habibi, and Stefan Luding. Cohesion-driven mixing and segregation of dry granular media. *Scientific reports*, 9(1):1–12, 2019.

[116] Jeffrey Aguilar, Tingnan Zhang, Feifei Qian, Mark Kingsbury, Benjamin McInroe, Nicole Mazouchova, Chen Li, Ryan Maladen, Chaohui Gong, Matt Travers, et al. A review on locomotion robophysics: the study of movement at the intersection of robotics, soft matter and dynamical systems. *Reports on Progress in Physics*, 79(11):110001, 2016.

[117] Hongwei Li, Yuanming Lai, Lizhong Wang, Xiaosong Yang, Ningshan Jiang, Liang Li, Cheng Wang, and Baocun Yang. Review of the state of the art: interactions between a buried pipeline and frozen soil. *Cold regions science and technology*, 157:171–186, 2019.

[118] Xue Zhang, Daichao Sheng, George P Kouretzis, Kristian Krabbenhoft, and Scott W Sloan. Numerical investigation of the cylinder movement in granular matter. *Physical Review E*, 91(2):022204, 2015.

[119] François Guillard, Yoël Forterre, and Olivier Pouliquen. Lift forces in granular media. *Physics of Fluids*, 26(4):043301, 2014.

[120] Jinbiao Wu, George Kouretzis, Laxmi Suwal, Yousef Ansari, and Scott W Sloan. Shallow and deep failure mechanisms during uplift and lateral dragging of buried pipes in sand. *Canadian Geotechnical Journal*, 57(10):1472–1483, 2020.

[121] Yang Ding, Nick Gravish, and Daniel I Goldman. Drag induced lift in granular media. *Physical review letters*, 106(2):028001, 2011.

[122] Matthias Klinkmüller, Guido Schreurs, Matthias Rosenau, and Helga Kemnitz. Properties of granular analogue model materials: A community wide survey. *Tectonophysics*, 684:23–38, 2016.

[123] RA López De La Cruz and GA Caballero-Robledo. Lift on side-by-side intruders within a granular flow. *Journal of Fluid Mechanics*, 800:248–263, 2016.

[124] Aymeric Merceron, Alban Sauret, and Pierre Jop. Cooperative effects induced by intruders evolving through a granular medium. *EPL (Europhysics Letters)*, 121(3):34005, 2018.

[125] Swapnil Pravin, Brian Chang, Endao Han, Lionel London, Daniel I Goldman, Heinrich M Jaeger, and S Tonia Hsieh. Effect of two parallel intruders on total work during granular penetrations. *Physical Review E*, 104(2):024902, 2021.

[126] Abram H Clark and Robert P Behringer. Granular impact model as an energy-depth relation. *EPL (Europhysics Letters)*, 101(6):64001, 2013.

[127] Leah K. Roth, Endao Han, and Heinrich M. Jaeger. Intrusion into granular media beyond the quasistatic regime. *Phys. Rev. Lett.*, 126:218001, May 2021.

[128] Hiroaki Katsuragi and Douglas J Durian. Unified force law for granular impact cratering. *Nature physics*, 3(6):420–423, 2007.

[129] Theodore A Brzinski III, Patrick Mayor, and Douglas J Durian. Depth-dependent resistance of granular media to vertical penetration. *Physical review letters*, 111(16):168002, 2013.

[130] Cacey Stevens Bester and Robert P Behringer. Collisional model of energy dissipation in three-dimensional granular impact. *Physical Review E*, 95(3):032906, 2017.

[131] Vadim Vasilevich Sokolovskiĭ. *Statics of soil media*. Butterworths Scientific Publications, 1960.

[132] Allan F Bower. *Chapter 6, Applied mechanics of Solids*. CRC press, 2009.

[133] Jeffrey Aguilar and Daniel I Goldman. Robophysical study of jumping dynamics on granular media. *Nature Physics*, 12(3):278–283, 2016.

[134] L Prandtl. Concerning the hardness of plastic bodies. *Nachr. Ges. Wiss. Gottingen*, pages 74–85, 1920.

[135] R Hill. The plastic yielding of notched bars under tension. *The Quarterly Journal of Mechanics and Applied Mathematics*, 2(1):40–52, 1949.

[136] Nick Gravish, Paul B Umbanhowar, and Daniel I Goldman. Force and flow transition in plowed granular media. *Physical review letters*, 105(12):128301, 2010.

[137] Murino Kobayakawa, Shinichiro Miyai, Takuya Tsuji, and Toshitsugu Tanaka. Interaction between dry granular materials and an inclined plate (comparison between large-scale dem simulation and three-dimensional wedge model). *Journal of Terramechanics*, 90:3–10, 2020.

[138] E Kashizadeh, JP Hambleton, and SA Stanier. A numerical approach for modelling the ploughing process in sands. In *Proc. 14th Int. Conf. IACMAG, Kyoto, Japan*, pages 159–164. Taylor & Francis Books Ltd, 2015.

[139] Zhefei Jin, Zhenhao Shi, and James Hambleton. Small-scale geotechnical testing using a six-axis robot. *Spree Internal Report*, pages 20–7/495S, 2020.

[140] Yajie Feng, Raphael Blumenfeld, and Caishan Liu. Support of modified archimedes' law theory in granular media. *Soft matter*, 15(14):3008–3017, 2019.

[141] Peter Yichen Chen, Maytee Chantharayukhonthorn, Yonghao Yue, Eitan Grinspun, and Ken Kamrin. Hybrid discrete-continuum modeling of shear localization in granular media. *Journal of the Mechanics and Physics of Solids*, page 104404, 2021.

[142] Fei Zhu, Jing Zhao, Sheng Li, Yong Tang, and Guoping Wang. Dynamically enriched mpm for invertible elasticity. In *Computer Graphics Forum*, volume 36, pages 381–392. Wiley Online Library, 2017.

[143] Michael Steffen, Robert M Kirby, and Martin Berzins. Analysis and reduction of quadrature errors in the material point method (mpm). *International journal for numerical methods in engineering*, 76(6):922–948, 2008.

[144] Alberto E Minetti, Georgios Machtsiras, and Jonathan C Masters. The optimum finger spacing in human swimming. *Journal of biomechanics*, 42(13):2188–2190, 2009.

[145] NO Sidelnik and BW Young. Optimising the freestyle swimming stroke: the effect of finger spread. *Sports Engineering*, 9(3):129–135, 2006.

[146] Hesam Askari and Ken Kamrin. Intrusion rheology in grains and other flowable materials. *Nature materials*, 15(12):1274–1279, 2016.

[147] JS Uehara, MA Ambroso, RP Ojha, and Douglas J Durian. Low-speed impact craters in loose granular media. *Physical review letters*, 90(19):194301, 2003.

[148] H Jay Melosh. Impact cratering: A geologic process. *Research supported by NASA. New York, Oxford University Press (Oxford Monographs on Geology and Geophysics, No. 11), 1989, 253 p.*, 11, 1989.

[149] Runchen Zhao, Qianyun Zhang, Hendro Tjugito, and Xiang Cheng. Granular impact cratering by liquid drops: Understanding raindrop imprints through an analogy to asteroid strikes. *Proceedings of the National Academy of Sciences*, 112(2):342–347, 2015.

[150] Sylvain Joubaud, Tess Homan, Y Gasteuil, Detlef Lohse, and Devaraj van der Meer. Forces encountered by a sphere during impact into sand. *Physical Review E*, 90(6):060201, 2014.

[151] RE Arvidson, P DeGrosse Jr, JP Grotzinger, MC Heverly, J Shechet, SJ Moreland, MA Newby, N Stein, AC Steffy, F Zhou, et al. Relating geologic units and mobility system kinematics contributing to curiosity wheel damage at gale crater, mars. *Journal of Terramechanics*, 73:73–93, 2017.

[152] Antas Singh. Man running on sand. Pexels.com, September 2018.

[153] Aaron M Johnson, Matthew T Hale, Galen C Haynes, and Daniel E Koditschek. Autonomous legged hill and stairwell ascent. In *2011 IEEE International Symposium on Safety, Security, and Rescue Robotics*, pages 134–142. IEEE, 2011.

[154] Daniel. Rider riding green motocross dirt bike. Pexels.com, February 2011.

[155] Liang Ding, Haibo Gao, Zongquan Deng, Keiji Nagatani, and Kazuya Yoshida. Experimental study and analysis on driving wheels' performance for planetary exploration rovers moving in deformable soil. *Journal of Terramechanics*, 48(1):27–45, 2011.

[156] Hirotaka Suzuki, Kota Katsushima, and Shingo Ozaki. Study on applicability of rft to traveling analysis of wheel with grousers: Comparison with dem analysis as a virtual test. *Journal of Terramechanics*, 83:15–24, 2019.

[157] Siddharth Shrivastava, Andras Karsai, Yasemin Ozkan Aydin, Ross Pettinger, William Bluethmann, Robert O. Ambrose, and Daniel I. Goldman. Material remodeling and unconventional gaits facilitate locomotion of a robophysical rover over granular terrain. *Science Robotics*, 5(42), 2020.

[158] C. Li, P. B. Umbanhowar, H. Komsuoglu, D. E. Koditschek, and D. I. Goldman. Sensitive dependence of the motion of a legged robot on granular media. *Proceedings of the National Academy of Sciences*, 106(9):3029–3034, feb 2009.

[159] Douglas Rubin, Naomi Goldenson, and Greg A Voth. Failure and strengthening of granular slopes under horizontal vibration. *Physical Review E*, 74(5):051307, 2006.

[160] Abram H Clark, Alec J Petersen, and Robert P Behringer. Collisional model for granular impact dynamics. *Physical Review E*, 89(1):012201, 2014.

[161] Paul Umbanhowar and Daniel I Goldman. Granular impact and the critical packing state. *Physical Review E*, 82(1):010301, 2010.

[162] Abram H Clark, Lou Kondic, and Robert P Behringer. Steady flow dynamics during granular impact. *Physical Review E*, 93(5):050901, 2016.

[163] Abram H Clark, Lou Kondic, and Robert P Behringer. Particle scale dynamics in granular impact. *Physical review letters*, 109(23):238302, 2012.

[164] Perrin E Schiebel, Henry C Astley, Jennifer M Rieser, Shashank Agarwal, Christian Hubicki, Alex M Hubbard, Kelimar Diaz, Joseph R Mendelson III, Ken Kamrin, and Daniel I Goldman. Mitigating memory effects during undulatory locomotion on hysteretic materials. *Elife*, 9:e51412, 2020.

[165] Perrin E Schiebel, Henry C Astley, Jennifer M Rieser, Shashank Agarwal, Christian Hubicki, Alex M Hubbard, Kelimar Cruz, Joseph Mendelson, Ken Kamrin, and Daniel I Goldman. Mitigating memory effects during undulatory locomotion on hysteretic materials. *bioRxiv*, page 748186, 2019.

[166] J.P. Hambleton and A. Drescher. On modeling a rolling wheel in the presence of plastic deformation as a three- or two-dimensional process. *International Journal of Mechanical Sciences*, 51(11-12):846–855, nov 2009.

[167] Tingnan Zhang, Feifei Qian, Chen Li, Pierangelo Masarati, Aaron M Hoover, Paul Birkmeyer, Andrew Pullin, Ronald S Fearing, and Daniel I Goldman. Ground fluidization promotes rapid running of a lightweight robot. *The International Journal of Robotics Research*, 32(7):859–869, 2013.

[168] Laura K Treers, Cyndia Cao, and Hannah S Stuart. Granular resistive force theory implementation for three-dimensional trajectories. *IEEE Robotics and Automation Letters*, 6(2):1887–1894, 2021.

[169] Auke J Ijspeert. Biorobotics: Using robots to emulate and investigate agile locomotion. *science*, 346(6206):196–203, 2014.

[170] Ryan D Maladen, Yang Ding, Paul B Umbanhowar, Adam Kamor, and Daniel I Goldman. Mechanical models of sandfish locomotion reveal principles of high performance subsurface sand-swimming. *Journal of The Royal Society Interface*, 8(62):1332–1345, 2011.

[171] GF Smith. On isotropic functions of symmetric tensors, skew-symmetric tensors and vectors. *International journal of engineering science*, 9(10):899–916, 1971.

[172] Greg Turk and Marc Levoy. Zippered polygon meshes from range images. In *Proceedings of the 21st annual conference on Computer graphics and interactive techniques*, pages 311–318, 1994.

[173] Alex A Francoeur and Kelly M Dorgan. Burrowing behavior in mud and sand of morphologically divergent polychaete species (annelida: Orbiniidae). *The Biological Bulletin*, 226(2):131–145, 2014.

[174] Antoine Humeau, Miguel Piñeirua, Jérôme Crassous, and Jérôme Casas. Locomotion of ants walking up slippery slopes of granular materials. *Integrative Organismal Biology*, 1(1):obz020, 2019.

[175] Rui He, Corina Sandu, Aamir K Khan, A Glenn Guthrie, P Schalk Els, and Herman A Hamersma. Review of terramechanics models and their applicability to real-time applications. *Journal of Terramechanics*, 81:3–22, 2019.

[176] Esteban Wright, Alice C Quillen, Juliana South, Randal C Nelson, Paul Sánchez, John Siu, Hesam Askari, Miki Nakajima, and Stephen R Schwartz. Ricochets on asteroids: Experimental study of low velocity grazing impacts into granular media. *Icarus*, 351:113963, 2020.

[177] Henry C Astley, Joseph R Mendelson III, Jin Dai, Chaohui Gong, Baxi Chong, Jennifer M Rieser, Perrin E Schiebel, Sarah S Sharpe, Ross L Hatton, Howie Choset, et al. Surprising simplicities and syntheses in limbless self-propulsion in sand. *Journal of Experimental Biology*, 223(5):jeb103564, 2020.

[178] GDR MiDi gdrmidi@ polytech. univ-mrs. fr http://www. lmgc. univ-montp2. fr/MIDI/. On dense granular flows. *The European Physical Journal E*, 14:341–365, 2004.

[179] Cecily Sunday, Naomi Murdoch, Arnaud Wilhelm, Melanie Drilleau, Yun Zhang, Simon Tardivel, and Patrick Michel. The influence of gravity on granular impacts-ii. a gravity-scaled collision model for slow interactions. *Astronomy & Astrophysics*, 658:A118, 2022.

[180] Hao Li , CSCI 599: Digital Geometry Processing. Differential operators on polygons. http://cs599.hao-li.com/.